

---

# Picometer scale imaging of the valence electron potential of solids

Harshit Lakhota

---



München 2019



---

# Picometer scale imaging of the valence electron potential of solids

Harshit Lakhota

---

Dissertation  
an der Fakultät für Physik  
der Ludwig-Maximilians-Universität  
München

vorgelegt von  
Harshit Lakhota  
aus Bhadreswar, India

München, den 13.02.2019

Erstgutachter: Priv.-Doz. Dr. Martin Schultze

Zweitgutachter: Prof. Dr. Eleftherios Goulielmakis

Tag der mündlichen Prüfung: 04.04.2019

# Zusammenfassung

Die Verteilung der Dichte der Valenzelektronen in Materialien definiert deren chemische, optische und biologische Eigenschaften. Daher ist die direkte Darstellung von Valenzelektronen in Festkörpern von höchster Wichtigkeit. Röntgenelektronen- und Neutronenbeugung liefern essentielle Informationen über die atomaren Positionen in Materialien, aber versagen bei der Messung der Dichte der Valenzelektronen. Diese Arbeit konzentriert ihre Bestrebungen auf dieses essentielle Problem.

Durch die Erzeugung Hoher-Harmonischer in Gasen konnten bereits erfolgreich die Bewegungen von Molekülorbitalen dargestellt und Valenzelektronenbewegungen gemessen werden. Die kürzliche Entdeckung Hoher-Harmonischer in kondensierter Materie stellt daher ein vielversprechend Mittel dar, um dieses Potential auch auf Festkörper auszuweiten. Durch die Verwendung starker Laserfelder, die Elektronen in Festkörpern auslenken, und durch die Messung ihrer hohen-harmonischen Emissionsspektren, welche aus der Streuung der Elektronen mit dem periodischen Potential resultieren, versuchen wir das periodische Valenzpotential von Festkörpern zu entschlüsseln.

Es wird diskutiert, dass unter dem Einfluss starker Felder und der hoch-frequenten Anregung von Festkörpern sich Valenzelektronen im Laserfeld wie nahezu freie Teilchen verhalten und dass das periodische Potential lediglich eine schwache Störung ihrer Bewegung darstellt. Dies erlaubt es, bereits entwickelte kinematische Modelle auszuweiten, um die Erzeugung Hoher-Harmonischer zu beschreiben und ihre Charakteristiken wie die Cutoff- Energie und Intensität mit dem periodischen Potential und der Elektronendichte des Festkörpers zu verknüpfen.

Diese Arbeit zeigt theoretisch und beweist experimentell, dass die Cutoff-Energie der hoch-harmonischen Emission es nun erstmalig erlaubt, den ionischen und den kovalenten Radius von Atomen in einem Kristall direkt zu bestimmen. Des Weiteren zeigt sie, dass die Messung der Intensitätsausbeute der Hohen-Harmonischen in Abhängigkeit der Anregungsstärke und für verschiedene Kristallwinkel die gesamte Rekonstruktion des periodischen Potentials und der Elektronendichte im Festkörper erlaubt. Diese Technik erlaubt es somit zum ersten Mal, das "Phasenproblem" zu adressieren. Hohe-Harmonische, die vom Festkörper ausgehen, verkörpern Informationen über die Amplitude und die Phase der Fourier-Komponenten des periodischen Potentials. Das Potential zweier kristalliner Materialien, MgF<sub>2</sub> und CaF<sub>2</sub>, konnte so mit einer Auflösung besser als 50 pm rekonstruiert werden. Studien mehrerer Materialien wie SiO<sub>2</sub>, Diamant, MgO, SiC, und ZnO erlauben es, die Maßstäbe der neuen Mikroskopietechnik zu setzen.



# Abstract

The valence electron density distribution of materials determine their chemical, optical, electronic and biological properties. Hence the direct imaging of valence electrons in solids is of paramount importance. X-ray, electron and neutron diffraction provide essential information about the position of atoms in materials but fail to probe the valence electron density. This thesis attempts to solve this essential problem.

The technique of high harmonic generation in gases have successfully imaged molecular orbital and has allowed observation of valence electron motion. The recent discovery of high harmonic generation (HHG) in condensed matter systems holds promise for extending this capability in solids. Using strong laser fields to drive electrons in the bulk of a material and by recording high harmonics emitted as a result of the scattering of electrons by the periodic potential we attempt to decipher the valence electron potential of solids.

It is argued that under the strong field and high-frequency driving of solids, valence electrons can be treated as nearly free particles in the laser field and that the periodic potential contributes only a weak perturbation in their motion. That allows extending the earlier developed kinematic models to describe the high harmonic generation and to link, their characteristics, such as cutoff energy and intensity with the periodic potential and the electron density of the solid.

The thesis shows theoretically and proves experimentally that the cutoff energy of the high harmonic emission allows for the first time the direct probe of the ionic and covalent radius of atoms inside the crystal. Moreover, it shows that by recording the intensity yield of high harmonics versus the driving strength for various angles of the crystal permits the complete reconstruction of the periodic potential and electron density inside the solid. The technique allows addressing for the first time the “phase problem”. High harmonics emanating from the crystal embody information about the amplitude and the phase of the Fourier components of the periodic potential. For two crystalline materials  $\text{MgF}_2$ , and  $\text{CaF}_2$  the potential is reconstructed with a resolution better than 50 pm. The study of more materials such as  $\text{SiO}_2$ , Diamond,  $\text{MgO}$ ,  $\text{SiC}$ , and  $\text{ZnO}$  allows benchmarking the new microscopy technique.



# Contents

<b>Zusammenfassung</b>	<b>v</b>
<b>Abstract</b>	<b>vi</b>
<b>Introduction</b>	<b>viii</b>
<b>1 Visualizing the microcosm</b>	<b>9</b>
1.1 Ways to determine the crystal structure of matter . . . . .	9
1.2 Microscopy . . . . .	10
1.2.1 Optical microscope . . . . .	10
1.2.2 X-ray microscope . . . . .	12
1.2.3 Electron microscope . . . . .	12
1.2.4 Scanning probe microscope (SPM) . . . . .	12
1.3 Crystallography . . . . .	13
1.3.1 X-ray crystallography and its principles . . . . .	13
1.4 Towards picoscopy of valence electrons . . . . .	18
<b>2 Strong field physics</b>	<b>21</b>
2.1 High harmonic generation (HHG) in gases . . . . .	21
2.2 High harmonic generation in solids . . . . .	22
2.3 Major models of HHG in solids . . . . .	22
2.3.1 Bloch oscillations . . . . .	23
2.3.2 Semiconductor Bloch equations . . . . .	24
2.3.3 Features of HHG in solids . . . . .	25
2.4 Summary . . . . .	27
<b>3 Foundations of optical picoscopy</b>	<b>29</b>
3.1 Introduction to high frequency approximation . . . . .	29
3.2 Understanding valence potential . . . . .	29
3.3 High frequency approximation . . . . .	31
3.3.1 Classical perspective . . . . .	31
3.3.2 Quantum mechanical perspective . . . . .	32
3.3.3 Time dependent density functional theory . . . . .	32

3.4	Semiclassical scattering of high harmonic generation in solids . . . . .	35
3.5	Cutoff law . . . . .	39
3.6	Tool box for picoscopy . . . . .	40
3.6.1	Starting point is symmetry point . . . . .	40
3.6.2	Dipole related to solid structure . . . . .	40
3.6.3	Intensity related to structure factors . . . . .	40
3.6.4	Cutoff links to the smallest specimen in the valence potential . . . . .	41
<b>4</b>	<b>Analogies and differences with crystallography</b>	<b>43</b>
4.1	Amplitude of Fourier coefficients . . . . .	44
4.2	Phase of Fourier coefficients . . . . .	46
<b>5</b>	<b>Methods</b>	<b>49</b>
5.1	Data analysis methods . . . . .	49
5.1.1	Analytical method . . . . .	49
5.1.2	Numerical method . . . . .	50
5.2	2D reconstruction from few projections . . . . .	52
5.2.1	Principles of the 2D reconstruction method . . . . .	54
<b>6</b>	<b>Experimental setup</b>	<b>57</b>
6.1	Elements needed for the picoscope . . . . .	57
6.2	Picoscope apparatus . . . . .	58
6.3	Details of the developed picoscope . . . . .	58
6.3.1	Light Source . . . . .	58
6.3.2	Crystalline sample . . . . .	66
6.3.3	Rotation stage and sample holder . . . . .	66
6.3.4	EUV spectromter . . . . .	66
6.4	Picoscope . . . . .	68
<b>7</b>	<b>Probing the radius of the smallest valence specimen in a crystal</b>	<b>71</b>
7.1	Introduction . . . . .	71
7.2	Shannon radius . . . . .	71
7.3	Measuring the radius of the smallest specimen (Mg) in $\text{MgF}_2$ . . . . .	72
7.4	Radius of smallest valence specimen in various crystals . . . . .	74
7.5	Picometer scale resolution . . . . .	74
<b>8</b>	<b>Picometer scale reconstruction of the valence potential of <math>\text{MgF}_2</math></b>	<b>77</b>
8.1	Crystal structure of $\text{MgF}_2$ . . . . .	77
8.2	The $\text{MgF}_2$ potential calculated using DFT . . . . .	77
8.3	Experiments . . . . .	79
8.4	Retrieving the Fourier coefficients of $\text{MgF}_2$ potential . . . . .	80
8.5	Potential along [100] and [110] crystal direction of $\text{MgF}_2$ . . . . .	80
8.6	Reconstructing the potential of $\text{MgF}_2$ on planes (001) and (002) . . . . .	83

---

8.7	Fitting fidelity analysis . . . . .	85
<b>9</b>	<b>Reconstructing the valence potential of CaF<sub>2</sub></b>	<b>89</b>
9.1	Structure of CaF <sub>2</sub> . . . . .	89
9.2	The CaF <sub>2</sub> potential (DFT) . . . . .	89
9.3	Experiment and Analysis . . . . .	90
9.4	Potential along [100] and [110] direction of CaF <sub>2</sub> crystal . . . . .	91
9.5	Reconstruction of the potential of CaF <sub>2</sub> on (001) plane . . . . .	93
<b>10</b>	<b>Conclusion and Outlook</b>	<b>99</b>
10.1	Conclusion . . . . .	99
10.2	Outlook: Picoscopy . . . . .	100
<b>A</b>	<b>Semiconductor Bloch equations with coulombic interaction</b>	<b>101</b>
<b>B</b>	<b>Coherent sum of equivalent planes</b>	<b>105</b>
<b>C</b>	<b>Calculating harmonic current from time dependent density functional theory</b>	<b>109</b>
<b>D</b>	<b>Projection-slice theorem</b>	<b>111</b>
	<b>Acknowledgments</b>	<b>122</b>



# Introduction

The knowledge of the distribution of electric charges in a material is of great importance in physics, chemistry, material science and biology. This is because the arrangements of atoms inside the crystal and the electron distribution around the atoms describe the mechanical, the chemical, the electronic and the optical properties of the material. This thesis presents a method to image the valence electron distribution of bulk solids. In the following introduction, I provide a brief outline of three major fields of physics: solid state physics, crystallography and ultrafast nonlinear optics, which forms the backbone of the research work presented in this thesis.

A key method for scientific progress is to break a complex problem into small pieces and analyze them individually. In order to understand the properties of matter, several methods have been proposed throughout history. The ancient philosophies attempted to divide matter into elements. Indian philosophers from Vedic times classified material into the earth (Prithvi), fire (Agni), air (Maya) and water (Apa). Greeks introduced the concept of matter being made of invisible and indivisible units. The scientific revolution, beginning in the 17th century, saw the question of “what matter is” as a central theme. At the start of the revolution, Isaac Newton believed that matter consisted of solid, hard, impenetrable, massive and movable particles. The atomic theory, as we know it today, came into existence in its primitive form only in the beginning of the 20th century with the discovery of electrons by J.J. Thompson [1]. Rutherford later provided a model for how electrons are arranged in an atom [2]. Things seemed to fall into place when Drude proposed his theory of electrical and thermal conduction in the 1900s [3]. Although we understood the basic constituents of matter, a complete theory which could describe the underlying physical laws and chemical properties of material was missing.

During the beginning of 20<sup>th</sup> century, with the basic building blocks of matter already understood, the drive was towards understanding the thermal properties of various objects. The black body, an idealized model, was used to understand radiative properties of matter. The classical physics describes the intensity of blackbody radiation to be proportional to frequency for a fixed temperature. This is known as Rayleigh-Jeans law. It works for the low frequencies but diverges quadratically for high-frequencies. This presented a paradoxical problem that the energy of high-frequency light should be higher, thereby diverging and leading to the infinite energy of the system. This paradox came to be

known as the Ultraviolet Catastrophe. In 1900, Max Planck postulated the concept of “quanta” to assert that energy of modes can only be in discrete packets. Using statistical mechanics and the concept of quanta he was able to resolve the ultraviolet paradox by explaining why high-frequency packets are less likely to be excited and thus have lower magnitude, matching the experimental results. This revolutionary idea of quanta was later used by Einstein to explain the photoelectric effect in his seminal papers of 1905. Arthur Compton, C.V. Raman and Pieter Zeeman were among the first to study the quantum aspect of nature, each having a quantum-effect named after them. This ushered in a new era of science and led to the development of quantum physics. Modern quantum mechanics, however, started in the second quarter of the twentieth century with the works of Bohr, Dirac, Heisenberg and Schrödinger, and was further unified and formalized by Hilbert, and John von Neumann.

The missing theory which could explain the fundamental physics at the smallest scales was now found. The foundations of quantum mechanics revolutionized our understanding of the matter. Quantum theory can describe the physical laws of the system if we can mathematically describe all the parameters involved in it. Even if we are able to fully describe the system, a complete analytical solution of the equations is often impossible. “The general theory of quantum mechanics is now almost complete. The underlying physical laws necessary for the mathematical theory of a large part of physics and the whole of chemistry are thus completely known, and the difficulty is only that exact application of these laws leads to equations much too complicated to be soluble” remarked P.A.M. Dirac in 1929, which still holds true today. A mere accurate description of the system does not guarantee a closed-form solution of the Schrödinger equation.

In order to describe a many-body quantum system, the wave-function is written in terms of the position of all  $N$  electron and all  $I$  nuclei present in the system. In the Born-Oppenheimer approximation, the motion of atomic nuclei and electrons can be separated and for many scenarios, the nuclear motion is neglected. Hence for  $N$  electrons present, the system may have  $3N$  degrees of freedom. One may comprehend the insurmountable challenge posed by many electrons from the fact that even obtaining energy eigenfunctions for a helium atom (2 electrons) is analytically impossible. Hence solid systems require another approach to solve this problem. Here we turn to a well-established approach to solve this problem, density functional theory (DFT).

In 1895 the discovery of X-rays by Wilhelm Röntgen led to the birth of crystallography. The advent of crystallography also initiated the quest for understanding the microscopic structure of materials and the arrangement of atoms and electrons inside. The field of X-ray diffraction started in the heart of Munich - Englischer Garten - where conversations between Paul Peter Ewald and Max von Laue sparked the idea that crystals may be used as diffraction gratings. Von Laue worked with Walter Freidrich and Paul Knipping to observe for the first time in 1912 the diffraction of light by copper sulfate crystals. The diffraction showed well-defined spots in a geometric pattern, Laue later developed laws to explain the scattering and was awarded the Nobel prize in Physics (1914) for it. This would be one of the most important discoveries of the century. The discovery provided a non-destructive technique to obtain information about a crystals structure. William Bragg and Lawrence

Bragg developed the law which connects the observed diffraction pattern to the reflection of X-rays from parallel, evenly spaced planes of the crystal. They shared the Nobel prize for it in 1915. The first structures of NaCl, KCl, KBr and KI were published in 1913. The effect of temperature on the crystal structure was studied by Debye in 1913-1914, where he defined a B-factor to incorporate the effects thermal motion, subsequently, this factor was corrected by Waller (1923). The importance of group symmetry to describe crystal structure was realized and in 1919 Niggli published 230 space groups which are still used today. Wyckoff (1922) and Astbury(1924) later published other space-group tables. By 1920 all the basic knowledge and theory of crystallography used today was already developed. However, the necessary instruments to make sense of the complex diffraction patterns were yet to be developed.

William Coolidge constructed completely enclosed X-ray tubes by making ductile tungsten. Coolidge tubes provided an X-ray source of extraordinary brilliance, whose intensity could be controlled. This tube was the workhorse for crystallographers for several decades and was improved upon until the invention of microfocus tubes. Many improvements were made in building high brilliance diffractometers. The next major advance in X-ray science came with the development of synchrotron sources for X-rays, where a magnetic field bends accelerating electrons to generate very bright, intense, coherent, monochromatic but tunable X-ray radiation. Now many countries have also invested in tabletop free electron sources which also provide bright X-rays. These two technologies have revolutionized experimental capabilities. Henceforth, structures of macromolecules such as proteins are obtained on a regular basis. However, the structure determination of large non-symmetric structures brings two major problems to the table: One is the so-called phase problem and the other is the computational challenge.

Periodic potentials of crystalline materials can be decomposed into Fourier components. If the material does not possess an inversion symmetry, Fourier components will also have an imaginary part, in addition to an amplitude. Alas, X-ray diffraction patterns only provide information about the amplitude of Fourier coefficients of the material! The Phase information, necessary for retrieval of electron density of the crystal, is lost in such experiments. In the early years of crystallography, the method of “guess and check” was used. The extensive knowledge of diffraction patterns, symmetry, and geometry of the crystal was used to guess the crystal structure. By 1930 crystalline structures of many inorganic materials and alloys were discovered. Patterson described a method to obtain the crystal structure only with amplitude information, but this method was only applicable to systems with a small number of atoms. Later on, mathematical methods were developed to determine the phases of the Fourier coefficients. These methods seldom require large computing capacities. Before the 1960s the determination of crystal structure was a tedious task but the advancement of computing capabilities also led to the refinement of crystallography. Though mathematical methods are available, direct experimental observation of phases is not yet possible.

The beginning of nonlinear light-matter interaction and the resulting observed phenomena (such as HHG) can be attributed to the invention of the laser in 1960 by Maiman. The theory behind lasers was proposed in 1958 by Townes and brought into existence

two years later. The invention of the laser revolutionized numerous fields namely, laser physics, atomic physics, plasma physics, solid state physics, astrophysics, elementary particle physics etc. Before the invention of lasers, the basic concepts in conventional optics such as reflection, dispersion, and scattering were all linear in nature. The interaction of intense pulses with matter led to various exotic, nonlinear phenomena. The first nonlinear phenomenon was observed when a pulsed laser beam was sent into a piezoelectric crystal, leading to the observation of the second harmonic generation (SHG) at an optical frequency. Many other phenomena such as frequency mixing, optical rectification, parametric amplification etc. have since been discovered.

For understanding the microcosm, apart from examining ever smaller structures, another pursuit of mankind has been to examine ever faster phenomena. The journey which began by taking the snapshot of motion of a horse has now reached the point of taking snapshots of the motion of electrons. The discovery of the laser was a major leap in this journey. Shortly after the discovery of continuous monochromatic laser beams, pulsed laser bursts were produced. These bursts continued advancing to shorter and shorter pulse duration from the picosecond to femtosecond and further. Currently, femtosecond lasers are commercially available and serve as a workhorse for most optics laboratories worldwide. Examples of phenomena which are now observable thanks to these super short pulses are the rotational dynamics of molecules, which take place in the picosecond regime, and vibrational dynamics, which take place in the femtosecond regime. The processes of bond formation and dissociation can be understood as vibrational dynamics. In the femtosecond regime, the motion of the nucleus is negligible and the vibration of electrons within molecules can be studied. This provides the technique to study the processes of bond making, bond breaking, chemical reactivity and transition rates. Ahmed H. Zewail used the "concept" of flash photolysis (pump-probe), where a strong femtosecond pulse is used to excite the system in the study and a delayed pulse, called probe pulse, is used to capture the evolution at various time delays by observing the absorption or fluorescence signal this absorption may present. With this technique, the real-time electron motion in molecules could be observed. Zewail used systems with increasing complexity to establish the field of femtochemistry. The first work was done using cyanogen iodide (ICN), where dissociation was observed to produce free CN molecules after 200 fs. In the famous study of NaI molecules, the contribution of vibration states to non-adiabatic transition rates was studied. The Nobel Prize in Chemistry 1999 was awarded to Zewail "for his studies of the transition states of chemical reactions using femtosecond spectroscopy". During the same period, other phenomena were being observed in the field of light-matter interactions. Multi-photon ionization, above-threshold ionization and high harmonic generation led to the development of pulses with attosecond pulse duration. In high harmonic generation (HHG), the nonlinear polarization in the atoms of noble gases is induced by the intense laser field which leads to ionization, excursion and recollision of the electron from the parent atom. This process is so called the *three step model* and was first proposed by Paul Corkum.

The field of attosecond science first came into existence during the first years of the new millennium with the successful generation of extreme ultraviolet pulses with sub-

femtosecond duration [4, 5, 6]. These sub-femtosecond pulses were then used to study physical processes with attosecond time resolution. The orbital period of an electron in the ground state of a hydrogen atom is 150 as, according to Bohr's model. The unfolding of ultrashort attosecond pulses opened the door for the first time into real-time observation of electron dynamics. The major early works in the field of attosecond science included the lifetime measurement of inner-shell vacancies of Kr atoms [7], ultrafast control of electronic processes [8], imaging the molecular orbitals [9], time-resolved observation of laser-induced tunnel ionization of atoms [10] and electric charge transport through atomic layers of solids [11]. In 2004, the first direct measurement of a short pulse of a visible laser light wave was performed [12] with the concept of attosecond streaking. Ever since its first demonstration, this technique has been used as the main tool to characterize ultrashort pulses on a routine basis and serves as a benchmark for attosecond precision metrology. Attempts were also made to answer some of the fundamental questions in science such as the length of the delay during single photo-ionization processes [13]. The real motion of valence-shell electrons in atoms was observed [14] and delay in non-linear response of bound electrons were tracked [15]. Attosecond science during its first decade demonstrated the unique capabilities that can be provided by its primary tool, the sub-femtosecond pulse. Moving into its second decade, the field is now delving deeper into increasingly fundamental questions and increasingly complex systems such as molecules and solids.

High harmonic generation, is a typical feature of strong field interactions and is the process at the heart of attosecond pulse generation. In 2011, HHG was extended to bulk crystalline materials such as ZnO [16] with mid-infrared frequency pulse, GaSe [17] with THz pulse and SiO<sub>2</sub> with optical pulses. The tools developed to understand electron dynamics in gases can now be used to understand much more sophisticated dynamics in solids. This motivation kindled a plethora of investigations demonstrating HHG in various dielectrics and semiconductors, establishing this process as a ubiquitous phenomenon [17, 18, 19, 20, 21, 22, 23, 24, 25]. The harmonic generation mechanism was explained using the Bloch equation [19, 17], semiconductor Bloch equations [26], time-dependent perturbation theory [27] and ab-initio calculations. A universal understanding of the mechanism in all insulators and semiconductors remains elusive. Experimental and theoretical works have debated the dominant mechanism of HHG in solids [28].

Understanding electron motion in the periodic structure of solids under ordinary electric field was one of the major breakthroughs in the last century of physics, which led to the invention of all the electronics we use in our day-to-day lives. The invention of intense and ultra-short pulses now provides us with "new eyes" to peer deeper into the electronic and optical properties of a material without destroying them. The phenomenon of HHG in solids [29] is the result of the interaction of electrons driven by short pulses with the periodic potential of the solids. Such interactions embody the information about the potential structure of solid. Initial research was conducted with the goal of determining fundamental features of a crystal such as its band structures using HHG [18]. Understanding the phenomenon of HHG can not only provide us with access to the dynamics of an electron inside solids but also access to the underlying valence periodic potential on which it is traversing. This is also the motivation and the main research question of this thesis.

Mapping atomic arrangement is a century-old science. The importance of crystallography can be gauged by the path-breaking discoveries done in the field, which has earned its biggest contributors 29 Nobel prizes. For bulk periodic or crystalline materials X-ray or electron beams can be used to decipher the crystalline arrangement and thereby map the electron density. However, even with these techniques at hand, the direct visualization of the electronic potential and valence electron densities inside solids remains an insurmountable challenge. X-ray diffraction patterns only contain the amplitude information and hence suffer from a poor final reconstruction of electron density due to ambiguity in phase information. Aron Klug realized that electron microscopy, however, does contain this phase information and was awarded Nobel Prize in 1982 for using it to elucidate the structure of protein complexes [30]. However, electron diffraction requires very thin samples to mitigate the effects of multiple scattering and is also very sensitive to space charge effects. A robust technique which can look into valence electron densities and provide information of both amplitude and phases of the electron density components is much needed.

This work presents experiments in which intensities of emitted harmonics were carefully measured and characterized for different orientation of the crystal. Theoretical concepts were developed for extracting the information of valence electron densities from the intensity and angular dependence of the obtained data. The valence electron densities of  $\text{MgF}_2$  and  $\text{CaF}_2$  were successfully extracted and compared with the existing theoretical model. The contents of the thesis are briefly outlined below.

- Chapter 1 presents a brief review of the current methods used to visualize matter to the smallest possible scale.
- In Chapter 2 the features of HHG in solids are discussed. Most widely accepted existing theoretical frameworks to understand the HHG phenomenon in solids are briefly presented.
- Chapter 3 discusses the foundation of picoscopy. It shows how the high harmonic generation process can be discussed without invoking the band picture. It first argues that in the high-frequency regime the motion of an electron in solids can be treated similarly to the motion of a nearly-free electron in the laser field, where the potential only acts as a perturbation. Based on this, a theory to understand HHG in solids which connects the intensity of emitted harmonic radiation with the Fourier coefficients of the valence potential of the periodic crystal is discussed.
- Chapter 4 presents analogies and differences between the intensity of emitted harmonics in the HHG process and the intensity of the diffracted X-rays in crystallography.
- Chapter 5 presents the methods for analyzing the experimentally obtained intensity yield of emitted harmonic radiation. It discusses how the amplitude and phase of the Fourier coefficients of the periodic crystal can be obtained from the intensity yields. It also details the method to obtain the 2D images of valence electron density.

- 
- Chapter 6 presents the experimental setup. Essential elements for developing a picoscope are first identified and the apparatus of the picoscope is presented.
  - Chapter 7 interrogates the validity of high-frequency approximation in solids by probing the valence radii of ions/atoms in the various crystalline system such as  $\text{MgF}_2$ ,  $\text{MgO}$ ,  $\text{ZnO}$ ,  $\text{SiO}_2$ ,  $\text{SiC}$  and Diamond.
  - Chapter 8 presents experiments and analysis to measure the valence potential of crystalline  $\text{MgF}_2$ . The two-dimensional slice of the valence potential of  $\text{MgF}_2$  is reconstructed and compared with the potential obtained from density functional theory.
  - Chapter 9 extends the experiment and analysis to the crystal of  $\text{CaF}_2$  and presents its experimentally measured valence electron potential.
  - Chapter 10 presents the conclusions and the outlook.



# Chapter 1

## Visualizing the microcosm

*From seeing too much of the world, We do not understand it.  
There is something unknown in knowing. Unfaith is what keeps the faith going.*

-Richard Eberhart

A human eye is the result of a million years of evolution. Although it is one of the most complex organs in a human body still its spatial and temporal resolutions are limited to about  $100\ \mu\text{m}$  and few milliseconds. Today, we are assisted by several tools which can observe in angstrom scale or can examine the motion up till attosecond duration. In this chapter, the current methods for observing matter to its minutest scale are reviewed.

### 1.1 Ways to determine the crystal structure of matter

The obvious way of determining the crystal structure is to magnify the objects to the size such that the human eye can understand and resolve them. With this aim, the field of microscopy and crystallography evolved and can currently resolve the molecules of nm size.

Crystalline material can either be resolved by magnifying its image or by knowing its Fourier coefficients. The latter part is done through the process of diffraction which gives us the information of the amplitude of the Fourier coefficients of the crystalline material.

Fig. 1.1 succinctly explains the two methodologies. In the case of microscopy, the image in real space is magnified to resolve finer features. On the other hand, in crystallography, the Fourier coefficients are obtained and the real space image is reconstructed. The first microscope was developed in 1600 by Antonie van Leeuwenhoek also known as “the father of microbiology”. He recorded the minute details in natural samples using a simple lens microscope.

The field of crystallography, on the other hand, is a century old. It started with the discovery of X-rays and is currently the most widely used method to determine the structure of the crystalline material. In the following, we will first review the important microscopy methods and then look at the fundamentals of crystallography.

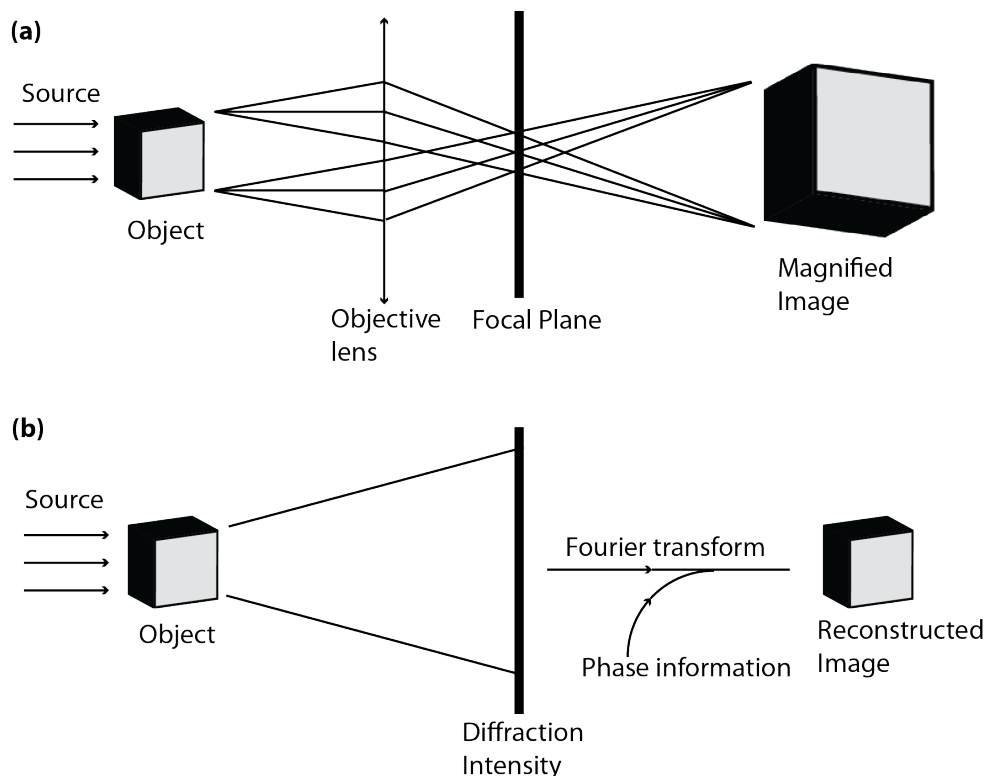


Figure 1.1: (a) Illustrates the principles of microscopy. The object is magnified using an objective lens. (b) Illustrates the principle of X-ray crystallography. A source containing photon(X-rays), electrons or neutrons gets diffracted by the crystalline object. The diffraction peaks are recorded and along with the phase information obtained by other sources the final image is reconstructed by Fourier transforming the diffraction peak amplitude along with correct phases.

## 1.2 Microscopy

The most widely used microscopy techniques are presented below along with their advantages, disadvantages and present resolution power.

### 1.2.1 Optical microscope

Developed in 17<sup>th</sup> century, this is the most widely used form of microscopy. Fig. 1.1 describes the basic principle of optical microscopy. It is extensively used in microbiology, mineralogy, pharmaceutical research, etc. The major limitation of optical microscopy is that the resolution is diffraction limited [31]. The resolution  $d$  of the microscope can be stated as:

$$d = \frac{\lambda}{2NA} \quad (1.1)$$

Optical	X-ray	Electron	Probe	Acoustic	Neutron
Simple	Scanning transmission X-ray microscope	Transmission electron microscope	Scanning tunnelling microscope	Scanning acoustic microscope	Neutron microscope
Compound	Transmission X-ray microscope	Scanning electron microscope	Atomic force microscope	Confocal scanning acoustic microscope	
Stereoscopic	Photoemission electron microscope	Scanning tunneling electron microscope	Magnetic force microscope		
Confocal		Reflection electron microscope	Chemical force microscope Electrostatic force microscope		

Table 1.1: Summary of microscopy techniques.

where  $\lambda$  is the wavelength of the light source and NA is the numerical aperture of an objective lens which describes the range of angle over which the system can emit or accept light. In 2014 E. Betzig, W. Moerner and S. Hell were awarded the Nobel prize in chemistry for the development of super-resolved fluorescence microscopy which increases the resolution of the optical microscopy to nm scale [32].

### 1.2.2 X-ray microscope

It is based on the principle of contrast imaging where the difference in absorption of X-rays in water window region (280-530 eV) and by carbon and oxygen atoms are used to map the image of the object. They are widely used for medical applications. The resolution of X-ray microscopes lies between optical microscopes and electron microscopes.

### 1.2.3 Electron microscope

First built in 1933 by Ernst Ruska, electron microscopes are similar to optical microscopes and also rely on the principle of magnifying the image to observe the matter but with electrons instead of photons. The wavelength of an electron can be hundreds of thousands of times shorter than visible light photons and hence have higher resolving power. These microscopes have reached up to 50 pm resolution.

### 1.2.4 Scanning probe microscope (SPM)

In 1981 Gerd Binnig and Heinrich Rohrer demonstrated that the surface topology of material could be mapped using a scanning tunnelling microscope (STM) [33]. With this, a new branch of microscopy known as scanning probe microscopy emerged. Herein, the images of the surfaces are obtained using a physical probe. The image is formed by raster scanning a probe tip on the surface of the material. The value of the probe is recorded at discrete points which depends on the type of microscope and the mode of operation. Using these recorded values the image of the surface is obtained.

**Advantages:** The resolution of SPM depends on the interaction volume of the probe and surface which can reach a picometer scale. Hence very fine features of the surface can be resolved by such a technique. This microscopy technique does not require high vacuum conditions.

**Disadvantages:** This technique can only be used to look into surfaces and not in bulk hence also requires sensitive sample preparation techniques. The knowledge of the shape of the scanning probe, which is difficult to determine, is essential for the correct measurement of the surface's topology. Being a scanning technique the procedure is inherently time-consuming and can only be used to measure a small portion of the surface. Moreover, the inherent assumption in the technique is that while rastering the surface is stationary however effects like specimen drift, vibrations etc may affect the obtained image.

### Scanning tunneling microscopy (STM)

STM is widely used to image a surface at an atomic level. They can be used at a wide range of temperature and pressure. The principle behind STM is that they measure the differential change in tunneling current given a differential change in voltage  $\frac{dI}{dV}$ . This quantity is proportional to the local density of state of the surface and provides information about the LDOS with a few hundreds of picometer resolution.

### Atomic force microscopy (AFM)

AFM uses a precisely fabricated tip placed on a cantilever which rasters over the surface of the material. A laser beam is reflected from the cantilever and detected by the quadrant photo-diode. As the position of the cantilever changes, while mapping the topology of the surface, the laser beam is deflected at different positions of the quadrant photodiode, which is correlated to the properties of the surface. The properties of the probe, cantilever and their alignment, affects the final reconstruction. AFM can reach a sensitivity of 10 pm. Highly sensitive alignment procedure along with sensitivity to thermal drifts make this technique very difficult [34].

## 1.3 Crystallography

Crystallography is now a century old science, the impact of which can be gauged from the fact that 29 Nobel prizes [35] have been awarded for scientific achievements related to, or involving the use of crystallography. Also, in a comment written on 100 years of this field [36], Robert Crease describes the discovery of X-ray diffraction in crystals as “the amazing turning point” and “central event” in modern physics. It has transformed our understanding of nature by revealing the structure of materials down to the Angstrom scale. The birth of this field could be attributed to the discovery of X-rays by Wilhelm Röntgen in 1895. Since then there has been a series of regular advancements in the field, some of which are chronologically mentioned in Fig. 1.2. In this section, the conventional crystallographic methods are briefly touched upon, and the importance of crystallography for understanding the structure and dynamics of the matter is explained. The procedure to obtain the total electron density from the diffraction data is also briefly touched upon.

### 1.3.1 X-ray crystallography and its principles

The aim of crystallography is to resolve the crystal structure of a material, i.e., to determine the precise arrangement of all atoms along with their electron density inside a molecule or periodic crystal. The knowledge of the precise crystal structure and atomic arrangement provide access to a large range of information such as bond length, bond angles and other chemical and optical properties of the materials [37, 38]. The interatomic distance is around 100 - 300 pm for most molecules and solids. To observe such small features, one needs the light wavelength of the comparable order. The photon energy of such light

<b>X-ray diffraction</b>	<b>Electron diffraction</b>	<b>Neutron diffraction</b>
<p>X - ray diffraction uses high energy photons to diffract from the electrons of the matter and hence provide information about the <b>total electron density</b></p>	<p>Electrons are charged particle and interact with material through the Coulomb forces. They are sensitive to both protons and electrons in the matter and hence probe the <b>total charge density</b>.</p>	<p>Neutrons being the neutral particle interacts with the <b>atomic core</b> through strong nuclear forces and hence are useful in differentiating isotopes. In addition, they also interact with the magnetic fields as they have non zero <b>magnetic moments</b> and can be used to study wide variety of magnetic phenomenon.</p>
<p>For 1Å resolution, X-ray requires <b>1000 eV</b> energy</p>	<p>For 1Å resolution, electron beam requires <b>40 eV</b> energy</p>	<p>For 1Å resolution, Neutron beam require <b>0.08 eV</b> energy</p>
<p>Normal penetration</p>	<p>Less penetration</p>	<p>High penetration</p>

Table 1.2: Diffraction techniques and their properties.

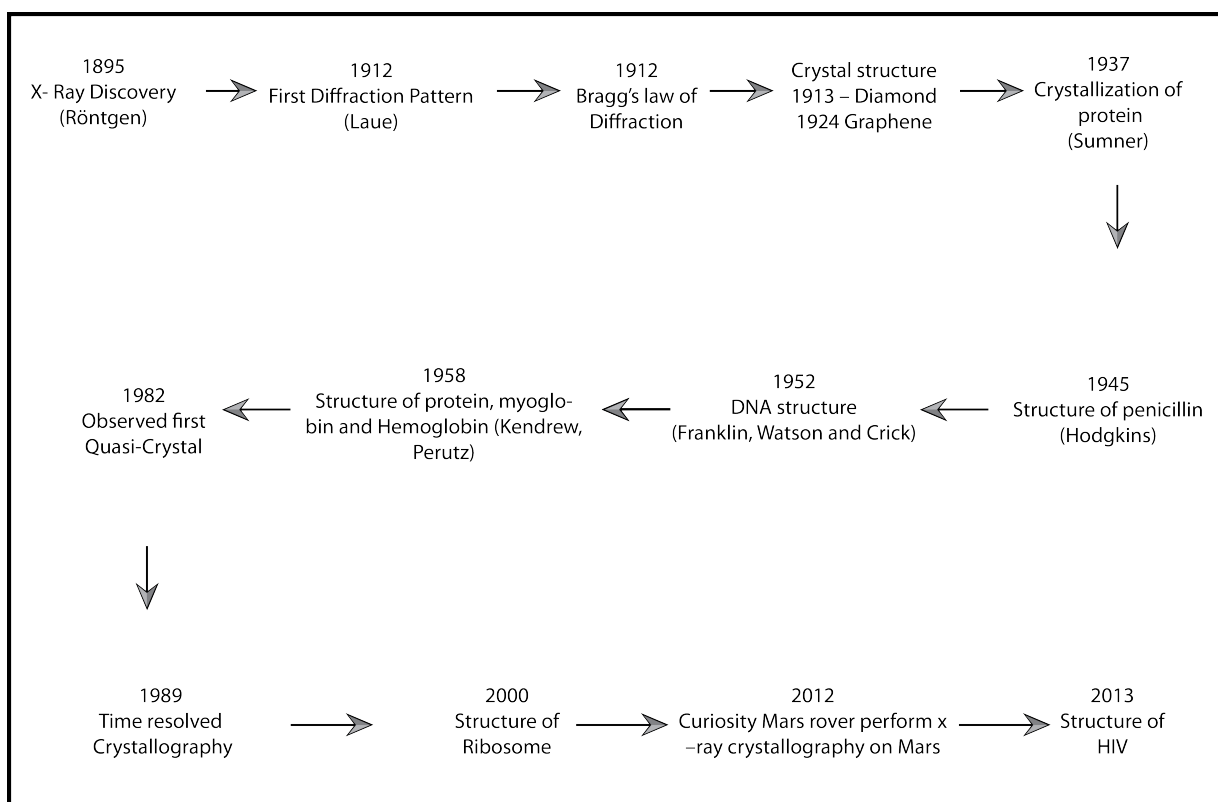


Figure 1.2: Chronological milestones in crystallography.

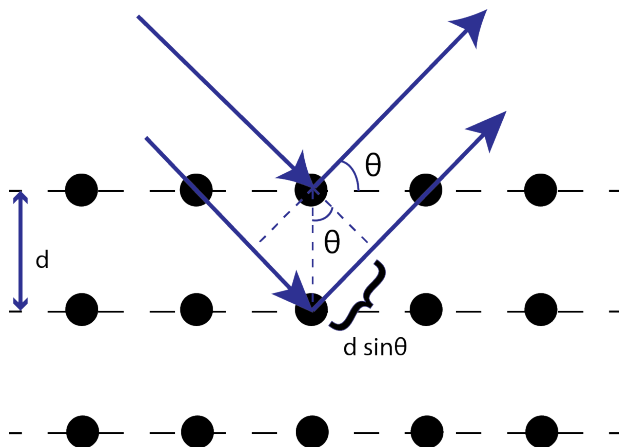


Figure 1.3: Schematic depiction of Bragg's law.

would be  $\hbar\omega = \frac{hc}{\lambda} = hc/1e^{-10} \sim 12.3 \times 10^3 eV$ , which is characteristic of X-rays. Thus, the discovery of X-rays paved the way to the direct observation of features on such small length scales. X-rays of commensurate wavelengths would diffract from the material revealing the interatomic distance. Two equivalent points of view are used to understand the scattering of X-ray from a crystalline structure, one provided by Bragg and another from Laue. Although both viewpoints are well described in the literature, we will still review the salient points from both of them. This will later help us understand the analogies between conventional crystallography, and picoscopy presented in this thesis.

### Bragg formulation of diffraction

William Bragg and Lawrence Bragg realized that when X-rays are diffracted from a crystalline material, very sharp peaks are observed, for a given incident wavelength and direction, which was in contrast to those produced from X-ray diffraction with liquids. They accounted for this by considering the crystal to be made of a periodic arrangement of atoms, in contrast to liquids, and specular reflection from these periodically arranged layers constructively interfere to produce a sharp diffraction peak.

The specular reflections from two consecutive planes in a crystal have a path difference of  $2d\sin(\theta)$  where  $\theta$  is the angle of incidence of the X-ray beam and  $d$  is the distance between two planes. If the path difference between specular reflection from two planes is an integral multiple of the wavelength of incident pulse ( $n\lambda = 2d\sin(\theta)$ ), then the interference between these two reflections will be constructive leading to a sharp peak at an angle theta from the crystal plane. The integer  $n$  is the order of the corresponding reflection. Thus, one plane configuration( $d$ ) can give multiple (higher order) reflections. Also in a crystal, depending on the orientation, several choices of sets of planes ( $ds$ ) are possible. By measuring the angle of reflection from the crystal and the order of reflection one can obtain the characteristic distance between two planes, yielding the first insight into inter-atomic distances.

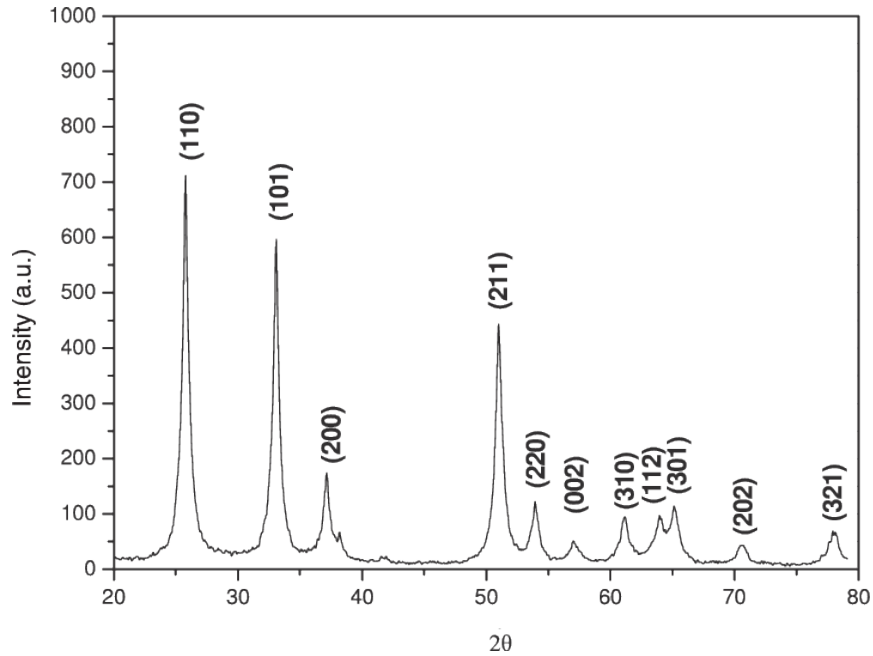


Figure 1.4: Diffraction pattern of a powdered sample. Each peak is labeled with a Miller index. Figure reproduced from the *Journal of the Korean Physical Society*, Vol. 53, No. 6, 2008, pp. 3588-3592.

### Von Laue formulation of diffraction

Max Von Laue, who was working in Arnold Sommerfelds Institute for Theoretical Physics in Ludwig-Maximilians-Universität, prompted by discussion with Peter Paul Ewald started studying X-ray diffraction from crystals and formulated a new approach for understanding diffraction. In this approach, no particular sectioning of the crystal is assumed. To obtain constructive interference, the Laue condition requires that the change in wave vector or incident and outgoing wave must be equal to the vector of the reciprocal lattice. This means that an incident wave vector will only then satisfy the Laue condition if the tip of this vector falls on a Bragg plane (the plane forming the boundary of the Brillouin zone).

### Inverse problem: Diffraction data to real image

The scattering of X-rays from atoms produces a diffraction pattern, which itself contains the information about the atomic arrangement of the crystal. The diffraction pattern from a powdered sample is displayed in Fig. 1.4.

Each diffraction peak is labeled with Miller indices  $(hkl)$ . They are used to identify different plane of atoms which assist in analyzing the crystal structure and denote family of planes orthogonal to  $h\mathbf{b}_1 + k\mathbf{b}_2 + l\mathbf{b}_3$  where  $\mathbf{b}_i$  are the basis vectors of reciprocal space. The Intensity of the diffracted peak is given by

$$I_{hkl} \propto |F_{hkl}|^2 \quad (1.2)$$

where,

$$F_{hkl} = \sum_{j=1}^m N_j f_j \exp[2\pi i(hx_j + ky_j + lz_j)] \quad (1.3)$$

where  $(x_j, y_j, z_j)$  represents the coordinates of the atoms,  $F_{hkl}$  is the structure factor,  $N_j$  is the fraction of every equivalent position that is occupied by atom  $j$  and  $f_j$  is the scattering factor which quantifies the efficiency of scattering by electrons. The structure factor  $F_{hkl}$  sums the scattering from all atoms in a unit cell.

The intensity of the diffracted peak is used to obtain the relevant structure factor. However, the hurdle in obtaining the correct structure factor values is the knowledge of phase which is lost in the intensity information. This is famously known as the **Phase problem** [39, 40]. Currently, various numerical and mathematical techniques are used to obtain the phase and retrieve the structure of the material.

## 1.4 Towards picoscopy of valence electrons

A Holy Grail of the ultrafast science is the direct, real-time imaging of valence electron densities. Constant development is made to step towards this goal. Optical microscopy techniques do not have enough sensitivity to probe the electron densities in a linear regime as they are restricted by the diffraction limit, However, the resolution increases dramatically in the non-linear regime. Using the non-linear mixing of X-rays and optical waves attempt had been made to probe valence electron density [41]. THz fields were used to nonlinearly drive the lattice vibration in solids to probe the inter-atomic potential. In gases, non-linear interaction of atoms and molecules with intense laser field was used to reconstruct the valence orbitals [42, 9, 43] and their dynamics[44].

This thesis is aimed at imaging valence electron distribution of solids for which a new kind of microscopy is developed which is termed as picoscopy. The development of a Picoscope require some fundamental conditions to be fulfilled so as to allow for the sub-angstrom scale imaging.

- **SENSITIVE** The probing tool must be sensitive to the valence electrons. Currently, available techniques are only sensitive to the core electrons of the potential. The extraction of the valence electron density from the measurements which are sensitive to the core electrons is challenging since the valence electrons are significantly less compared to core electrons.
- **FAST** The probing of the system must occur on time scales faster than the internal time scales such as rotational, vibrational, thermal motions etc. to obtain the maximum spatial resolution. Ultrafast pulses have made this possible in atomic and molecular systems by allowing the mapping of valence electron motion [14]. The ultrafast pulses used in our experiments to generate the HHG signal ensure that the probe is faster than the internal dynamics.

- **PHASE** Complete imaging of the potential not only requires the information of the amplitude of the Fourier coefficients of the potential but also the information of the phase of the Fourier coefficients. Currently, the experimental techniques are unable to directly access the phase information of crystalline materials. To image the valence density of material only from the experimental data, a device which can measure both amplitude and phase of the coefficients is required.

The developments in ultrafast optics coupled with the capabilities provided by the high harmonic generation in solids now allow us to fulfill all the critical conditions mentioned above. The non-linear interaction of intense laser field with the crystal structure has led to the generation of high harmonics in solids. This interaction can be leveraged to obtain the valence electron density and develop picoscopy of valence electron density. In the following chapter, we first describe the current models to understand HHG in solids and later using a semiclassical approach and without invoking band picture, we show how picoscopy emerges!



# Chapter 2

## Strong field physics

The invention of the laser [45], a device producing intense coherent electromagnetic fields, has paved the way for the investigation of nonlinear light-matter interactions. Before the invention of the laser, solely the linear interactions of light with matter and the concurrent phenomena such as reflection, refraction, interference were understood and studied [46]. In its simplest form, the non-linear interaction can be described by a Taylor-series expansion:

$$P(E) = \epsilon_o(\chi^{(1)}E + \chi^{(2)}E^2 + \chi^{(3)}E^3 + \dots) \quad (2.1)$$

Here  $P$  is the polarization,  $\epsilon_o$  is the vacuum permittivity,  $\chi$  is the electric susceptibility and  $E$  is the electric field. In the non-linear light-matter interaction, the optical properties depend on the intensity of the field. This leads to the observation of important nonlinear phenomenon such as second harmonic generation(SHG) [47], sum and difference frequency generation, wave mixing, non-linear refraction and absorption etc.

### 2.1 High harmonic generation (HHG) in gases

High harmonic generation is a highly non-perturbative process. An intense laser pulse ionizes the atoms which in turn emit electrons. This electron accelerates in the laser field, returns when the field direction changes, and with some finite probability recombines with the parent ion radiating a photon of higher energy. This picture is famously known as the *three-step model*[48]. During the re-collision process, the electron emits a high energy photon corresponding to the energy it has acquired during its excursion. More precisely, the energy of the emitted photon is given by  $I_p + 3.17U_p$  [49], where  $I_p$  is the ionization potential and  $U_p$  is the ponderomotive energy. Depending on the number of cycles in the driving pulse, each sufficiently intense half-cycle may produce a burst of XUV light, resulting in an attosecond pulse train. Moreover, few-cycle pulses can be used to obtain the isolated attosecond pulses [50].

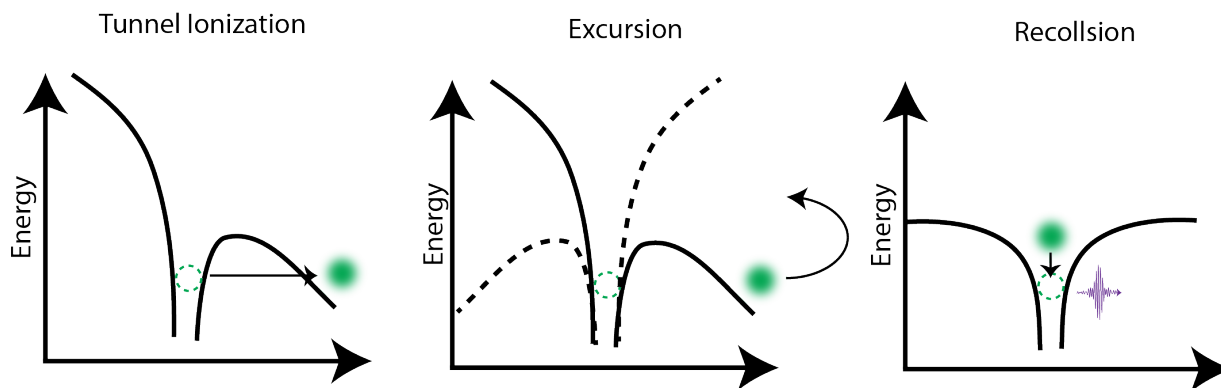


Figure 2.1: The three-step model of HHG in gases. The exciting field bends the potential so as to facilitate tunnel ionization. The resulting free electron is driven by the laser field. As the field reverses its direction the electron re-collides with the parent ion, emitting a high energy photon.

## 2.2 High harmonic generation in solids

The density of electrons at the surface of a solid is much larger than the atoms. Hence, it was of equal interest to investigate the generation of harmonics by shining laser light on a solid. High harmonic phenomenon was first extended to metals surface[51] and recently to bulk semiconductors and dielectrics [52]. With the discovery of HHG in bulk solids, the tools developed to understand electron dynamics in gases could be used to understand more sophisticated dynamics in solids. This motivation kindled a plethora of investigations demonstrating HHG processes in various dielectric and semiconductor materials [17, 18, 19, 20, 21, 22, 23, 24, 25]. In these works, the strong field induced currents[53, 54, 55] and the process of HHG was explained by using perturbative concepts[55, 56, 57] developed earlier for gas phase physics.

## 2.3 Major models of HHG in solids

The first intuitive explanation was provided in terms of a single band motion known as intraband motion of electrons in solids (Bloch oscillations) [16, 58]. A more microscopic theory which took into account both valence and conduction bands, known as the semiconductor Bloch equations was then proposed [17, 59]. Analogous to HHG in gases, HHG in solids was attempted to be explained in terms of a recollision-based model [21, 60]. A real space semi-classical analysis predicting electron trajectory in a unit cell was also presented [61]. More descriptive, quantum mechanical solutions of the time-dependent Schrödinger equation [27] and ab-initio methods [62] have also been presented.

### 2.3.1 Bloch oscillations

The simplest model for HHG in solids was explained using the Bloch oscillation. An electron wave packet is driven by a laser field in a non parabolic band dispersion of a conduction band of the solid. The dynamics of the wave packet in the reciprocal space can be calculated using the usual classical equation of motion for a particle with the crystal momentum  $\hbar\mathbf{k}$ , given as  $m\dot{\mathbf{r}} = \hbar\dot{\mathbf{k}} = \mathbf{F}$ . In the presence of an electromagnetic field with electric component  $\mathbf{E}$  and magnetic component  $\mathbf{B}$ , the equation becomes  $\hbar\dot{\mathbf{k}} = -e(\mathbf{E} + \frac{1}{c}\mathbf{v} \times \mathbf{B})$ . In this thesis we will remain in the non-relativistic regime and hence neglect the magnetic field. The equation then reduces to

$$\frac{d\mathbf{k}(t)}{dt} = -\frac{e}{\hbar}\mathbf{E} \quad (2.2)$$

The above equation is also known as the acceleration theorem which suggests that the external field changes the crystal momentum of the particle. For constant field strength the solution of this equation is  $k(t) = k(0) - \frac{eE}{\hbar}t$ . The dynamics in k-space mirror exactly the vector potential  $A(t) = \int E(t)dt = Et$ . However, it folds into the first Brillouin zone by Bragg reflecting at the zone boundary. Given the dispersion of the conduction band  $\epsilon(\mathbf{k})$ , the group velocity of the electron wave packet is given by

$$v_g(\mathbf{k}) = \frac{1}{\hbar} \frac{\partial \epsilon(\mathbf{k})}{\partial k} \quad (2.3)$$

Where, in the tight-binding model, the band dispersion ( $\epsilon(\mathbf{k})$ ) can be defined as  $\epsilon(\mathbf{k}) = \Delta \cos(kd)$ . Hence the group velocity  $v_g(k) = -\frac{\Delta d}{\hbar} \sin(kd)$  and the electron position  $x$  using Eq.2.2 comes out  $x(t) = \int_0^t v(\mathbf{k}(t'))dt' = x(0) - \frac{\Delta}{eE} \cos(\frac{deE}{\hbar}t)$ . Clearly we observe that eventhough a unidirectional constant electric field acts on electron wave packet, it oscillates in the real space. This non-intuitive phenomenon is known as **Bloch oscillation**. The frequency of oscillation is known as Bloch frequency and is given by  $\Omega_B = \frac{edE}{\hbar}$  which is proportional to the static electric field.

### HHG from Bloch Oscillations

In the semi-classical approach, instead of assuming a classical particle we assume some initial distribution of the electrons  $f(\mathbf{k}, t)$  and also instead of a constant electric field we assume an oscillating electric field. Then, the dynamics in the presence of an electric field is given by the Boltzmann equation [63].

$$\frac{\partial f(\mathbf{k}, t)}{\partial t} = -\frac{e}{\hbar}\mathbf{E}(t) \frac{\partial f(\mathbf{k}, t)}{\partial \mathbf{k}} \quad (2.4)$$

with the solution given by:

$$f(\mathbf{k}, t) = f(\mathbf{k} + \frac{e}{\hbar}\mathbf{A}(t), 0); A(t) = - \int_{-\infty}^t \mathbf{E}(t')dt' \quad (2.5)$$

Here  $A(t)$  is the vector potential of the electric field. Evidently, the initial distribution of charge is merely translated in reciprocal space by the vector potential, while the shape of the distribution remains unchanged. The electron wavepacket traverse in the anharmonic dispersion of the conduction band which can be decomposed into its Fourier components. The acceleration of the electron wavepacket on the band dispersion can then be understood as its motion on these individual Fourier components which leads to the generation of HHG. The accelerating electron wave packet generate current density given by  $J(t) \propto e \int_{-pi/d}^{pi/d} v_g(\mathbf{k}) f(\mathbf{k}, t) d\mathbf{k}$ . The source of radiation in the wave equation  $\partial j(t)/\partial t$ , hence the spectrum of the emitted radiation can be calculated from  $I_{rad} \propto |\omega j(\omega)|^2$ . This picture is based on the assumption that pre-excited carriers are present in the conduction band of solids. For a complete description of the HHG process, one must also account for the transition of carriers from valence to conduction band.

### 2.3.2 Semiconductor Bloch equations

Semiconductor Bloch equations (SBE) takes into account both the excitation process within the band and dynamic of the electron inside individual bands. We will here sketch the multi-band SBE approach and understand how different interactions play a role in HHG. Only critical steps are outlined. A more comprehensive derivation can be found in reference[26, 64].

A general many-body Hamiltonian in second-quantization for the electronic system (neglecting defects and electron-phonon interactions) is given as [59]

$$\begin{aligned} \hat{H} &= \hat{H}_o + \hat{H}_v + \hat{H}_{ls} \\ \hat{H} &= \sum_{\lambda, \mathbf{k}} \varepsilon_{\mathbf{k}}^{\lambda} \hat{\mathbf{a}}_{\lambda, \mathbf{k}}^{\dagger} \hat{\mathbf{a}}_{\lambda, \mathbf{k}} + \frac{1}{2} \sum_{\lambda \lambda'} \sum_{\mathbf{k}, \mathbf{k}'} \sum_{q \neq 0} \mathbf{V}_q^{\lambda \lambda'} \hat{\mathbf{a}}_{\lambda, \mathbf{k}}^{\dagger} \hat{\mathbf{a}}_{\lambda', \mathbf{k}'}^{\dagger} \hat{\mathbf{a}}_{\lambda', \mathbf{k}'+q} \hat{\mathbf{a}}_{\lambda, \mathbf{k}-q} - \mathbf{E}(t) \sum_{\lambda, \lambda' > \lambda, k} (\mathbf{d}_{\mathbf{k}}^{\lambda \lambda'} \hat{\mathbf{a}}_{\lambda, \mathbf{k}}^{\dagger} \hat{\mathbf{a}}_{\lambda', \mathbf{k}} + c.c). \end{aligned} \quad (2.6)$$

Where  $\hat{\mathbf{a}}_{\lambda, \mathbf{k}}^{\dagger}$  and  $\hat{\mathbf{a}}_{\lambda, \mathbf{k}}$  denotes the creation and annihilation operators for an excitation of momentum  $\mathbf{k}$ . The Hamiltonian is divided into three components. The first term describes an electron in a band structure with energy  $\varepsilon_{\mathbf{k}}$ . The second term describes the Coulomb interaction between electrons either in the same band or in different bands.  $\mathbf{V}_q$  are the Fourier coefficients of the real space Coulomb potential. The third term is the laser-solid interaction where the electron is annihilated from one of the bands and created in another band. All terms except the Coulomb interaction terms have two operators. When we write the equations of motion, these operators recursively increase and end up in infinite hierarchy of coupled differential equations. In order to truncate this and obtain closed set of differential equations we make the random phase approximation i.e,  $(\langle \hat{\mathbf{a}}_{\lambda, \mathbf{k}}^{\dagger} \hat{\mathbf{a}}_{\lambda, \mathbf{k}'}^{\dagger} \hat{\mathbf{a}}_{\lambda, \mathbf{k}} \hat{\mathbf{a}}_{\lambda, \mathbf{k}'} \rangle \rightarrow \langle \hat{\mathbf{a}}_{\lambda, \mathbf{k}}^{\dagger} \hat{\mathbf{a}}_{\lambda, \mathbf{k}'}^{\dagger} \rangle \langle \hat{\mathbf{a}}_{\lambda, \mathbf{k}} \hat{\mathbf{a}}_{\lambda, \mathbf{k}'} \rangle - \langle \hat{\mathbf{a}}_{\lambda, \mathbf{k}}^{\dagger} \hat{\mathbf{a}}_{\lambda, \mathbf{k}} \rangle \langle \hat{\mathbf{a}}_{\lambda, \mathbf{k}'}^{\dagger} \hat{\mathbf{a}}_{\lambda, \mathbf{k}'} \rangle + \langle \hat{\mathbf{a}}_{\lambda, \mathbf{k}}^{\dagger} \hat{\mathbf{a}}_{\lambda, \mathbf{k}} \rangle \langle \hat{\mathbf{a}}_{\lambda, \mathbf{k}'}^{\dagger} \hat{\mathbf{a}}_{\lambda, \mathbf{k}} \rangle)$

The expectation value of these two operators are either population ( $f_{e,h}$ ) or polarization ( $p_{\lambda\lambda'}$ ) of electrons/holes. Specifically,  $f_e = \langle \hat{\mathbf{a}}_{e, \mathbf{k}}^{\dagger} \hat{\mathbf{a}}_{e, \mathbf{k}} \rangle$ ,  $f_h = \langle \hat{\mathbf{a}}_{h, \mathbf{k}}^{\dagger} \hat{\mathbf{a}}_{h, \mathbf{k}} \rangle$ ,  $p_{he} = \langle \hat{\mathbf{a}}_{h, \mathbf{k}}^{\dagger} \hat{\mathbf{a}}_{e, \mathbf{k}} \rangle$ ,

$p_{ee'} = \langle \hat{\mathbf{a}}_{e,\mathbf{k}}^\dagger \hat{\mathbf{a}}_{e',\mathbf{k}} \rangle$ ,  $p_{hh'} = \langle \hat{\mathbf{a}}_{h,\mathbf{k}}^\dagger \hat{\mathbf{a}}_{h',\mathbf{k}} \rangle$ , with e and h denoting electron and hole band indices. With the above approximation the equation of motion in the Heisenberg picture can be solved to obtain the set of coupled differential equations, known as semiconductor Bloch equations (see Appendix A). Finally, the emitted harmonic field is evaluated as

$$E(t) = \frac{\partial}{\partial t} P(t) + J(t), \quad (2.7)$$

where  $P(t) = \sum \lambda \lambda' k p_{\lambda \lambda'}(k) d_{\lambda \lambda'}(k)$  is the total polarization, contributing to high harmonic due to interband motion of electrons and  $J(t) = \sum \lambda k f_\lambda(k) v_{g,\lambda}(k)$  is the total current, contributing to high harmonic due to intraband motion of electrons.

In the above picture, electrons are excited to higher bands due to its interaction with a laser pulse, leaving holes in the low lying valence bands. After traversing through these bands these electrons and holes pairs may recombine, emitting high-energy photons in the process. Such emission processes are denoted by interband HHG emission. Otherwise, there is the possibility that electrons, upon interaction with a laser pulse, accelerate in the anharmonic band of the solid, thus generating high harmonics (Fig .2.2). Dominant mechanics among the two is still being debated [65, 66, 67, 68, 69, 70]. The experiment performed with an optical driving field in the wide bandgap dielectric, quartz, showed Intraband picture to be the dominant mechanism [68].

### 2.3.3 Features of HHG in solids

In this section, by comparing the features of HHG in solids with that of well established and understood features of HHG in gases, our effort is to gain insight into HHG process in solids.

- **CUTOFF** The cutoff energy law is well established in gases where the cutoff energy is proportional to the intensity of the driving field and scales quadratically with the wavelength. It weakly depends on the ionization potential of the target gas atom. On the other hand, in solids the cutoff energy is observed to scale linearly with the field strength ( $E_o$ ) [16, 19, 17]. No agreement is being established on scaling of the cutoff energy with the wavelength. Some studies have claimed linear dependence [16, 63, 56, 72] on wavelength while others have claimed cutoff energies to be wavelength independent [27, 73]. A systematic study is at the moment absent. The cutoff energy in solids also strongly depends on the material properties such as the dispersion of the band. In the Bloch oscillation picture, the maximum cut off energy was found to be linked to the highest Fourier component of the band[74]. In the interband model, the cutoff energy is found to be limited to the maximum band gap of the material. This sets an upper bound, which can however be breached if higher bands are involved. In the HHG process, this phenomenon is predicted to be manifested as the multiple plateaus in the HHG signal [75] and was also experimentally observed in HHG emitted from a solid Ar [76]. However unlike gases where the prediction for

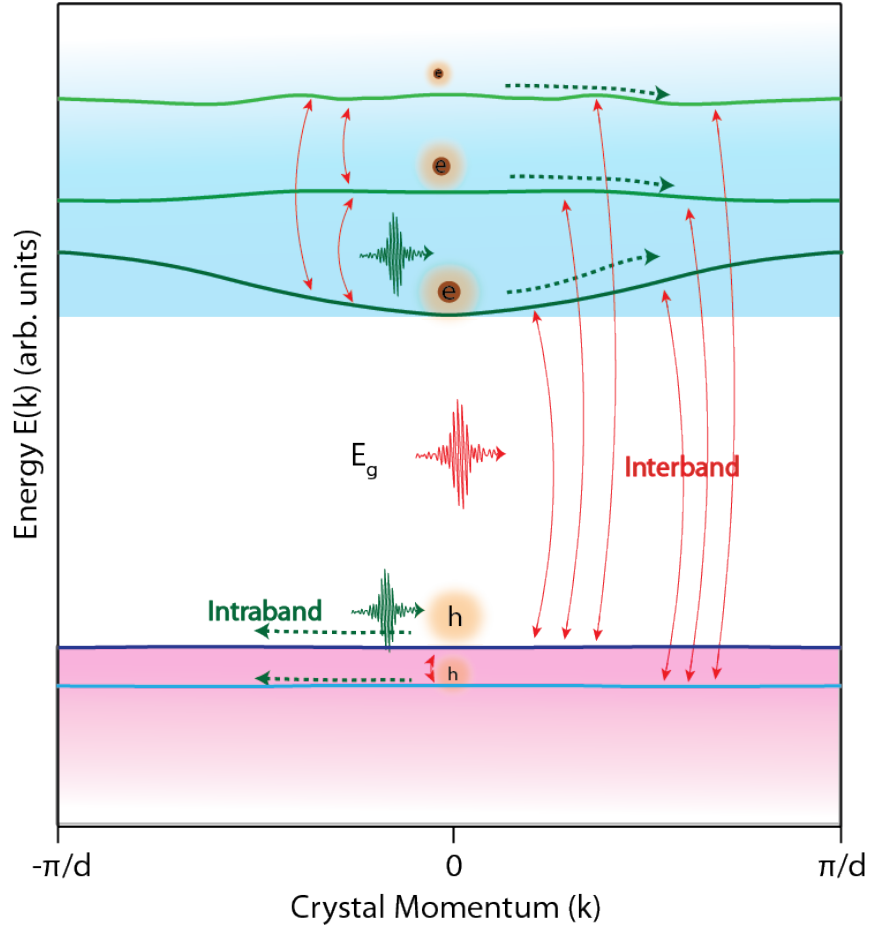


Figure 2.2: Interband and intraband mechanism of harmonic emission are schematically depicted. The valence bands are depicted by the blue coloured curves and conduction band by green coloured curves. The motion of carriers (electrons and holes) are depicted by the arrows. The shaded area (magenta and cyan) depict the density of states in the valence and the conduction bands respectively. Adapted from reference [71].

cut off energy is well established and is given by  $I_p + 3.17U_p$ , in solids a law for cutoff energy dependence of wavelength of the driver is still blurred.

- **ELLIPTICITY** HHG from gases shows a strong dependence on the ellipticity of the exciting field where small deviation from the linear polarization of the exciting pulse lead to a strong suppression of HHG signal. The circularly polarized driver completely prohibits the harmonic emission. This feature is often used to generate the isolated attosecond pulses by polarization gating [77] and double optical gating [78]. The initial experimental investigations in solids does not show a very strong dependence of emitted spectra on the polarization of the light [52, 79]. Unlike gases, the maximum intensity of harmonic emission in solids may not be from a linearly polarized driver but from an elliptically polarized driver [80]. Also, a circularly polarized driver may also generate the harmonic radiation from solids. Moreover, unlike gases, harmonics can be generated both parallel and perpendicular to the polarization vector of the driver. [23].
- **ISOLATED ATTOSECOND PULSES ARE POSSIBLE** One of the major success of gas phase HHG is the generation of attosecond pulses. One of the features of attosecond pulses from gas is the chirp which is a consequence of the re-collision model. Recently the HHG processes in solids have also been used to generate isolated attosecond pulses [28]. However unlike gases, these pulses were found to be chirp-free when driven by optical pulses. This result was only compatible with the intraband picture.
- **SYMMETRY PROPERTIES** High harmonic spectrum in solids is highly related to the symmetry properties of the crystal under consideration [16]. The crystals with inversion symmetry only emit odd harmonics while others may emit both even and odd harmonics, unlike gases where atoms have inherent inversion symmetry and generate only odd harmonics. Also, a strong dependence on the position of the atom inside the crystal structure was observed where harmonic emission is enhanced or suppressed when its classical trajectory connects or misses the nearest neighbor atom, respectively [61].

## 2.4 Summary

This chapter discussed the current understanding of HHG in solids, where an intuitive picture such as Bloch oscillations only involving single band and semiconductor Bloch equations involving multiple bands to explain the HHG process in solids were outlined. These pictures were used to probe the band dispersion of the solid [19, 18]. However, probing more fundamental properties of solid such as its valence potential requires associating HHG process to the crystal potential. With this motivation, we develop a picture of high harmonic generation due to scattering of electrons in the periodic potential of solids,

without invoking band picture and in subsequent chapters attempt to understand how this picture can predict features such as cutoff energy law and intensity dependence.

# Chapter 3

## Foundations of optical picoscopy

### 3.1 Introduction to high frequency approximation

In the physics of stimulated coherent bremsstrahlung [81], electron dynamics in the presence of a laser field has been long treated using a kinematic description. In this picture, the kinetic energy of the electron is much higher than the energy of crystal potential which it experiences. Hence, the crystal potential force can only introduce a weak perturbation to the motion of an electron. As a result, the velocity of the particle traversing the crystal is nearly identical to the particle which is free from forces of the periodic potential.

In the band picture of solids, the laser-driven electron cannot be treated as a free particle. Here, the motion of an electron in a periodic potential is very different from its motion in a vacuum. Hence, the concept of an effective mass is essential. However, on a more fundamental level, one can understand the laser-driven motion of an electron in a periodic potential differently. It is possible to drive an electron in a potential as a nearly-free particle if the external force is able to suppress the binding force the electron experiences while traversing the crystal potential. It has been long understood that this is possible when the frequency of the driving laser is much higher than the inherent frequencies of the binding potential. In strong field atomic physics, high-frequency driving leads to important phenomenon such as atomic stabilization [82]. Here we explore if similar concepts are valid in solids.

### 3.2 Understanding valence potential

To understand whether the high frequency regime and the ideas related to it can be extended to solids, we must first understand the properties of the potential experienced by a valence electron in a real crystal. In solids, periodic arrangement of the atomic potential creates the crystal potential. Fig. 3.1 depicts the formation of crystal potential by superimposition of various atomic potentials separated from each other at fixed distance  $d$  which is defined as the lattice constant. The strength of the total potential experienced by a valence electron in a crystalline solid is given as  $U_{tot}(x) = U_0 + U_{in}$  where  $U_0$  is a

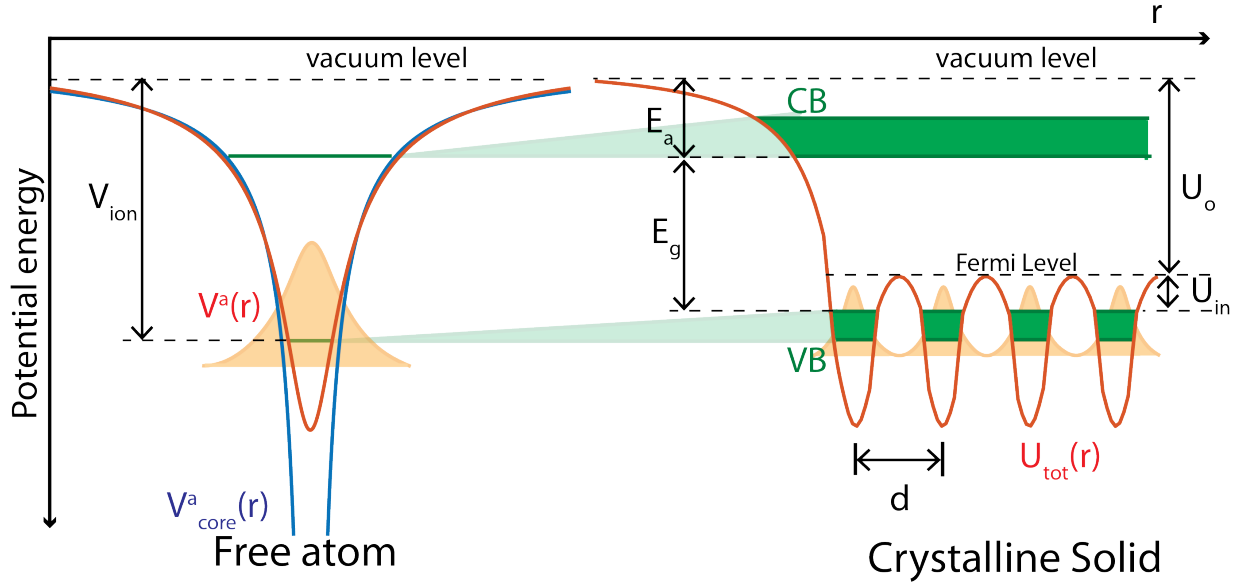


Figure 3.1: Left: The core potential ( $V_{core}^a(r)$ ) and the valence potential  $V^a(r)$  of an atom along with the energy levels.  $V_{ion}$  is the ionization potential of the atoms. The electronic wavefunction of the ground state of the atom is represented by the yellow area. Right: Illustrates the potential of solid formed by superimposing the atomic potentials at regular distance  $d$ . The discrete energy levels of atoms are replaced by valence band (VB) and conduction band (CB), in solids. The total potential experienced by a valence electron ( $U_{tot}$ ) is the sum of constant offset  $U_0$  and the inner potential whose amplitude is given by  $U_{in}$ . The value of  $U_{in}$  is given by the difference between the top of the valence band and Fermi level.  $E_a$  is the electron affinity and  $E_g$  is the band gap.

constant offset generated due to the summation of individual atomic potentials and  $U_{in}$  is the amplitude of the inner potential. Here,  $U_0$  is spatially invariant and  $U_{in}$  is associated with the local electron density near the Fermi level. The amplitude of the inner potential ( $U_{in}$ ) is given by the difference in the energy of top of the valence band (VB) and the Fermi level (Fig. 3.1).  $U_0$  is constant and therefore does not yield any force on the electrons. However, the inner potential follows the spatial variation of the potential of the crystal and plays an important role in determining the dynamics of the electron driven by the intense laser field.

One of the systems under study in this work is  $MgF_2$ . A one dimensional slice of valence potential of  $MgF_2$  along F-Mg-F molecular axis calculated from the density functional theory(DFT) is shown in 3.2. The inner potential ( $U_{in}$ ) of  $MgF_2$  is calculated to be 1eV. Hence, the high frequency regime for this system, where valence electron can follow the light field as a nearly free particle, is achieved when  $\hbar\omega > U_{in} = 1eV$ .

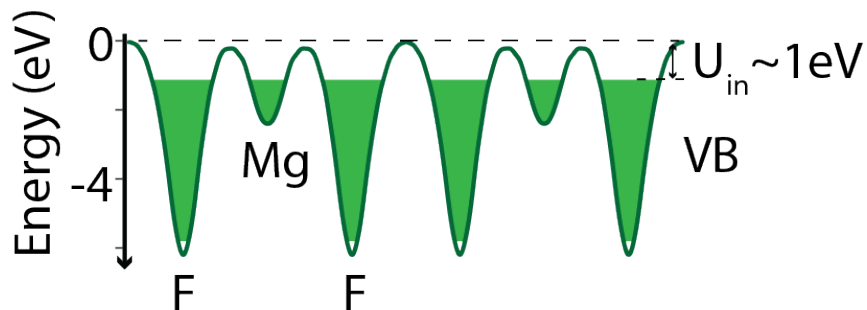


Figure 3.2: Figures illustrates the valence potential and the valence band energy of  $\text{MgF}_2$  calculated using density functional theory. The inner potential ( $U_{in}$ ) of  $\text{MgF}_2$  is 1eV. Hence, the high frequency regime is achieved for driving pulses having carrier photon energy greater than 1eV ( $\hbar\omega > 1\text{eV}$ )

### 3.3 High frequency approximation

Now, we demonstrate the validity of our approximation using classical, quantum mechanical and finally using time dependent density functional theory. In addition, we explore the frequency regimes in which it is valid.

#### 3.3.1 Classical perspective

Using the classical equations of motion, we try to discern the difference between the motion of an electron driven by pulses with photon energies lower and higher than the inner potential of the solid under investigation. Fig. 3.3a depicts a periodic potential of a solid (blue curve) modeled as a Mathieu potential which is defined as  $V(x) = U_{in} \cos(kx)$ , where  $U_{in}$  is the amplitude of the potential and  $k$  is the wave vector. The dynamics of an electron in the periodic potential driven by the laser field can be understood to resemble a damped driven oscillator and the same equations can be used for the numerical analysis. Fig. 3.3b,c compare the motion of a laser-driven electron with and without the periodic potential for the two regimes. In Fig. 3.3b the electron is driven by laser field with carrier photon energy 0.4 eV ( $\hbar\omega < U_{in}$ ). Positions of the bound and the free electrons (Fig. 3.3b), are recorded at three different instances to map the trajectory of the electrons. It shows that in the low frequency regime the electron is bound to the potential and its trajectory deviates from the trajectory of the free electron. However, in Fig. 3.3c, where electron is driven by the laser field with a carrier photon energy of 2eV ( $\hbar\omega > U_{in}$ ), the trajectory of the bound electrons follows that of the free electron.

Fig. 3.3d,e compare the velocities of a free and a bound electron in the high and the low frequency regimes, respectively. In the low frequency regime, where the photon energy is lower than the inner potential ( $\hbar\omega < U_{in}$ ), the velocity of the electron in the periodic potential (red line) is significantly lower compared to the velocity of the free electron. However for the high frequency regime, ( $\hbar\omega > U_{in}$ ), the velocity of the electron experiencing the periodic potential follows the velocity of the free particle very closely,

supporting the fact that for fields with photon energy higher than the inner potential, a valence electron bound to the crystal potential can be treated as a nearly free particle. In the high frequency regime, the potential barrier is sufficiently suppressed to make way for the electrons to move as nearly free particles.

### 3.3.2 Quantum mechanical perspective

The high frequency approximation was also examined using the single-electron quantum mechanical simulations. The time dependent schrödinger equation (TDSE) was solved for a Hamiltonian containing a periodic potential and a time dependent electric field.

$$i\hbar\frac{\partial\Psi(\mathbf{r},t)}{\partial t} = \mathbf{H}\Psi(\mathbf{r},t); |\Psi(\mathbf{r},\Delta t)\rangle = e^{-\frac{iH\Delta t}{\hbar}}|\Psi(\mathbf{r},0)\rangle \quad (3.1)$$

For most Hamiltonians, an analytical solution of the TDSE is not viable. Therefore, we resort to numerical methods for solving it. Time propagation is solved using the split operator method. Again, ground state electron wavefunction (yellow) Fig. 3.3a is driven by the laser field on a Mathieu potential and the velocities were obtained by applying momentum operator. Fig. 3.3d,e show the velocities of the electron obtained from solving the TDSE. The same conclusion, that velocity of an electron bound to crystal in the high frequency regime follows the velocity profile of a free electron, can be inferred.

### 3.3.3 Time dependent density functional theory

#### Method

The three dimensional, time dependent density functional theory (TDDFT) simulations, performed by our collaborators, Shiqi Hu and Dr. Sheng Meng at The Institute of Physics, Chinese Academy of Sciences, are consistent with the conclusions obtained from the classical and the quantum mechanical one dimensional calculations. TDDFT calculations were performed for the rutile-type  $\text{MgF}_2$  unit cell ( $P4_2/mnm$ ). The unit cell contains 2 Magnesium and 4 Fluorine atoms with the lattice constants  $a = b = 4.628 \text{ \AA}$  and  $c = 3.051 \text{ \AA}$  [83]. The density functional theory (DFT) calculations were performed using the Quantum ESPRESSO package (QE) to obtain the ground state properties, using a norm-conserving (NC) pseudopotential in conjunction with the Perdew BurkeErnzerhof (PBE) functional [84] and plane-wave (PW) basis set with energy cutoff at 400 eV. The energy convergence threshold for self-consistent calculations was set at  $10^{-6}$  (a.u). In the ground state calculations,  $12 \times 12 \times 24$  k-points were used for sampling and a direct band gap of 7 eV was obtained which was 3.8 eV lower than the experimental value. The excited-state simulations were performed within the real-time time dependent density functional theory (TDDFT) formalism using the time-dependent Kohn-Sham equation (TDKS)  $i\hbar\frac{\partial\psi}{\partial t} = \hat{H}\psi$  to simulate the excitation process [85]. Higher harmonic spectra were obtained by Fourier transforming the current  $\text{HHG}(\omega) \propto \omega^2|\text{FT}[I(t)]|^2$ .

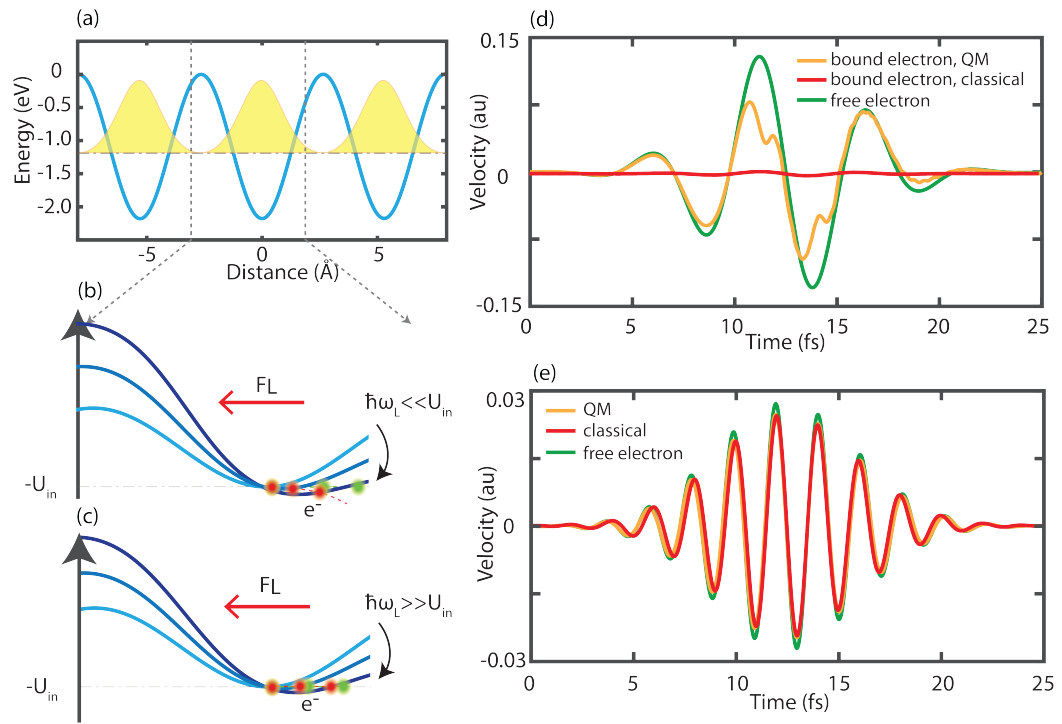


Figure 3.3: (a) Mathieu potential (blue) and the ground state (yellow) wavefunction of the potential. (b),(c) The position of crystal/bound electron (red dot) and free electron (green dot) driven by pulse with career photon energy 0.4 eV (b) and for 2 eV (c) on potential (blue lines) at 3 instances of laser field. A trajectory connecting these three positions is marked by dashed line. For  $\hbar\omega < U_{in}$  trajectory of crystal electron does not follow free electron(b) contrary to the case where crystal electron follows free electron(c). (d)(e) Comparison of the velocity of a crystal electron (green) to that of a free electron using quantum mechanical calculations (orange) and classical calculations (red), in low frequency regime  $\hbar\omega < U_{in}$  (d) and the high frequency regime  $\hbar\omega > U_{in}$  (e). In the high frequency regime velocity of crystal electron follows the velocity of free electron

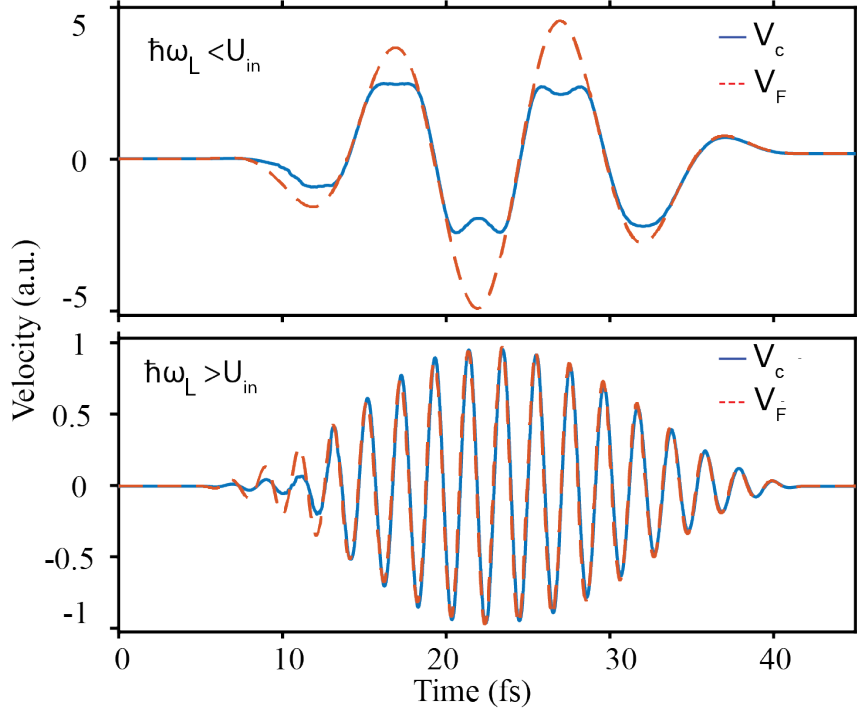


Figure 3.4: Velocity  $V_c$  of particle in  $\text{MgF}_2$  crystal compared to velocity of free particle ( $V_F$ ) for the low frequency ( $\hbar\omega < U_{in}$ ) and the high frequency ( $\hbar\omega > U_{in}$ ) regime. In the high frequency regime particle experiencing  $\text{MgF}_2$  potential force, behaves as a nearly free particle.

### Analysis

Fig. 3.4 compares the velocity of a free electron to the velocity of an electron experiencing the periodic potential of  $\text{MgF}_2$ , along the F-Mg-F molecular axis for  $\hbar\omega < U_{in}$  and  $\hbar\omega > U_{in}$  conditions extracted from TDDFT. When the electron is driven by a laser pulse with a field strength  $0.5\text{V}/\text{\AA}$  and a carrier photon energy  $0.4\text{ eV}$  in the low frequency regime ( $\hbar\omega < U_{in}$ ), the velocity of electron experiencing the potential force is much lower than that of a free electron. However, when the electron is driven by the same laser field strength but a higher carrier photon energy ( $2\text{ eV}$ ) in the high frequency regime  $\hbar\omega > U_{in}$  the velocity of the electron experiencing potential force follows closely the velocity profile of a free electron as suggested by the classical and the quantum mechanical analyses. Hence the TDDFT calculations provide conclusive evidence for the validity of our approximation in the high frequency regime.

To infer the range of frequencies where an electron behaves as a nearly-free particle in the  $\text{MgF}_2$  crystal, the ratio of the maximum velocity of the free particle and the particle experiencing the crystal potential was calculated. Fig. 3.5 highlights the onset of the high frequency regime where  $\hbar\omega > U_{in}$  ( $\sim 1\text{eV}$ ) and show that the free electron improves asymptotically for the higher frequencies.

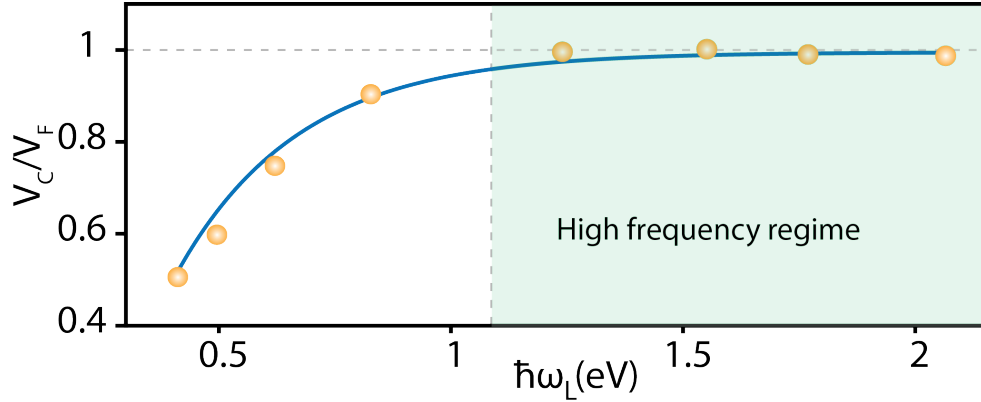


Figure 3.5: Ratio of velocity of free electron to that of crystal electron at various driving carrier photon energy. The ratio tends towards unity in the high frequency regime ( $\hbar\omega > U_{in}$ )

### 3.4 Semiclassical scattering of high harmonic generation in solids

The above study demonstrates that a laser-driven electron motion in the high frequency regime affords a semiclassical analysis, as the potential barrier is largely suppressed in this regime and the periodic potential acts as a perturbation to the free electron motion. The theoretical description of high harmonic generation in terms of an electron motion driven by a intense laser field in a periodic lattice of solids is explained both classically [86, 87] and quantum mechanically [88, 89] in previous works. In these earlier works, HHG from solids under very strong laser fields were studied, where electrons move over many lattice periods and scan its periodic structure. An extremely intense laser field exceeding the potential by several orders allows the electron motion to be nearly free. However, such models require very intense fields of the order of  $10^{17}$  W/cm<sup>2</sup>. Hence, they could not become experimentally alluring owing to the low damage threshold of most of the solids. Nevertheless, as shown in the previous section, a periodic potential can be treated as a perturbation in the high frequency regime too. This regime does not require relativistic fields to apply this approximation. Here, we will adopt some important features from the above works to establish a basis for the optical picoscopy.

Briefly, we are interested in describing the process of high harmonic generation driven by a laser field  $E(t)$  in a periodic potential  $V(r) = \sum_{\mathbf{k}} u_{\mathbf{k}} e^{-i\mathbf{k}\cdot r}$  where,  $u_{\mathbf{k}} = \Re u_{\mathbf{k}} + i\Im u_{\mathbf{k}}$ , is a complex number and  $\Re u_{\mathbf{k}}$  and  $\Im u_{\mathbf{k}}$  is the real and the imaginary part of the Fourier coefficients of the potential, respectively.

### High Harmonic Generation

High harmonic generation can be obtained from the Fourier transform of the time-dependent acceleration

$$I^{(n)} \propto \left| \int_0^\infty e^{-in\omega t} \ddot{\vec{d}}(t) dt \right|^2 \quad (3.2)$$

where time-dependent dipole acceleration  $\vec{d}(t)$  is conventionally defined as

$$\vec{d}(t) = \langle \Psi(r, t) | er | \Psi(r, t) \rangle \quad (3.3)$$

### Dipole in the laser field

In the zeroth order approximation the potential can be neglected then the wave function is superposition of the Volkov states.

$$\Psi(\mathbf{x}, t) = \int c(\mathbf{k}(t)) \Phi_{\mathbf{k}}(\mathbf{x}, t) d^3k = \int c(\mathbf{k}(t)) e^{i\mathbf{k}\mathbf{x}} e^{i\phi(\mathbf{k}, t)} d^3k \quad (3.4)$$

Here the dipole approximation is taken such that the light field only depends on time. The time-dependent phase is given by

$$\phi(\mathbf{k}, t) = \frac{1}{2} \int_0^t (\mathbf{k} - \mathbf{E}_0 \cos(\omega^2 \tau))^2 d\tau. \quad (3.5)$$

The dipole in the presence of laser field can now be obtained as:

$$\langle \Phi_{\mathbf{k}}(t) | \hat{\mathbf{x}} | \Phi_{\mathbf{k}'}(t) \rangle = \quad (3.6)$$

$$= \int e^{i(\mathbf{k}-\mathbf{k}')\mathbf{x}} e^{i\phi(\mathbf{k}, t) - i\phi(\mathbf{k}', t)} d^3x = \quad (3.7)$$

$$= e^{i(\frac{1}{2}(\mathbf{k}^2 - \mathbf{k}'^2)t - (\mathbf{k} - \mathbf{k}') \frac{\mathbf{E}_0}{\omega^2} \sin(\omega t))} \int \mathbf{x} e^{i(\mathbf{k}-\mathbf{k}')\mathbf{x}} d^3x = \quad (3.8)$$

$$= e^{i(\frac{1}{2}(\mathbf{k}^2 - \mathbf{k}'^2)t - (\mathbf{k} - \mathbf{k}') \frac{\mathbf{E}_0}{\omega^2} \sin(\omega t))} (-i(2\pi)^3) \delta'(\mathbf{k} - \mathbf{k}') \quad (3.9)$$

and thus the dipole is given by

$$\langle \Psi_t | \hat{\mathbf{x}} | \Psi_t \rangle = \quad (3.10)$$

$$= \int c_{\mathbf{k}} c_{\mathbf{k}'}^* \langle \Phi_{\mathbf{k}}(t) | \hat{\mathbf{x}} | \Phi_{\mathbf{k}'}(t) \rangle d^3 k d^3 k' = \quad (3.11)$$

$$= \int c_{\mathbf{k}} c_{\mathbf{k}'}^* e^{i(\frac{1}{2}(\mathbf{k}^2 - \mathbf{k}'^2)t - (\mathbf{k} - \mathbf{k}') \frac{\mathbf{E}_0}{\omega^2} \sin(\omega t))} (-i(2\pi)^3) \delta'(\mathbf{k} - \mathbf{k}') d^3 k d^3 k' = \quad (3.12)$$

$$\text{substitute } \mathbf{a} = \mathbf{k} - \mathbf{k}', \quad \mathbf{b} = \mathbf{k} + \mathbf{k}'. \text{ Jacobian determinant is } \frac{1}{8} \quad (3.13)$$

$$\propto \int c_{(\mathbf{a}+\mathbf{b})/2} c_{(\mathbf{b}-\mathbf{a})/2}^* e^{i(\mathbf{a}\mathbf{b}t/4 - \mathbf{a} \frac{\mathbf{E}_0}{\omega^2} \sin(\omega t))} (-i) \delta'(\mathbf{a}) d^3 a d^3 b = \quad (3.14)$$

$$= -i \int \nabla_{\mathbf{a}} \Big|_{\mathbf{a}=0} \left\{ c_{(\mathbf{a}+\mathbf{b})/2} c_{(\mathbf{b}-\mathbf{a})/2}^* e^{i(\mathbf{a}\mathbf{b}t/4 - \mathbf{a} \frac{\mathbf{E}_0}{\omega^2} \sin(\omega t))} \right\} d^3 b = \quad (3.15)$$

$$= -i \int \left( c'_{\mathbf{b}/2} c_{\mathbf{b}/2}^* - c_{\mathbf{b}/2} c'_{\mathbf{b}/2} + c_{\mathbf{b}/2} c_{\mathbf{b}/2}^* i(\mathbf{b}t/4 - \frac{\mathbf{E}_0}{\omega^2} \sin(\omega t)) \right) d^3 b = \quad (3.16)$$

$$\propto \int \text{Im}(c_{\mathbf{k}} \nabla c_{\mathbf{k}}^*) d^3 k + t \int |c_{\mathbf{k}}|^2 \mathbf{k} d^3 k + \frac{\mathbf{E}_0}{\omega^2} \sin(\omega t). \quad (3.17)$$

The three terms have an obvious interpretation as

$$\langle \Psi_t | \hat{\mathbf{x}} | \Psi_t \rangle = \mathbf{x}_0 + t\mathbf{v}_0 + \frac{\mathbf{E}_0}{\omega^2} \sin(\omega t), \quad (3.18)$$

where  $\mathbf{x}_0$  and  $\mathbf{v}_0$  are, respectively, the expectation values of position and velocity in the initial electron wave packet at  $t = 0$ . The motion of electron wavepacket can be understood as the classical trajectory starting from the point of symmetry ( $\mathbf{x}_0$ ) and following the path defined by the laser field. As is in gas phase physics, it is safe to assume that the particle has no initial velocity.

$$\mathbf{d}(t) = \mathbf{x}_0 + \frac{\mathbf{E}_0}{\omega^2} \sin(\omega t) \quad (3.19)$$

### Crystal potential as perturbation

The dominant contribution to the emitted radiation is due to the quiver motion ( $\mathbf{d}(t)$ ) in the laser field which contributes only to the fundamental frequency. High harmonics are generated due to interaction with crystal potential whose dipole acceleration term ( $\ddot{\mathbf{d}}(t)$ ) is given as

$$\ddot{\mathbf{d}}(t) = \frac{e}{m} \nabla V(\mathbf{d}(t)) \quad (3.20)$$

Now, we proceed to write the periodic potential in terms of its Fourier coefficients. For inversion symmetric potentials the form of the potential can be further simplified and written as  $V(r) = \sum_{\mathbf{k}} u_{\mathbf{k}} \cos(\mathbf{k} \cdot \mathbf{r})$ . In this case, the dipole acceleration can be further

simplified to

$$\ddot{\mathbf{d}}(t) = \frac{e}{m} \nabla \sum_{\mathbf{k}} u_{\mathbf{k}} e^{-i\mathbf{k} \cdot \mathbf{d}(t)} \quad (3.21)$$

$$= -i\mathbf{k} \frac{e}{m} \sum_{\mathbf{k}} u_{\mathbf{k}} e^{-i\mathbf{k} \cdot (\mathbf{x}_0 + \frac{\mathbf{E}_0}{\omega^2} \sin(\omega t))} \quad (3.22)$$

$$(3.23)$$

without loss of generality we can choose our origin to be at a symmetry point  $x_0$ .

$$\ddot{\mathbf{d}}(t) = -i \frac{e}{m} \sum_{\mathbf{k}} \mathbf{k} u_{\mathbf{k}} e^{-i\mathbf{k} \cdot (\frac{\mathbf{E}_0}{\omega^2} \sin(\omega t))} \quad (3.24)$$

$$(3.25)$$

Splitting the equation into the real and the imaginary parts and using the Jacobi-Anger expansion  $\sin(z \sin \theta) = 2 \sum_{n=1}^{\infty} J_{2n-1}(z) \sin[(2n-1)\theta]$ ,  $\cos(z \sin \theta) = J_0(z) + 2 \sum_{n=1}^{\infty} J_{2n}(z) \cos[(2n)\theta]$ , the real part of the dipole acceleration can be decomposed into sum of two terms such as  $\ddot{\mathbf{d}}(t) = \ddot{\mathbf{d}}^{\text{odd}}(t) + \ddot{\mathbf{d}}^{\text{even}}(t)$ .

$$\ddot{\mathbf{d}}^{\text{odd}}(t) = \frac{e}{m} \sum_{\mathbf{k}} \mathbf{k} \Re u_{\mathbf{k}} \sum_N J_N \left( \mathbf{k} \cdot \frac{\mathbf{E}_0}{\omega^2} \right) \sin((2N-1)\omega t) \quad (3.26)$$

$$\ddot{\mathbf{d}}^{\text{even}}(t) = \frac{e}{m} \sum_{\mathbf{k}} \mathbf{k} \Im u_{\mathbf{k}} \sum_N J_N \left( \mathbf{k} \cdot \frac{\mathbf{E}_0}{\omega^2} \right) \cos(2N\omega t) \quad (3.27)$$

$$(3.28)$$

where,  $\ddot{\mathbf{d}}^{\text{odd}}(t)$  is termed as odd dipole acceleration and  $\ddot{\mathbf{d}}^{\text{even}}(t)$  is termed as even dipole acceleration. Field of emitted harmonics can be obtained by Fourier transforming the obtained dipole accelerations as:

$$\mathbf{E}_{2N-1}^{\text{odd}}(t) = \frac{e}{m} \sum_{\mathbf{k}} \mathbf{k} \Re u_{\mathbf{k}} J_{2N-1} \left( \mathbf{k} \cdot \frac{\mathbf{E}_0}{\omega^2} \right) \quad (3.29)$$

$$\mathbf{E}_{2N}^{\text{even}}(t) = \frac{e}{m} \sum_{\mathbf{k}} \mathbf{k} \Im u_{\mathbf{k}} J_{2N} \left( \mathbf{k} \cdot \frac{\mathbf{E}_0}{\omega^2} \right) \quad (3.30)$$

$$(3.31)$$

The intensity of the emitted harmonics in the direction of laser polarization is then given as:

$$I_{2N-1}^{odd}(t) = \left| \frac{e}{m} \sum_{\mathbf{k}} (\mathbf{k} \cdot \mathbf{e}_0) \Re u_{\mathbf{k}} J_{2N-1} \left( \mathbf{k} \cdot \frac{\mathbf{E}_0}{\omega^2} \right) \right|^2 \quad (3.32)$$

$$I_{2N}^{even}(t) = \left| \frac{e}{m} \sum_{\mathbf{k}} (\mathbf{k} \cdot \mathbf{e}_0) \Im u_{\mathbf{k}} J_{2N} \left( \mathbf{k} \cdot \frac{\mathbf{E}_0}{\omega^2} \right) \right|^2 \quad (3.33)$$

$$(3.34)$$

where  $I_N$  is the intensity of the  $N^{th}$  harmonic in the direction of laser polarization,  $\mathbf{e}_0$  is the unit vector in the direction of laser polarization,  $E_0$  is the electric field strength and  $\omega$  is the laser frequency.

### 3.5 Cutoff law

For a given field strength ( $E_0$ ), laser frequency ( $\omega$ ) and highest significant reciprocal space vector ( $k_{max}$ ) of the potential, the cutoff harmonic is the value of  $N$  which maximizes the intensity equation Eq.3.32. The cutoff energy is then given as

$$\begin{aligned} N_{\text{cutoff}} &= k_{max} \frac{E_0}{\omega^2} \\ E_{\text{cutoff}} &= k_{max} \frac{E_0}{\omega} \end{aligned} \quad (3.35)$$

where  $\omega$  is the frequency of the input pulse. Compared to gases, where cutoff energy is directly proportional to the intensity of driving field, in solids the cutoff energy is experimentally observed to be proportional to the field strength.

The equation for the cutoff energy is analogous to the one obtained from the Smith Purcell effect. In this effect, electromagnetic radiation is generated when an electron beam moves over a periodic structure, such as a grating. The process is intuitively explained as the scattering of the Coulomb field of the electrons on the periodic grating structure. The frequency of the scattered radiation is given by the ratio of velocity of the electron to the grating periodicity  $\omega = \frac{2\pi v_e}{d} = k v_e$ . The cutoff energy of high harmonic radiation in solids can also be interpreted as the energy of the electron with velocity ( $v = E_0/\omega$ ) scattering on the smallest structure with the radius  $r_s$  ( $k_{max} = \frac{\pi}{r_s}$ ). Hence it can also be written as

$$E_{\text{cutoff}} = \frac{\pi}{r_s} \frac{E_0}{\omega} \quad (3.36)$$

The measurement of the cutoff energy of harmonic spectra from a crystalline solid can be used to obtain the valence electron radius of the smallest specimen inside the crystal. This equation hence provides direct insight into the crystal structure.

## 3.6 Tool box for picoscopy

The most significant equations are summarized here. In this thesis, only crystals with symmetric potentials are studied so the Fourier coefficients will be real numbers and will generate only odd harmonics. Hence only the equations for odd harmonics are summarized here.

### 3.6.1 Starting point is symmetry point

$$\langle \Psi_t | \hat{\mathbf{x}} | \Psi_t \rangle = \mathbf{x}_0 + t\mathbf{v}_0 + \frac{\mathbf{E}_0}{\omega^2} \sin(\omega t) \quad (3.37)$$

This equation suggests that the dynamics of the dipole acceleration term can be understood as a classical motion of electron starting from the expectation value of the initial position and following the vector potential of the laser field. The expectation value of the initial position ( $\mathbf{x}_0$ ) or ground state of the electron wave will be a symmetry point in the crystal. Hence, in a high frequency regime, time-dependent dipole acceleration can be obtained from the classical motion of electron starting from the symmetry point of the crystal.

### 3.6.2 Dipole related to solid structure

$$\ddot{\mathbf{d}}^{\text{odd}}(t) = \frac{e}{m} \sum_{\mathbf{k}} \mathbf{k} \mathfrak{R} u_{\mathbf{k}} \sum_N J_N \left( \mathbf{k} \cdot \frac{\mathbf{E}_0}{\omega^2} \right) \sin((2N-1)\omega t) \quad (3.38)$$

The dipole term  $\ddot{\mathbf{d}}^{\text{odd}}(t)$  is a vector, which implies that the electric field polarization of the radiated harmonics may deviate from the laser polarization ( $E_o$ ) as described in other works [90]. This deviation from laser polarization direction is due to the topology of the lattice on which electron accelerates. It also provides a direct link between the Fourier coefficients of the potential ( $u_{\mathbf{k}}$ ) which allows us to provide a description of harmonic emission in any kind of periodic material without invoking a band picture.

### 3.6.3 Intensity related to structure factors

$$I_N \propto \left| \frac{e}{m} \sum_{\mathbf{k}} (\mathbf{k} \cdot \mathbf{e}_0) u_{\mathbf{k}} J_N \left( \mathbf{k} \cdot \mathbf{e}_0 \frac{E_0}{\omega^2} \right) \right|^2 \quad (3.39)$$

The intensity of emitted harmonic is directly linked to the Fourier coefficients and provides the way for optical picoscope. Inverting this equation provides direct access to the Fourier coefficients ( $u_{\mathbf{k}}$ ) of the material. The methods to extract Fourier coefficients of the potential using this equation is detailed in chapter 5.

### 3.6.4 Cutoff links to the smallest specimen in the valence potential

$$\boxed{E_{cutoff} = k_{max} \frac{E_o}{\omega}} \quad (3.40)$$

$$\boxed{r_s = \frac{2\pi}{E_{cutoff}} \frac{E_o}{\omega}} \quad (3.41)$$

The cutoff energy of the material depends on the smallest specimen it contains. This equation provides direct access to the ionic/covalent radii of the smallest specimen in the system. Chapter 7 presents the experimentally observed cutoff energy and measured valence electron radius of the smallest specimen in various crystalline materials.



# Chapter 4

## Analogies and differences with crystallography

To associate with crystallography, we write the equations derived in chapter 3, in terms of the crystallographic notation. First, we review the following important equation in crystallography, describing the intensity of the diffracted X-rays.

$$I_{hkl} \propto |F_{hkl}|^2 \quad (4.1)$$

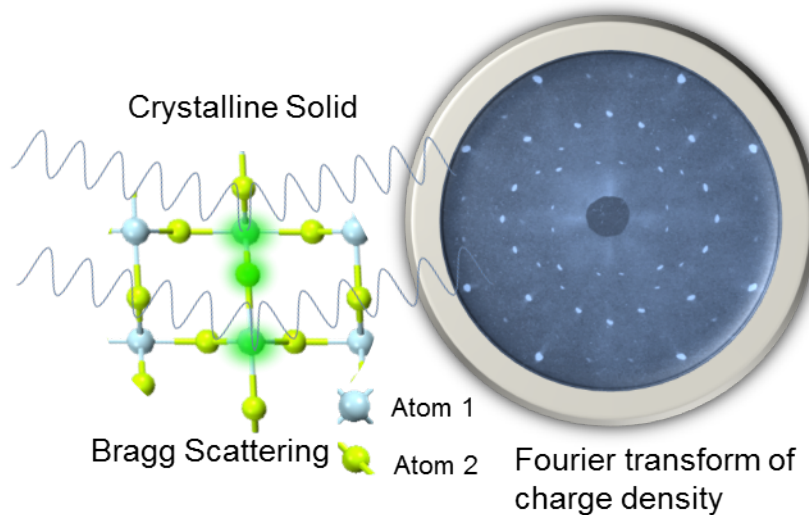


Figure 4.1: Schematic of X-ray diffraction from crystalline solids.

Here  $F_{hkl}$  are known as the structure factors of the crystal, with  $hkl$  being the indices for vectors in reciprocal space. The amplitude of the structure factor depends on the electron density as follows

$$F_{hkl} = \int_{V_{cell}} \rho_{XYZ} e^{-i2\pi(hX+KY+lZ)} dV \quad (4.2)$$

Here  $\rho$  denotes electron density and  $X, Y, Z$  are real space coordinates.

The equation for intensity of emitted harmonics from solids can also be written in terms of crystallographic notations as:

$$I_N(\mathbf{E}_o, \omega_L) \propto \left| \sum_{\mathbf{k}} (\mathbf{k} \cdot \mathbf{e}_o) u_k J_N(\mathbf{k} \cdot \mathbf{e}_o \frac{E_o}{\omega^2}) \right|^2 \quad (4.3)$$

where  $\mathbf{e}_o = \frac{\mathbf{E}_o}{|E_o|} = X\hat{i} + Y\hat{j} + Z\hat{k}$  is the unit vector in the direction of laser polarization and  $\mathbf{k} = \frac{2\pi}{d}(h\hat{i} + k\hat{j} + l\hat{k})$  is the reciprocal space wave vector. The intensity of the  $N$ th harmonic can then be expressed as,

$$I_N(E_o, \omega_l) \propto \left| \sum_{hkl} (hX + kY + lZ) u_{hkl} J_N \left( \frac{2\pi}{d} (hX + kY + lZ) \frac{E_o}{\omega_L^2} \right) \right|^2 \quad (4.4)$$

Equations Eq.4.1 and Eq.4.4 are very similar in notation except in equation Eq.4.4 the Fourier coefficients ( $u_{hkl}$ ) are besselized and summed over to obtain the intensity of  $N^{th}$  order harmonic. Here “besselized” means that the amplitude of the coefficients is multiplied by a Bessel function, which is a function of laser field strength and frequency.

## 4.1 Amplitude of Fourier coefficients

In diffraction, the amplitude of Fourier coefficients of the electron density ( $F_{hkl}$ ) is directly related to the amplitude of individual order of the diffraction pattern ( $I_{hkl}$ ) Eq.4.1. Similarly, in HHG in solids, the intensity of  $N^{th}$  harmonic ( $I_N$ ) for a given laser field with strength  $E_0$  and laser frequency  $\omega$ , depends on the Fourier coefficients of potential ( $u_k$ ) and the  $N^{th}$  order Bessel function ( $J_N(k)$ ) Eq.3.39. Here, in contrast to diffraction, a single intensity contains the contribution of all the Fourier coefficients ( $u_k$ ) of the potential. However, only a few Fourier coefficients contribute significantly to the intensity of particular laser harmonic. The following two sections explain the selectivity of laser harmonic to the Fourier coefficients.

The intensity ( $I_N$ ) of  $N^{th}$  harmonic is directly proportional to the product of  $N^{th}$  order Bessel function  $J_N(k)$  and  $u_k$ . Hence, the intensity will maximize when each one of them maximizes. For the sake of simplicity, if we assume that all Fourier coefficients are one then the intensity maximizes when the Bessel function maximizes. To understand the behaviour of Bessel function, we describe its behaviour with varying harmonic order ( $N$ ). For a given driving field with strength ( $E_0$ ) and frequency ( $\omega$ ), the Bessel function ( $J_N(k \frac{E_0}{\omega^2})$ ) as a function of the reciprocal vector ( $k$ ) acts like a weighing factor for individual Fourier coefficients. In other words, it acts as a bandpass filter for the Fourier coefficients by enhancing only a few of them and suppressing the rest. Fig. 4.2 shows  $3^{rd}$  to  $13^{th}$  order Bessel functions, terminated at its first root, as a function of reciprocal space vector ( $k$ ). The blue stems depict the position of Fourier coefficients with each coefficient having the same amplitude. We observe that the lower (higher) order Bessel functions are sensitive

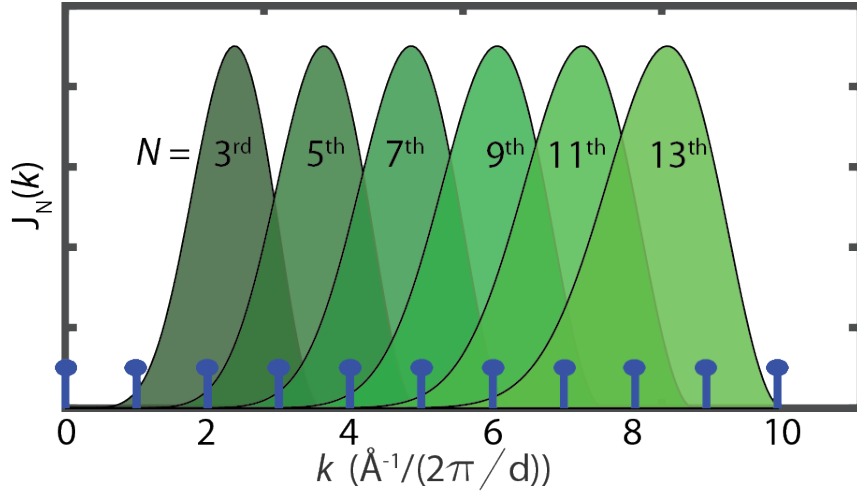


Figure 4.2: Bessel functions  $J_N(\frac{k \cdot E_o}{\omega^2})$  versus reciprocal lattice vector  $k$  plotted for order  $N = 3, 5, 7, 9, 11, 13$ , ( $3^{rd}$  to  $13^{th}$  laser harmonic) for photon energy  $\hbar\omega = 2.1\text{eV}$  and  $E=0.75\text{V}/\text{\AA}$ . Blue stem are hypothetical Fourier coefficients ( $u_k$ ) spaced at regular interval  $(2\pi/d)$ . Lower order( $N$ ) Bessel function peaks at low spatial frequency( $u_k$ ) and vice versa.

to lower(higher) Fourier coefficients. More specifically, for a pulse with field strength  $0.75\text{V}/\text{\AA}$  and centered at  $585\text{nm}$  ( $2.1\text{eV}$ ), the  $13^{\text{th}}$  harmonic has significant value at  $6^{\text{th}}$  to  $10^{\text{th}}$  Fourier coefficients and  $3^{\text{rd}}$  harmonic maximizes at  $1^{\text{st}}$  to  $3^{\text{rd}}$  Fourier coefficients. Intuitively, this means that lower harmonics are generated by the coarse features of the potential and higher harmonics are generated from the sharper features inside the potential.

Now, we proceed to understand the behaviour of the Bessel function for varying field strength ( $E_o$ ) for a given of harmonic order ( $N$ ) and frequency  $\omega$ . Fig. 4.3 shows sensitivity of  $5^{\text{th}}$  order Bessel function ( $5^{\text{th}}$  harmonic) over reciprocal space vector ( $\mathbf{k}$ ) at 5 different field strength. We observe that Bessel function at higher(lower) field strengths peaks at lower(higher) order Fourier coefficients. Importantly, by observing the emitted intensity over a broad range of driving fields, sensitivity to all the Fourier coefficients can be achieved using only a single laser harmonic. However, damage of crystalline material at very high field strength constraints the range of driving field strengths for which emitted harmonics can be observed.

In conclusion, to measure all Fourier coefficients with significant precision, one needs to measure the emitted intensity till the highest field strength sustained by the sample so that lower spatial frequencies can be properly reconstructed, and take the highest number of laser harmonics possible so that higher Fourier coefficients are obtained with significant precision.

The above analysis suggests that measuring the emitted intensity for all observed harmonics at various driving field strengths can provide information about the Fourier coefficients of the periodic potential.

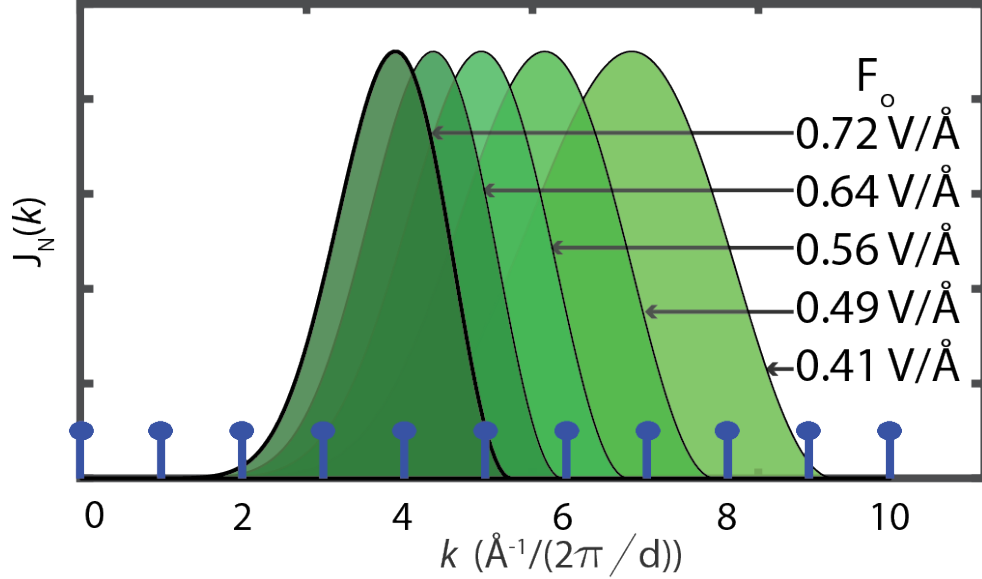


Figure 4.3: Bessel functions  $J_N(\frac{k \cdot E}{\omega^2})$  versus reciprocal lattice vector  $k$  plotted for order  $N=5$  ( $5^{\text{th}}$  laser harmonic) for photon energy  $\hbar\omega = 2.1\text{eV}$  and  $E=0.72, 0.64, 0.56, 0.49, 0.41$   $\text{V}/\text{\AA}$ . Blue stem are hypothetical Fourier coefficients ( $u_k$ ) spaced at regular interval ( $2\pi/d$ ). Bessel function at higher field strength peaks at low spatial frequency ( $u_k$ ) and vice versa.

## 4.2 Phase of Fourier coefficients

Measuring the diffraction intensity is at the heart of crystallography. Unfortunately, the phase information is lost as it only contains the absolute value of  $F_{hkl}$ .

In the technique presented in this thesis, even though we still measure the intensity of emitted harmonics, the phase information is still preserved. The sum over all the contributing coefficients along with their respective phases before taking the modulus square preserves the phase information, which is manifested in the cross terms. In this thesis, only centrosymmetric systems are analyzed. In such systems, the phase problem is reduced to a sign ( $\pm$ ) problem.

Fig. 4.4 presents simulation to understand how the information of phase (sign) of Fourier coefficients is manifested in the intensity dependence of the harmonics. As a reference calculation we first take the periodic potential generated using single Fourier coefficient Fig. 4.4a. The harmonic spectra obtained by driving electron on this potential and the intensity scaling of the  $7^{\text{th}}$  harmonic is shown in Fig. 4.4b,c. Note, the cutoff energy from this potential (14 eV) and the build-up of the intensity scaling of the  $7^{\text{th}}$  harmonic.

When another Fourier coefficient is added with an opposite phase (d) or the same phase (g), the harmonic spectra and the intensity yield of  $7^{\text{th}}$  harmonic changes Fig. 4.4. In case of opposite phase, the build-up of intensity scaling of the  $7^{\text{th}}$  harmonic (f) changes significantly from the reference (c). Here, the slope of the build-up is less aggressive

compared to the reference. However, when both the Fourier coefficients of the potential are of the same phase, the slope of intensity scaling of  $7^{th}$  harmonic is more aggressive than the reference (c).

In conclusion, comparison of intensity dependence between the two cases suggests that intensity yield of high harmonics contains not only the information of the amplitude but also of the phase of the individual Fourier coefficient of valence potential of a crystal.

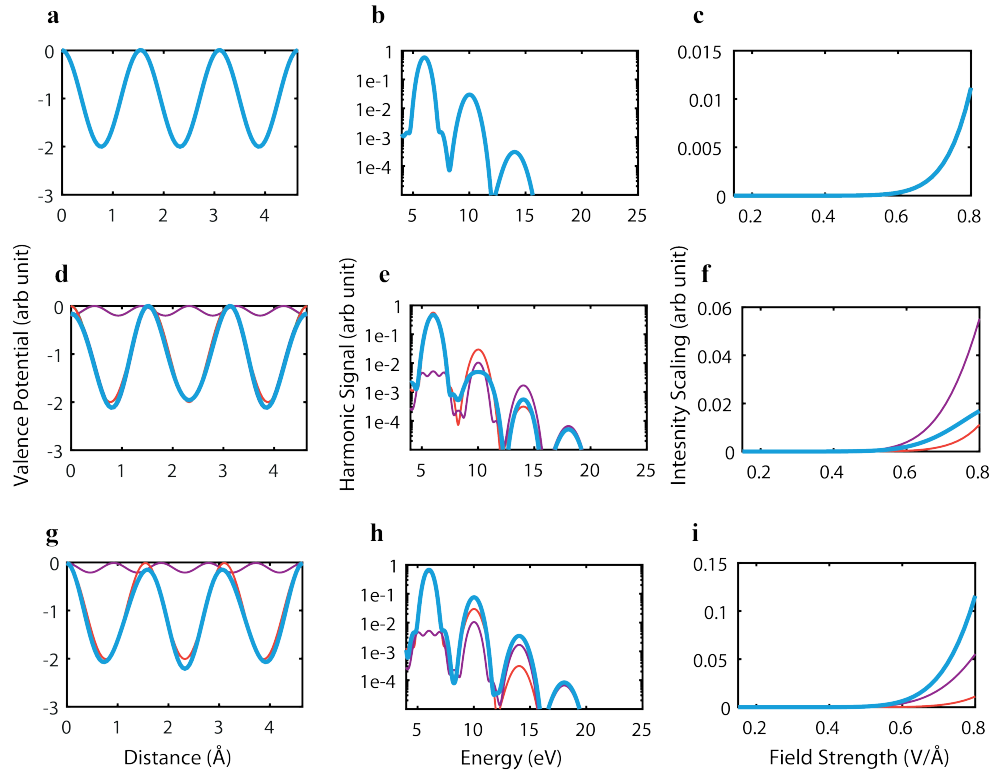


Figure 4.4: Periodic Potential (a) generated using single Fourier coefficient, emits harmonic signal (b) of laser pulse centered at 2eV. The intensity scaling of 7<sup>th</sup> harmonic centered at 14 eV is shown in (c). Potential generated using two Fourier coefficients of opposite phase, harmonic spectra emitted from it and intensity scaling of the 7<sup>th</sup> harmonic are shown in blue in (d)(e)(f) respectively. Potential of individual coefficients their respective harmonic spectra and the intensity scaling is shown in red and magenta in (d)(e)(f) respectively. (g)(h)(i) show the same for the potential generated from the coefficients having the same phase. The slope of intensity yield of the 7<sup>th</sup> harmonic from total potential is less aggressive when the phase of the coefficient is opposite. However, when the constituent Fourier coefficients of the potential have the same phase, the slope of the intensity yield of the 7<sup>th</sup> harmonic from total potential is more aggressive than the reference (c).

# Chapter 5

## Methods

### 5.1 Data analysis methods

Having understood how the amplitude and phase information is contained in the Eq.3.39, we now delve into the details of how experimentally obtained intensity yields of different harmonics can be analyzed to obtain the valence potential of a crystal.

#### 5.1.1 Analytical method

In this section, first the theoretical method for obtaining Fourier coefficients of the potential is presented.

$$I_N(\omega, E_o) = \left| \sum_{\mathbf{k}} \mathbf{k} \cdot \mathbf{e}_o u_{\mathbf{k}} J_N(\mathbf{k} \cdot \mathbf{e}_o \frac{E_o}{\omega^2}) \right|^2 \quad (5.1)$$

A closer scrutiny of the above equation reveals its resemblance with the discrete Hankel transform. The properties of the Hankel transform can hence be used to obtain the Fourier coefficients of the potential.

#### Hankel transform

The Hankel transform of order  $\nu$  of a function  $f(r)$  is given by  $F_\nu(k) = \int_0^\infty f(r) J_\nu(kr) r dr$ , where  $J_\nu$  is the Bessel function of the first kind of order  $\nu$  with  $\nu \geq -1/2$ . Similarly, the inverse Hankel transform is defined as:  $f(r) = \int_0^\infty F_\nu(k) J_\nu(kr) k dk$

#### High harmonic intensity dependence analogy with Hankel transform

Eq.5.1 can be rewritten in terms of the Hankel transform. First the discrete equation is written in continuous form. Let  $E_N(E_o) = \sqrt{I_N(\omega, E_o)}$  be the electric field of the emitted

harmonic for the incident field of strength  $E_o$ , then for a one dimensional potential

$$E_N(E_o) = \int_0^\infty u_k J_N(k \frac{E_o}{\omega^2}) k dk \quad (5.2)$$

The above equation is similar to the equation for the inverse Hankel transform. In principle, the Fourier coefficients of the potential  $u_k$  can now be obtained by just performing a Hankel transformation.

$$u_k = \int_0^\infty E_N(E_o) J_N(k \frac{E_o}{\omega^2}) E_o dE_o \quad (5.3)$$

If the intensity of emitted harmonics could be recorded for all possible field strengths then the above transformation can directly provide the values of  $u_k$  and hence we would be able to reconstruct the periodic potential analytically. However, in practice the sample is damaged after a high driving field strength thereby limiting the experimental capabilities to small range of field strengths. It is currently not feasible, even with some approximations, to perform the Hankel transform in the bounded range without passing through any of its roots. Hence, we have to resort to numerical methods to obtain the value of the Fourier coefficients.

### 5.1.2 Numerical method

The intensity yield versus driving field strength data can be fitted to obtain the Fourier coefficients ( $u_k$ ) along with their phases. We seek to minimize the objective function  $f$  over the independent variables  $u_k$ , i.e. we minimize  $\min_{\{u_k\}} f(\{u_k\})$ .  $f$  has the form  $f(\{u_k\}) = (\sum_N \sum_{E_o} I_N(E_o; \{u_k\}) - g_N(E_o))^2$  where  $I_N(E_o)$  and  $f(\{u_k\})$  denote the spectral intensity of the Nth harmonic (which depends on field strength  $E_o$ ) and the coefficients we would like to ascertain are  $f\{u_k\}$ ;  $g_N(E_o)$  is the data obtained from experiment, respectively. We next try to obtain the condition number to verify if the problem is well posed. The condition number of an algorithm quantifies how large the function deviates in response to a deviation of the initial conditions. We calculated the condition number of the algorithm for various  $u$ 's and all were less than one (typically on the order of  $10^{-1}$ ), indicating that our problem is well-conditioned. Now the experimentally obtained data can be fit to obtain the  $u_k$

In principle, all the significant Fourier coefficients  $u_k$  can be extracted from the intensity yield of a single harmonic. However, experiments put constraint on the field strength for which the signal can be recorded. Hence, we fit all the harmonics simultaneously. The fitting of the experimental intensity scaling data obtained when laser is polarized along the major crystal axes [100] and [110] is explained below. Fitting in other crystal direction is also done in a similar manner.

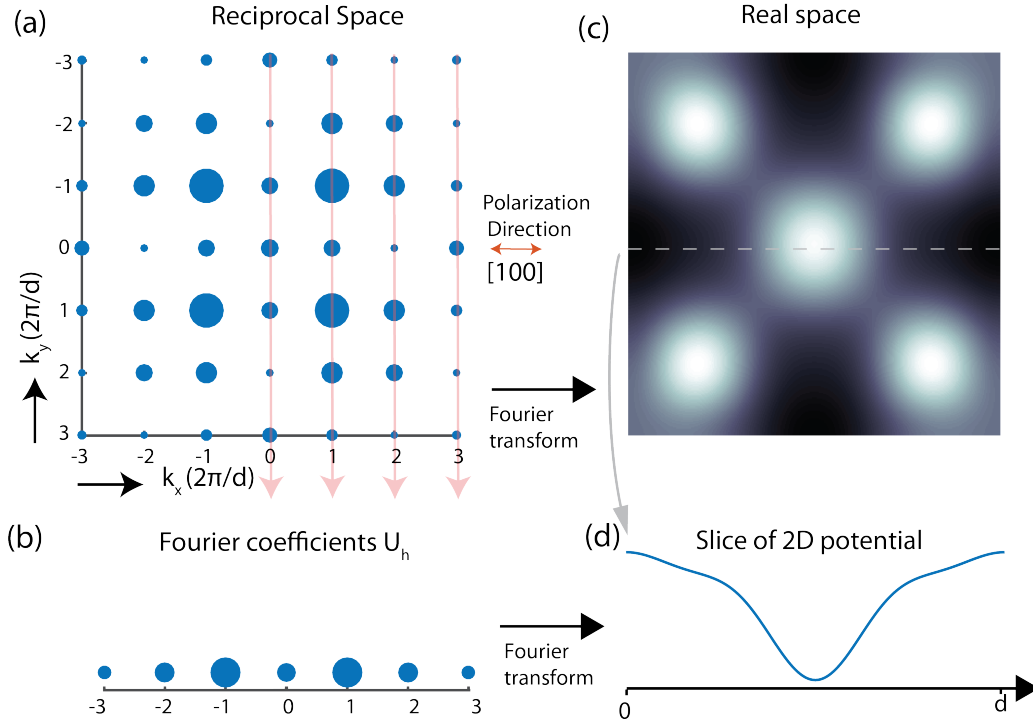


Figure 5.1: (a) Reciprocal space of a symmetric system. Amplitude of the Fourier coefficients is depicted by the size of the ball. Laser polarization is along [100] direction of the crystal. (b)  $U_h$  obtained by summing the Fourier coefficients along the direction perpendicular to laser polarization. (c) Symmetric potential obtained by Fourier transforming the coefficients in (a). (d) Slice of potential along [100] direction of crystal, which is also the Fourier transform of  $U_h$  according to projection-slice theorem.

### Fitting along the [100] direction of crystal

Eq.4.4 simplifies for the case when the laser is polarized along the direction of a symmetry axis. When the laser is polarized along [100] or  $\mathbf{e}_o = \hat{i}$ , then Eq.4.4 reduces to

$$I_N(E_o, \omega) \propto \left| \sum_h h J_N \left( h \frac{2\pi E_o}{d \omega^2} \right) U_h \right|^2 \quad (5.4)$$

where  $U_h = \sum_{kl} u_{hkl}$  is the sum of all coefficients on plane perpendicular to  $\mathbf{e}_o = \hat{i}$  at distance  $h$  from origin.

To understand this equation and its implications we take a hypothetical symmetric 2D potential. Fig. 5.1 shows the Fourier coefficients where the size of the dot shows the magnitude of the Fourier coefficient. The unit cell valence potential of this hypothetical system obtained by Fourier transformation of the coefficients is shown in Fig. 5.1(c).  $U_h = \sum_{kl} u_{hkl}$  is obtained by summing the coefficients along  $k_y$  axis and is shown in 5.1(b). These coefficients ' $U_h$ ' are also spaced with spacing  $(\frac{2\pi}{d})$ . The Fourier transform of these

coefficients is shown in Fig. 5.1(d)

The projection-slice theorem in 2D states that, the Fourier transform of the projection of a 2D function in 1D is equal to the 1D slice of 2D Fourier transform of that function through the origin of the axes of the Fourier transform. This means that line (d) which is a Fourier transform of the projection of 2D reciprocal space is a slice through the origin of the unit cell potential. The slice is shown as dotted line in the potential (c). Indeed, the fitted coefficients along [100] direction of the crystal provides direct access to the slice of the potential cut along this direction passing through the symmetry point (origin) of the potential.

### Fitting along the [110] direction

Similarly when laser is polarized along  $\mathbf{e}_o = \frac{1}{\sqrt{2}}(\hat{i} + \hat{j})$ , then Eq.4.4 reduces to

$$I_N(E_o, \omega) \propto \left| \sum_m \frac{m}{\sqrt{2}} J_N \left( \frac{2\pi m E_o}{d \sqrt{2} \omega^2} \right) U_m \right|^2 \quad (5.5)$$

where  $U_m = \sum_{h+k=m} u_{hkl}$  is sum of all coefficients on the plane perpendicular to  $\mathbf{e}_o = \frac{1}{\sqrt{2}}(\hat{i} + \hat{j})$  defined by  $h + k = m$ . The coefficients perpendicular to the polarization are again summed up as shown in Fig. 5.2 (b). In this case spacing between the coefficient is reduced to  $\frac{2\pi}{\sqrt{2}d}$ . The Fourier transform of the coefficients is shown in (d). Again, from the projection slice theorem, this line is the cut along [110] direction of the unit cell of the potential (b) passing through its origin. This line will have Fourier coefficients spaced at  $\sqrt{2}d$  distance.

Hence, a laser projection along [110] direction will probe the slice of the potential along this direction. A two dimensional potential can, in principle, be probed by obtaining the lines at all possible orientation of the crystal. However, for any arbitrary direction of the crystal, given by  $\tan^{-1}(p/q)$  where  $p, q$  are integers with  $q \geq 0$ , the spacing between the coefficients reduces to  $\frac{2\pi}{d(p^2+q^2)}$ . This increases the number of coefficients needed for fitting and reduces the confidence of fitting significantly making the technique error prone.

But, the fitting along the [100] and [110] directions already contain the information of all the Fourier coefficients. Using fitting along one more direction [120], provides us enough information to extract all the coefficients and hence obtain an image of the two dimensional valence potential. The method for this is detailed in the next section.

## 5.2 2D reconstruction from few projections

The reconstructed Fourier coefficients along a particular crystal direction comprises of the sum of projections of the all coefficients along that direction. Hence, apart from the coefficients perpendicular to that direction, which have zero projection, all other coefficients contribute along this direction. For a complete knowledge of Fourier coefficients of the 2D slice of valence potential, a sufficient condition is the reconstruction in a few directions, using which a system of linear equations can be solved to obtain all the Fourier coefficients.

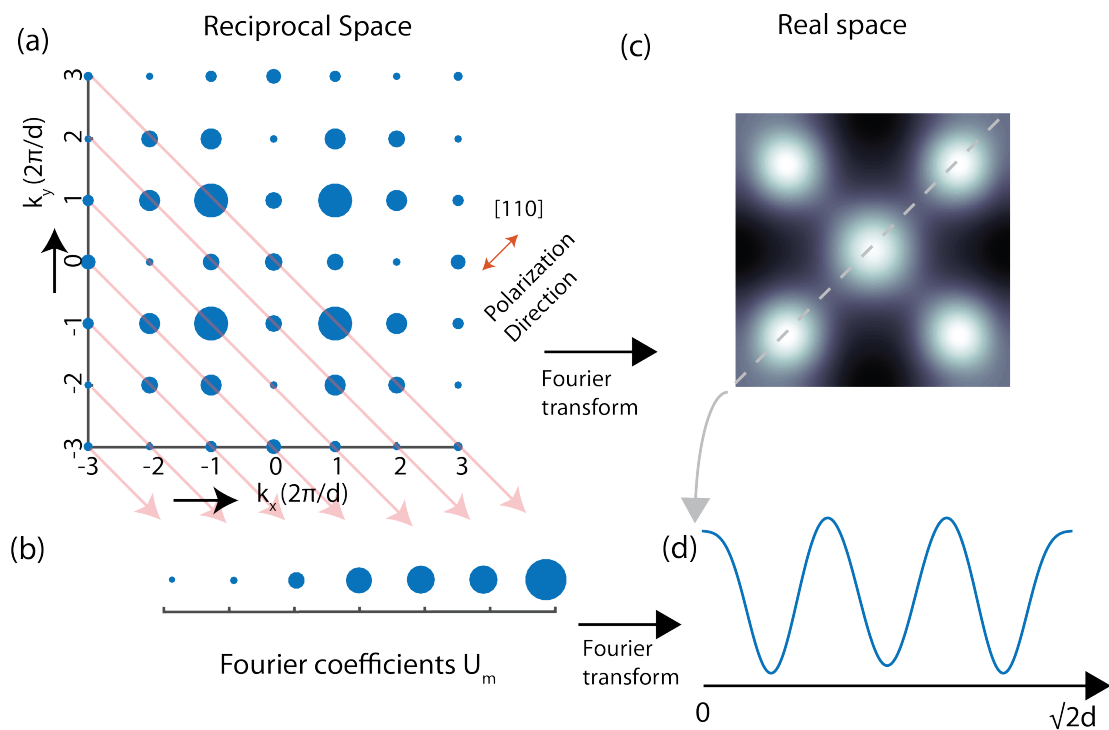


Figure 5.2: (a) Reciprocal space of a symmetric system. Amplitude of the Fourier coefficients is depicted by the size of the filled circle. The laser is polarized along the [110] direction of the crystal. (b)  $(U_m)$  obtained by summing the Fourier coefficients along the direction perpendicular to laser polarization. (c) The symmetric potential obtained by Fourier transforming the coefficients in (a). (d) Slice of potential along [110] direction of crystal, which is also the Fourier transform of  $U_h$  according to projection-slice theorem.

### 5.2.1 Principles of the 2D reconstruction method

Given a limited number of projections, which are obtained from experimental data, the aim is to reconstruct a 2D slice of the periodic potential in one unit cell.

Assuming for simplicity a square unit cell with lattice constant  $a$ , we are interested in obtaining the 2D potential slice  $U(x, y)$ , which, when expanded in a Fourier series, takes the form

$$U(x, y) = \sum_{kl \in \mathbb{Z}} U_{kl} e^{i \frac{2\pi}{a} kx} e^{i \frac{2\pi}{a} ly}, \quad (5.6)$$

where  $U_{kl}$  are the structure factors of the 2D potential. We assume as given a number of projections, which can be obtained either from theoretical calculations or from fitting to experimental data. A projection  $P_{pq}$  is a list of complex numbers that can be obtained by summing the structure factors along parallel lines through reciprocal lattice points oriented at an angle of  $\arctan(q/p)$ . Here  $p, q$  are integers with  $q \geq 0$ , which specify the angle at which the projection is performed. Since  $q/p$  is a rational number, the 1D real space slice of the periodic potential through the origin along such a direction is a periodic function of the line parameter. Accordingly, the Projection-Slice theorem applies and can be made use of to establish a relationship between lines in real space and projections of structure factors in reciprocal space. In detail, the projections are calculated as

$$P_{pq}(b) = \sum_{k, l \in \mathbb{Z}} U_{kl} \Delta(b + kq - lp). \quad (5.7)$$

Here the Kronecker delta function  $\Delta(k)$  equals one when  $k = 0$  and zero otherwise. The parameter  $b$  specifies along which of the parallel lines a summation was performed.

In practice only a finite number of projections (parameterized by a finite number of values for  $b$ ) is obtained for a given angle  $(p, q)$  by fitting to experimental data. This corresponds to a finite resolution. Although any angle can be approximated by a pair of integers  $(p, q)$ , it is difficult to obtain projections for large values  $p, q$  from experimental data. This is because the number of projections that have non-vanishing contributions from structure factors within a given radius in reciprocal space (corresponding to a given resolution in real space) quickly increases for larger values of  $p, q$ . For the present approach we only use a limited number of angles, i.e. sets of integers  $(p, q)$ .

Using the known symmetries of the potential, we then solve a system of linear equations to obtain all structure factors within a certain radius from data corresponding to a few projection angles. The symmetries of the 2D potential lead to a number of linear constraints. In practice these constraints can imply that the structure factors are real for inversion symmetric potentials, as well as modeling mirror axes and rotations as linear maps between sets of  $N \times N$  coefficients. No interpolation is necessary at this step since the axes and rotation angles necessary for the materials always map the lattice to itself.

The system of equations is solved by standard linear least squares methods. We seek

to find the Fourier coefficients  $U \in \mathbb{C}^{N \times N}$  as the solution for

$$\text{minimize} \quad \|L[U] - h\|^2 \quad (5.8)$$

$$\text{subject to} \quad S[U] = 0, \quad (5.9)$$

where  $h$  is a vector containing the projections for all angles in use and  $L$  is a linear map stringing the projections as given by Eq.5.7 with summation indices restricted to the  $N \times N$  grid. Finally,  $S$  is another linear map implementing the condition that coefficients be real and symmetric with respect to given mirror axes or rotations, depending on the material.

The final result is a 2D slice of the potential. The approach requires that structure factors outside the specified radius are zero and thus the validity of all the results hinges on the assumption that they are in fact negligible. This leads to a delicate balance: on the one hand, the cutoff radius can not be taken arbitrarily large. This is due to the requirement that the limited projection data and symmetry constraints on the potential should be sufficient to uniquely reconstruct the Fourier coefficients of a plane. On the other hand, the cutoff radius needs to be sufficiently large for the *actual physical potential* to have vanishing structure factors outside it. Whether the cutoff radius used is sufficiently large can be judged in practice from the quality of the least square fit upon solving the over-determined system of equations with linear constraints, and by comparing the end result to potentials obtained theoretically or experimentally by other methods.



# Chapter 6

## Experimental setup

*You become responsible forever for what you have tamed. You are responsible for your rose.*

- Antoine de Saint-Exupry, Le Petit Prince

This chapter provides the experimental details of the picoscope apparatus. We start with presenting the basic elements needed to build such device and then discuss in detail each of the elements and how they function in our laboratory setup.

### 6.1 Elements needed for the picoscope

The development of a picoscope requires the following basic elements:

- **LASER SOURCE** A pulsed light source must have photon energy higher than the inner potential of the crystal to be in high frequency regime. The laser pulses must be well characterized with precise knowledge of its amplitude and waveform. In our experiments, this information is obtained by the attosecond streaking technique (section 6.3.1).
- **CRYSTALLINE SAMPLE** The crystalline sample must be thin so that the propagation of laser pulses inside the sample does not distort the waveform. The experimental setup used in this thesis can only support free-standing samples however picoscopes can also be developed to support crystalline material coated on a substrate.
- **ROTATABLE SAMPLE HOLDER** In order to probe the potential of crystal in different directions, a rotatable sample holder is needed. The sample holder presented in the thesis allows rotation only along one axis of the crystal. Hence, the valence potential of a 2D slice of the crystal can be imaged. It can be upgraded in order to provide rotation along the other axis of the crystal and thereby reconstruct the 3D valence densities.
- **SPECTROMETER** The spectrometer must be able to record all the harmonics emanating from the crystalline sample and hence must be sensitive to a wide range of frequencies.

## 6.2 Picoscope apparatus

Figure 6.1 shows a schematic of the picoscope. A crystalline sample is exposed to a laser beam whose amplitude and waveform has been precisely characterized at the position where laser-sample interaction takes place. The intensity yield of the emitted laser harmonics from the crystal for an increasing field strength of driving pulse is recorded using the spectrometer. The procedure is repeated for different crystal orientations.

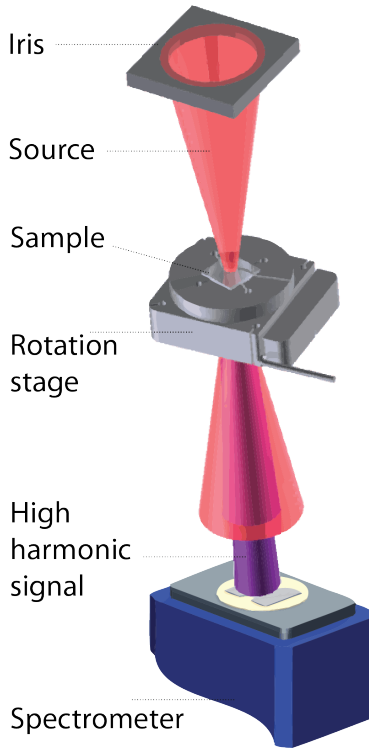


Figure 6.1: Schematic diagram of a picoscope. The crystalline sample is placed on a rotation stage and exposed to an intense laser pulse (red beam). The emitted harmonic spectrum (blue beam) from the crystal is recorded by the EUV spectrometer.

## 6.3 Details of the developed picoscope

### 6.3.1 Light Source

#### Oscillator

A Titanium Sapphire crystal based oscillator system (RAINBOW<sup>TM</sup>) is pumped by 3W, 532 nm, Nd-YAG continuous-wave Verdi V6<sup>TM</sup> laser and generates pulses with the energy of 3-4 nJ, the pulse duration of 6 fs and repetition rate of 78 MHz.

### Amplifier

The process of chirped pulse amplification [91] is used to amplify the energy of each pulse from the oscillator. The pulses exiting the oscillator are first stretched to 25 picoseconds via propagation through a thick slab of flint glass and then seeded to a multi-pass amplifier to increase their energy. Faraday isolator is used to prevent the amplified pulses from returning to the oscillator and avoid damaging the crystal. The amplifier system consists of a Titanium Sapphire crystal pumped by a Q switched Nd:YLF pump laser. The seed pulse from the oscillator is amplified by first passing it four times through the crystal in a crossed-beam setup as shown in Fig. 6.2. After the fourth pass, the beam is passed through the Pockel cell. The Pockel cell reduces the repetition rate from 78 MHz to 3 KHz. The p-polarized pulses are amplified further, by passing it 5 times through the crystal. The seed pulse experiences the process of gain narrowing every time it passes through the crystal where the central region of the spectrum experiences higher gain compared to the wings, thereby reducing the spectral bandwidth. To compensate for the gain narrowing, the pulses are passed through a dazzler. The dazzler works on the principle of acousto-optic dispersion. It consists of a birefringent crystal sandwiched between RF (radio frequency) generators. The acoustic waves inside the crystal, generated by the RF generators, diffract the seed pulse where its diffraction efficiency can be programmed according to the need. In our system, the dazzler is programmed to create a hole in the spectra to compensate for the gain narrowing. It is also used to compensate for the higher-order dispersions in the pulse. The amplified pulses are compressed using two transmission gratings to produce nearly Fourier-limited 3W, 1mJ, 21fs pulses at 3KHz with central wavelength of 800nm and bandwidth of 60nm.

### Hollow-core fiber

The amplified pulses are further spectrally broadened in a hollow-core fiber compressor. They are focused with 1.8 m focal length lens on the entrance of the 1.1 m long hollow-core fiber having 250  $\mu\text{m}$  core diameter. The fiber is filled with neon gas at around 2 bar pressure. The beam enters the tube containing hollow-core fiber through a 500  $\mu\text{m}$  thick anti-reflection window and exits from a second 500  $\mu\text{m}$  thick fused silica window mounted at Brewster's angle. Each window is mounted at 0.8 m distance from the fiber. The pulses undergo self-phase modulation inside the fiber to increase their frequency components (Fig. 6.3). The output from the fiber is a supercontinuum with wavelengths ranging from deep ultraviolet (230 nm) to infrared (1100 nm). The initially diverging beam emerging from the fiber is collimated using a toroidal mirror with  $R_h$  of 8000 mm and  $R_v$  of 260 mm and then compressed by dispersive mirrors in the Synthesizer (section 6.3.1).

### Phase stabilization of the pulse

The change in the dispersion inside the cavity due to thermal fluctuations can change the carrier offset frequency. We apply two mechanisms to lock the  $f_{CEO}$  to a predefined value. The first method uses the concept of difference frequency generation. The difference

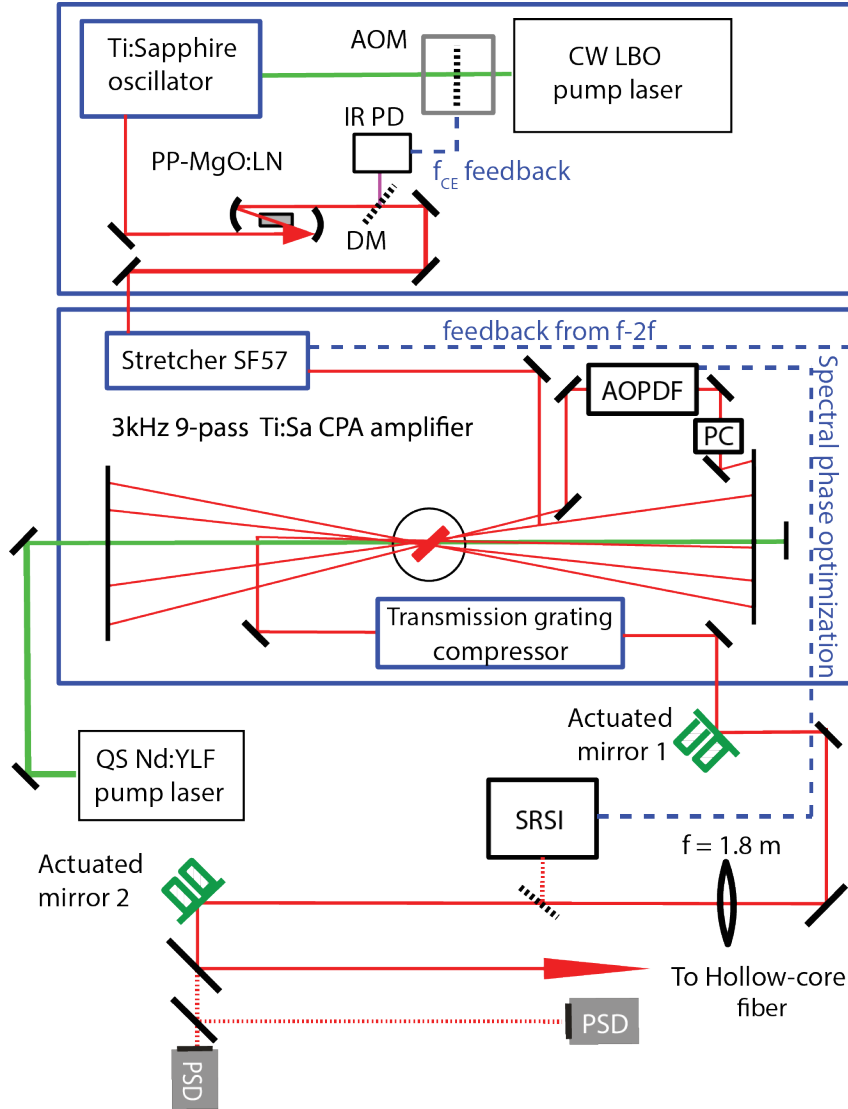


Figure 6.2: Schematic of the laser setup used for the experiment in this thesis. Adapted from PhD thesis of Manish Garg.

frequency defined as  $f_{diff} = f_{CEO} + n f_{rep} - f_{CEO} - m f_{rep} = (n - m) f_{rep}$  is inherently free from a carrier envelope phase and can be used as the reference. Inside the oscillator, a periodically poled lithium niobate crystal (PPLN) is used to generate the difference frequency spectrum. The difference frequency spectrum and the cavity spectrum have some overlap, which causes interference and yield a beat signal which also contains the carrier envelope phase  $f_{CEO} + n f_{rep} - n f_{rep} = f_{CEO}$ . The beat signal has a very low frequency and is separated from the rest of the signal by using a low pass radio frequency filter. The filtered signal is detected using an avalanche photodiode. If  $f_{CEO}$  is stabilized to  $\frac{f_{rep}}{4}$ , every fourth pulse in the oscillator will then have the same phase. Since we already reduce the frequency from 78MHz to 3KHz while amplifying the pulse, all pulses from

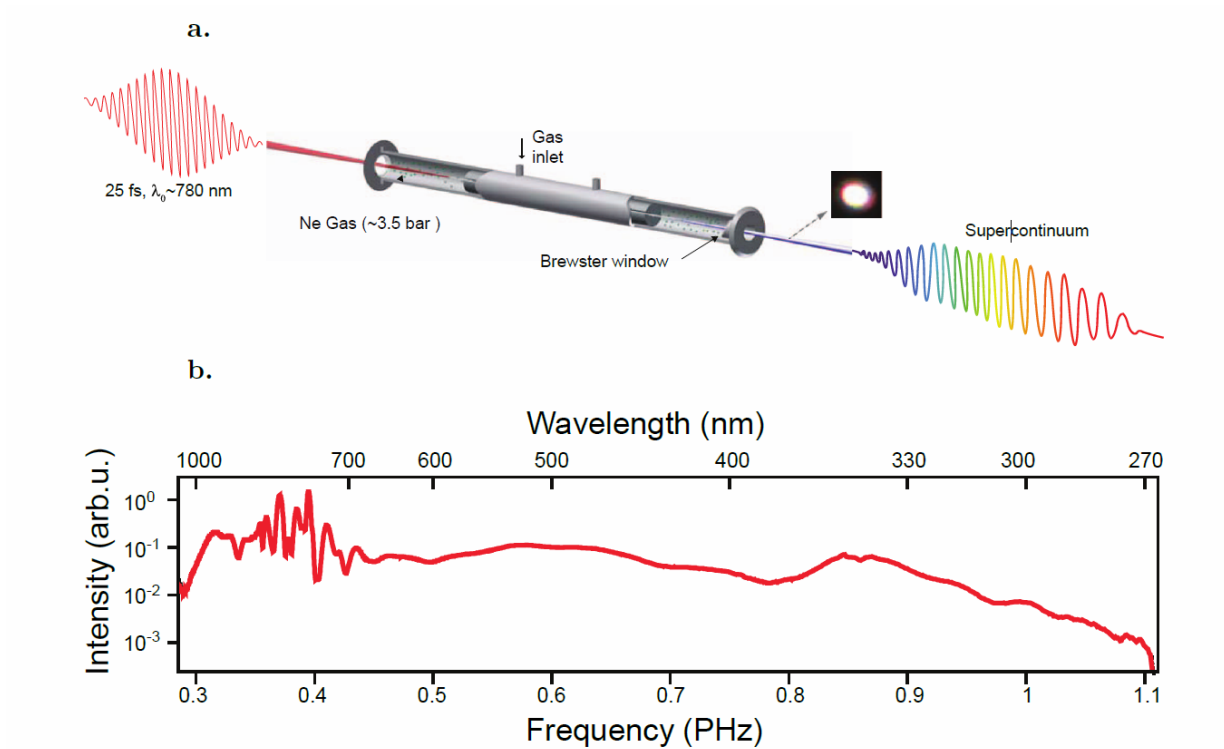


Figure 6.3: (a) Schematic of spectral broadening using a gas filled hollow-core fiber. (b) The spectra of the emitted super continuum encompassing multi-octave bandwidth. Adapted from reference [92].

the amplifier have the same phase. After detecting the phase of the pulse, feedback is provided to the acousto-optic modulator (AOM) to modulate the intensity of the pump laser entering the oscillator. The changes in intensity of the pumps change the phase of pulses exiting the cavity due to the Kerr effect.

A phase slippage is acquired by the pulses while they propagate through the amplifier and the hollow-core fiber. We again correct this phase slippage using another technique. In this technique, a beta barium borate (BBO) crystal is used to generate a second harmonic signal. The interference between the frequency doubled spectrum at its low end and fundamental spectrum at its high end, i.e.  $f_{CEP} - 2nf_{rep} - 2(f_o - nf_{rep}) = f_{CEP}$  is used to obtain the carrier envelope phase. Feedback is given to the glass wedges in the stretcher of the amplifier to correct for the phase offset.

### Light Field Synthesis

The most popular method to compress the pulses down to few-fs pulse duration after exiting the hollow-core fiber is to reflect them off a series of chirped mirrors. In our laboratory, we have enhanced the capabilities of tailoring and controlling light sources to fit our needs by synthesizing the electric field, while compressing it down to sub-fs pulse duration. The technology of light field synthesis made possible the production of the shortest pulse in optical wavelength regime with around 400 attosecond duration [15].

The broadband light emanating from the fiber is split into four spectral bands (four channels) of nearly equal width using dichroic beamsplitters as shown in Fig. 6.4. Pulses in each channel are compressed by reflection off six chirped mirrors. The pulses from each channel are characterized using transient grating- frequency-resolved optical gating (TG-FROG). Each channel, except one (yellow) consists of a set of two mirrors placed on the piezoelectric stage to control the relative delay between them. Finally, the pulses from each channel are recombined using the dichroic beam-splitters of the same type to produce a synthesized pulse.

The spatial overlap of the beam profile is ensured by overlapping the beams from the individual channel in the focal plane using a CCD camera. The temporal overlap between pulses in different channels is attained by maximizing the highly non-linear process of high harmonic generation from the Neon gas.

The Synthesizer is actively and passively stabilized to ensure long term sustainability of the synthesized fields. For passive stabilization, the whole setup is assembled on a monolithic aluminum base plate whose temperature is stabilized by circulating water at 20°C. The active stabilization is achieved by interferometric path length stabilization. More details about the synthesizer can be found in the references [93] and [15].

The frequency-resolved optical gating (FROG) technique is only suitable for finding the amplitude and phase of many-cycle pulses. The light pulses produced from the synthesizer, however, may contain close to or less than a single cycle of a pulse. Attosecond streaking, discussed in the next section, provides a way to characterize the pulses from the light field synthesizer. Once the field form is known, pulses in each channel can be delayed by a known amount to synthesize the required pulses. Repeating the procedure of synthesis and

characterization finally results in the desired waveform which can be actively stabilized.

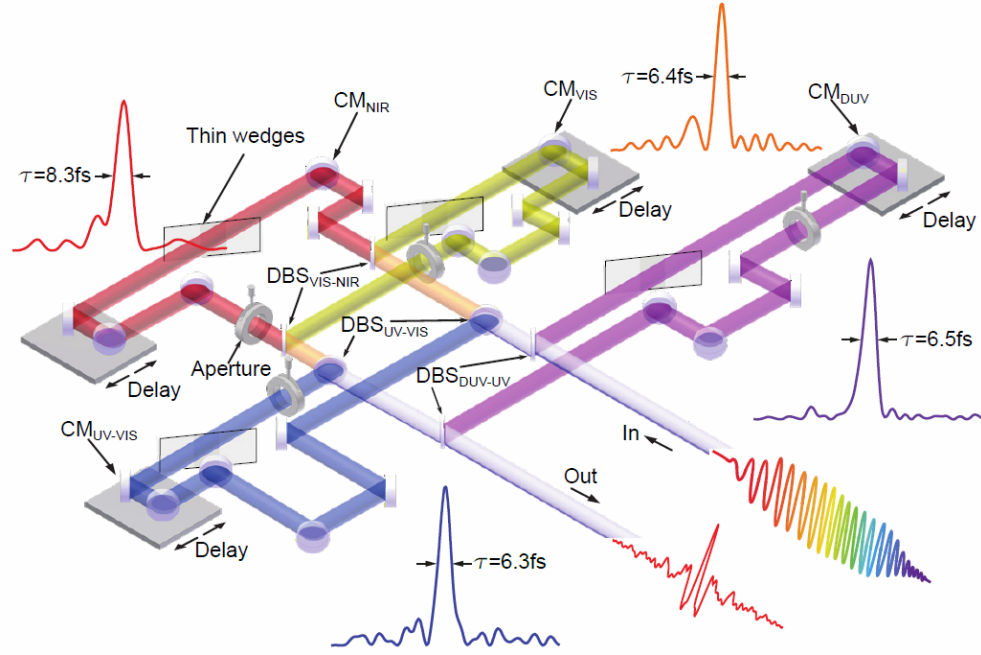


Figure 6.4: Schematic diagram of the light field synthesizer. Supercontinuum with multi-octave spectral bandwidth is split using the dichroic beamsplitters (DBS) into 4 different spectral channels, shown with 4 different colors. Pulses in each channel are compressed by reflections off 6 chirped mirrors. Aperture and wedge, placed in each arm of the synthesizer, control the amplitude and the carrier envelope phase, respectively. The beams from the individual channel are combined again using the same type of beam splitter to produce the synthesized field at the exit of the apparatus. Adapted from reference [92].

### Attosecond streaking

In the experiments presented in this thesis, precise knowledge of the laser waveform and its amplitude is of immense importance.

The short intense optical pulse obtained from the synthesizer is directed into the first chamber- the HHG chamber. They are focused into a nickel tube (2.2mm thick) filled with neon gas using a 32.5 cm focusing mirror. The interaction of the high-intensity laser pulse with the gas atoms leads to the generation of extreme ultraviolet (EUV) pulses. The emitted EUV pulse and the optical pulse co-propagate through differentially pumped chambers towards the experimental chamber. Owing to the lower divergence of EUV pulses (inner beam) compared to the optical pulses (outer beam) they can be spatially separated using a metallic filter (zirconium/ aluminum) suspended on thin 30  $\mu\text{m}$  tungsten wire

having the same diameter as the EUV beam. The metallic filter is selected such that it only transmits the high-energy spectral part of the EUV pulse so as to generate an isolated attosecond pulse. The beam profile and the intensity of the beam EUV pulse is measured using a EUV-CCD camera placed at the end of the experimental chamber. Both the EUV and optical pulses are focused into another gas target by a 12.5 cm concave dual-mirror module made by concentrically cutting a single concave mirror. The two mirrors can be delayed relative to each other using the piezo stages. The inner mirror is an EUV multi-layer mirror optimized at 80 eV, while the outer mirror is optimized to boost the signal from blue and UV channels and suppress the frequency components from the red channel so as to compensate for the skewness in the spectra of the optical pulses. The pulses from both mirrors are then focused on Ne gas nozzle. The high photon energy EUV beam ionizes the Ne atoms. A time of flight (TOF) spectrometer mounted on top of the gas jet is used to capture electrons emitted along the laser polarization vector. The TOF spectrometer measures the kinetic energy of electrons by measuring the delay between the trigger and arrival of the electron on an MCP plate. The TOF spectrometer is pumped with a dedicated turbopump which maintains vacuum around  $10^{-7}$  mbar pressure. The gas jet target is also placed on a 3D piezo stage so that once the field is characterized at the location of the gas target, the jet can be moved out and the sample under study can be placed. This allows for knowledge of exact field strength at the position where laser interacts with the sample. The inner and outer beams can also be imaged and spatially overlapped using the imaging setup placed at one of the exit ports of the chamber. These beams are picked up by the translation D mirror and passed through an aberration-corrected biconvex lens, which collimates and magnifies the beam size by a factor of four on the camera. The coarse temporal overlap between the beams is achieved by maximizing the overlap signal on the camera. The power of each beam is also measured on the same port using a power meter.

### Pulse measurement with attosecond streaking

The temporally and spatially overlapping XUV and optical pulses are shot on the neon gas jet. The XUV pulse with central energy of around 80 eV ionizes the neon gas atoms. The electron emitted from gas atoms are then moved by few-cycle optical pulse and finally, these electrons are detected by the TOF spectrometer. The intensity of the optical pulse is adjusted so that it does not ionize the atoms and merely modifies the momentum of the electron. The momentum gained by the electrons due to the optical field is given by  $\Delta p = -e \int_{t_0}^{\infty} E_L(t) dt$ , where  $t_0$  is the time of birth of the electron and  $E_{NIR}$  is the electric field of the optical pulse. The TOF spectrometer measures the time of flight of electrons, which corresponds to the kinetic energy of the particle. Assuming the initial velocity at the time of birth is  $v(t_0)$ , then using the change in momentum formula above, the kinetic energy can be given as  $E_{KE}(\infty, t_0) = \frac{1}{m_e} \left[ v(t_0)^2 - \frac{2e}{m_e} A_L(t_0) v(t_0) + \left( \frac{e}{2m_e} \right)^2 A_L(t_0)^2 \right]$  where  $A_L(t) = \int_{t_0}^{\infty} E_L(t) dt$  is the vector potential. As stated earlier, we keep the intensity relatively low so as not to ionize the neon with the optical pulse, thus  $A_L(t_0)^2$  can be neglected. The change in kinetic energy is then given by  $\Delta E_{KE} \approx -\frac{2e}{m} A_L(t_0) v(t_0)$ . Delaying the XUV pulse with

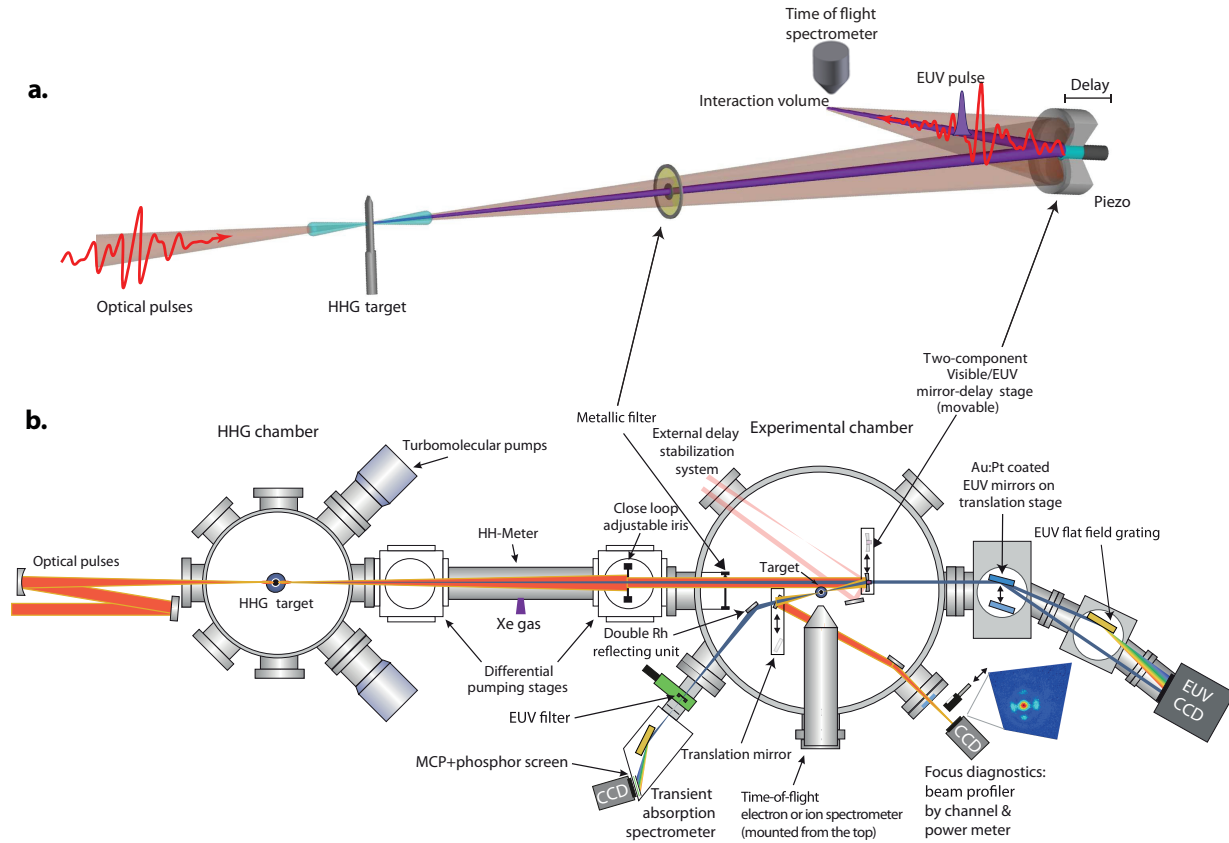


Figure 6.5: a. Schematic diagram of the attosecond streaking setup b. From the right side, a single-cycle optical pulse from the synthesizer enters the first chamber maintained at  $10^{-3}$  mbar. The optical pulse is focused on the HHG target, which is a tungsten tube with a hole of around  $250 \mu\text{m}$  filled with the noble gas (Ne), to generate EUV pulse shown in blue. The second chamber is the experimental chamber maintained at  $10^{-6}$  mbar in which both attosecond streaking and picoscopic measurements are performed. Adapted from the thesis of Dr. Manish Garg.

respect to the optical pulse would mean changing the time of birth of the electron with respect to the optical pulse. This pump-probe technique provides a trace at every delay point as shown in the Fig. 6.6 which is directly related to the optical field as shown in the equation above. For quick, but still precise analysis, the centroid of the momentum distribution from the streaking trace is calculated. This centroid can be interpreted as the vector potential  $A(t)$  from which the electric field can be deduced. Using the knowledge of the spectral bandwidth, the spectrum of the individual channel is retrieved. Knowledge of field strength and waveform of pulses in each channel is used to obtain the desired waveform of the output pulses from the light field synthesizer.

### 6.3.2 Crystalline sample

The crystalline samples used in the experiments were commercially obtained. Figure 6.7 shows a freestanding crystalline sample. Polishing and etching techniques were used to decrease the thickness of the bulk crystal to the desired size. The thickness of the commercially obtained films was confirmed using a white light interferometer.

### 6.3.3 Rotation stage and sample holder

The concepts presented in this thesis requires sampling of the intensity of harmonics at various orientations of the crystal. Also, the sample must be placed at the location inside the experimental chamber where the field strength is characterized. The streaking nozzle is placed 5 mm below the TOF spectrometer hence our sample holder of the crystal must be constrained to that location. We constructed the sample holder using a rotation stage, two gears and a belt. The gear with a smaller radius was placed exactly at the location of streaking nozzle. This gear was attached to larger gear, placed on the rotation stage, with a conveyor belt. The whole system was mounted on a translation stage so that after streaking measurement of the field of the pulse is performed, the position of streaking target and sample holder can be exchanged. The same stage was also used to change the spot exposed to the laser beam so that a fresh spot on the sample can be exposed after potential damage.

### 6.3.4 EUV spectromter

In our experiments, using the optical fields, the harmonics from solid samples are generated with a cutoff around 40 eV. To capture all the harmonics, we built a spectrometer which covers the spectral range of 8eV to 45eV using a Hitachi flat field grating with 1200 grooves/mm and the blaze angle of 3.2 degrees. The grating was mounted on a rotation stage and was housed inside a custom-built vacuum chamber. In our spectrometer design, instead of moving the detector we rotate the grating so that the grazing angle of incidence of the incident beam can be changed. Rotating the grating gives us the freedom to select the spectral range captured by the detector. A 3 stage (z-stack) multi-channel plate (MCP) was used to detect the EUV photons and the fluorescence signal on the MCP phosphor

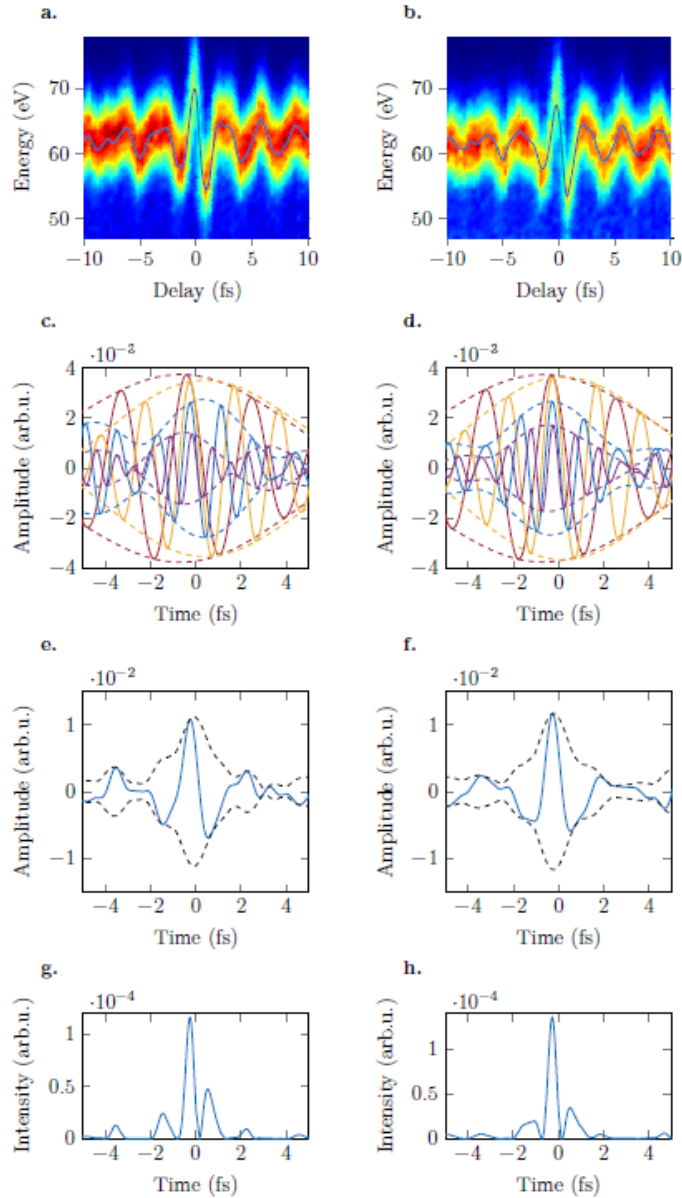


Figure 6.6: (a) and (b) show streakings with superimposed centroid (blue). (c) and (d) show the corresponding channel decomposition. (e) and (f) show the total electric field and (g) and (h) the intensity. The left side shows initial waveform, the right side after optimization.

screen was then imaged using an optical camera. The energy calibration of the spectrometer was performed using gas harmonics. To detect the low harmonics in VUV range i.e. 3eV to 8 eV, a commercial spectrometer from McPherson was used.



Figure 6.7:  $\text{MgF}_2$  crystal with  $5 \mu\text{m}$  thickness and 2 mm diameter mounted on an cylindrical frame.

## 6.4 Picoscope

Fig. 6.9 shows a schematic of the picoscope apparatus used in the experiments. After the fields are characterized at the location of the streaking target, the position of the target and the sample is exchanged. Owing to the versatility of the light field synthesizer, 5 fs pulses centered at 585 nm exiting from the single channel of the synthesizer is used for the experiments while the other channels were blocked. The intensity of the beam is controlled by a motorized iris and the inner part of the beam is blocked with an aluminum filter. Outer mirror of the dual mirror module directs the pulses to the crystalline sample placed on the rotation stage. The spectrum emanating from the crystalline sample is focused using a pair of rhodium mirrors to the entrance of the spectrometer. The optical beam is dumped inside the spectrometer and the harmonic spectra is recorded. To measure the third harmonic ( $\sim 6 \text{ eV}$ ) a focusing mirror is placed at the position of the translation mirror and beam is directed towards the McPherson spectrometer. The optical beam is attenuated by reflecting the beam at Brewster angle off the Silicon wafers.

The close loop adjustable iris, the rotation stage, the optical camera on home built spectrometer and the CCD camera of the McPherson spectrometer were interfaced using the LabView software. This allowed quick and automatized acquisition of HHG spectra of the EUV pulse at required orientations of crystal and for required field strengths of the optical beam.

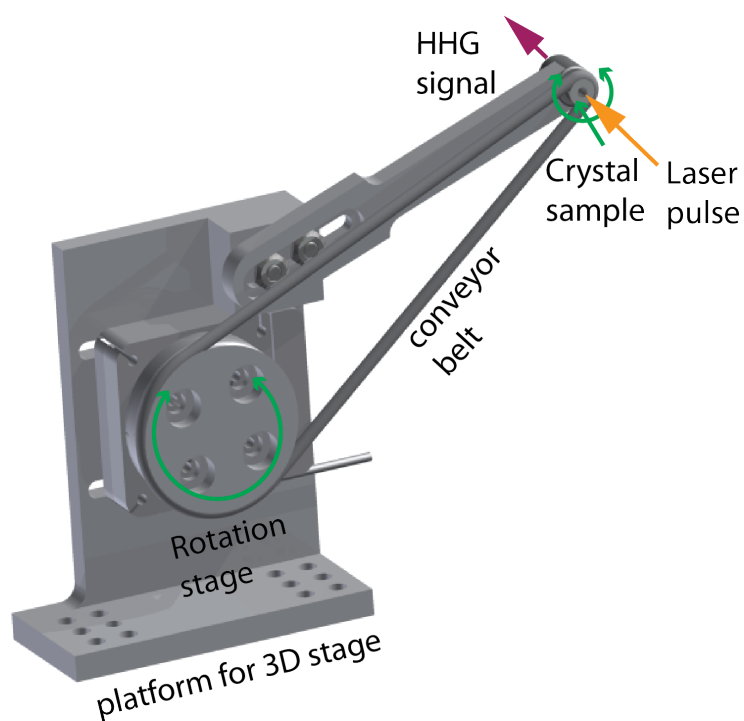


Figure 6.8: Schematic diagram of the sample holder. A conveyor belt connects the motorized rotation stage to the crystal sample holder. The distance between the center of the crystal sample holder to the TOF spectrometer is 5mm. This particular design allows the experiments to be performed at the exact streaking nozzle position and provides exact knowledge of field strength at sample location.

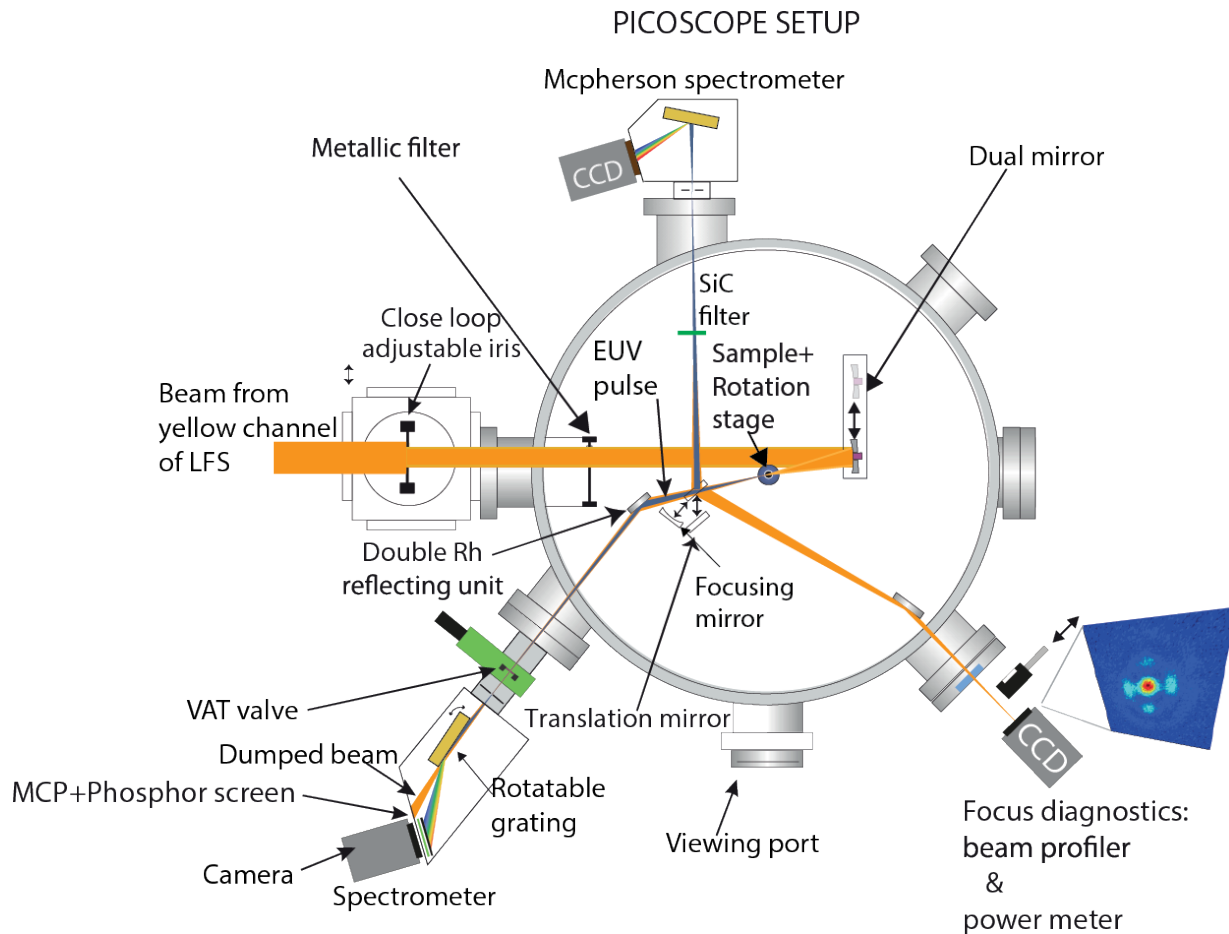


Figure 6.9: Schematic diagram of the picoscope. A few-cycle (5 fs) Pulses centered at the carrier photon energy of 2.1 eV is exposed to sample. The intensity of the beam is controlled by the closed loop adjustable iris. It is focused on the sample by reflection off the outer section of the concave mirror with 12.5 cm focal length. The beam exiting the sample is directed to a CCD camera and power meter by a mirror placed on a translation stage. This mirror is then removed and the harmonics generated (blue) by the sample is focused by double rhodium reflecting mirror on the spectrometer entrance. The optical beam is dumped inside the spectrometer and the HHG spectrum is measured using a 3 stage MCP phosphor screen detector. To measure third harmonic, the beam is directed to McPherson spectrometer using a focusing mirror. The optical beam is attenuated by 2 reflections off a Si wafer placed at Brewster's angle.

# Chapter 7

## Probing the radius of the smallest valence specimen in a crystal

### 7.1 Introduction

An essential implication of the high-frequency approximation is that the cutoff energy of the harmonic spectra is directly related to the radius of the smallest valence specimen in a crystal. High frequency approximation predicts that the cutoff energy  $E_{cutoff}$  is directly proportional to the driving field strength  $E_o$  and inversely proportional to the radius of the smallest specimen  $r_s$  and the frequency  $\omega$  of the driving pulse. The radius of the smallest specimen can be obtained as (chapter 3)

$$r_s = \frac{2\pi}{E_{cutoff}} \frac{E_o}{\omega} \quad (7.1)$$

Here we derive the radius ( $r_s$ ) of the smallest atom in different crystalline solids using the Eq.

### 7.2 Shannon radius

The most widely accepted radius of an ionic specimen is empirically calculated by Shannon [94]. The ionic radius has not been possible to measure. Conventionally, to estimate the ionic radius, atoms or ions were treated as hard spheres filling the unit cell. The internuclear distance was determined by X-ray crystallography which provides the length of each side of the unit cell. For example, in a crystal of NaCl, the length of the unit cell is measured as 5.64 Å. Ions in each side of the crystal have an arrangement given by Na<sup>+</sup> - Cl<sup>-</sup> - Na<sup>+</sup> ... and so on. Hence, the sum of the ionic radii of Na<sup>+</sup> and Cl<sup>-</sup> is equal to 2.82 Å which is half of unit cell length as depicted in Fig. 7.1. Shannon used the value of the ionic radius of O<sup>2-</sup> = 140 pm as a reference to estimate the ionic radius of all other species in crystals using the above method.

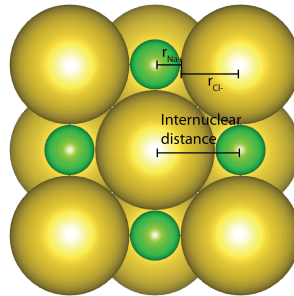


Figure 7.1: The internuclear distance measured using X-ray crystallography is apportioned between sodium and chlorine ions to calculate the ionic radius of the individual specie.

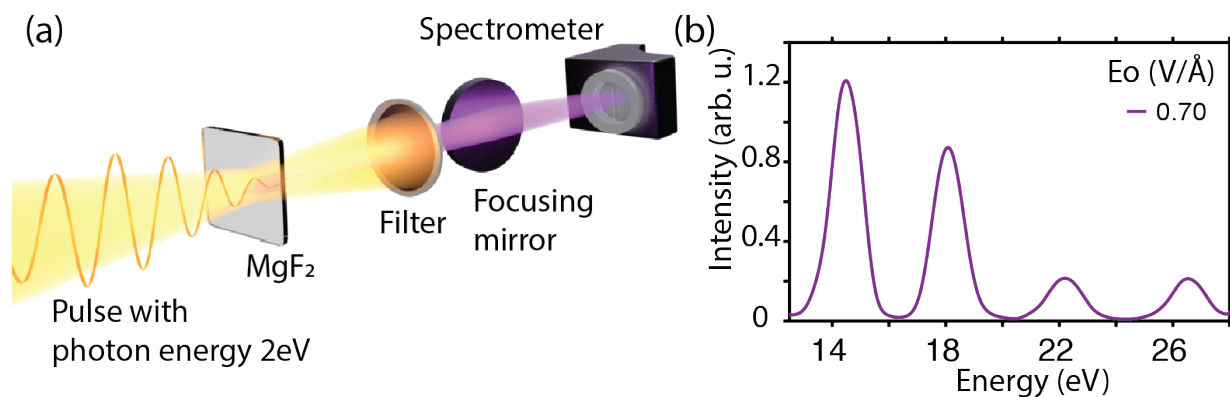


Figure 7.2: (a) Schematic diagram of experimental setup. (b) High harmonic spectra emanating from the MgF<sub>2</sub> crystal.

### 7.3 Measuring the radius of the smallest specimen (Mg) in MgF<sub>2</sub>

In order to estimate the cutoff energy the high harmonic spectrum emanating from MgF<sub>2</sub> was measured as shown in Fig. 7.2.

The dependence of cutoff energy of crystalline magnesium fluoride on driving field strength is shown in Fig. 7.3. It was obtained by recording the value of field strength when a harmonic peak was first observed in the spectrometer. It shows the values of cutoff energy at various driving field strength along [100] and [110] direction of the crystal. The error in the measurement of electric field strength is defined by the quanta with which driving field strength is increased. The blue and green shaded areas represent all the possible values that best fit of the experimental data along with its error.

The radius of the smallest specimen (Mg ion) in the crystal was obtained from the slope

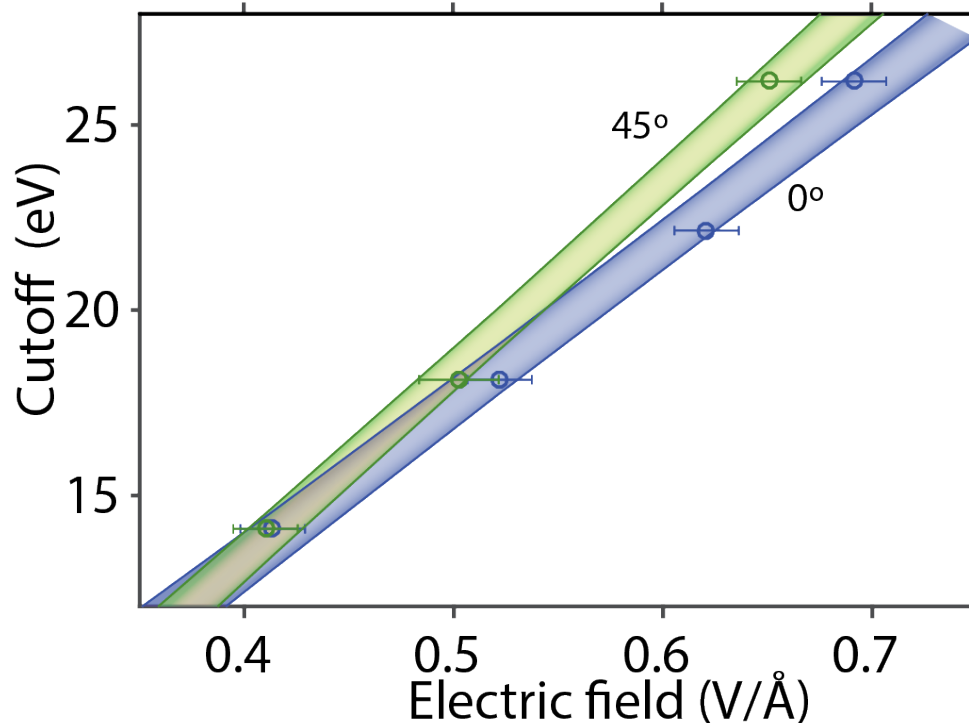


Figure 7.3: The dependence of cutoff energy ( $E_c$ ) on the driving field strength for [100] (blue) and [110] (green) crystal orientations of  $\text{MgF}_2$ . The width of the line shows all possible least square fitting of cutoff energy versus driving field strength.

of data in Fig. 7.3. We obtain  $r_s = 62 \pm 4$  pm in [100] direction of crystal and  $r_s = 59 \pm 4$  pm in [110] direction of crystal. The Shannon radius of  $\text{Mg}^{++}$  ion is 65 pm and Shannon radius of  $\text{F}^-$  ion is 126 pm [94]. Our experiment suggests that the smallest entity will have around 59 pm size in [110] direction of the crystal and 62 pm in [100] direction, which matches well the Shannon radius of the magnesium ion, the smallest valence specimen in  $\text{MgF}_2$  crystal.

The difference between the radius of magnesium observed in [100] and [110] directions suggests that the magnesium potential may not be completely symmetric but rather oblong shaped. In [110] crystal orientation, where magnesium shares an electron with the fluorine, its radius becomes smaller compared to the [100] orientation where it does not share any electron. The valence electron density calculated from DFT does not show the oblong magnesium because of the inherent assumption of spherical electron densities at the atomic sites.

## 7.4 Radius of smallest valence specimen in various crystals

We generalize the validity of the high-frequency approximation by experimentally measuring the cutoff energies for both wide and narrow band gap, ionic as well as covalent crystals. For this purpose we measure cutoff energies for two other ionic crystals, periclase (MgO) [95] with band gap 7.8 eV and zinc oxide (ZnO) with band gap 3.3 eV [96]. Furthermore, we measure cutoff energies for three covalent crystals, quartz (SiO<sub>2</sub>), diamond (C) and carborundum (SiC-6H) with band gap of 9.2 eV [97], 5.47 eV [98] ) and 3.05 eV [99] respectively. These materials were chosen so that the approximation could be tested on materials with both a narrow and wide band gap.

Table 7.1: Shannon radius ( $r_s$ ) of Ions and Atoms

Ionic Radius		Covalent Radius	
Ion	Ionic Radii (in pm) [94]	Ion	Covalent Radii (in pm) [100]
Zn <sup>+2</sup>	60	C	75
Mg <sup>+2</sup>	65	O	64
F <sup>-</sup>	129	Si	116
O <sup>-2</sup>	135		

The experimentally observed cutoff energies for maximum driving field strength sustained by all the above-mentioned materials are shown in Fig. 7.4. The measured values of the radii( $r_s$ ) of the smallest specimen in all these crystalline systems, extracted using their cutoff energy (Fig. 7.4) are shown in Fig. 7.5. Alongside, the ionic/covalent radii for all the specimens in the respective crystal obtained from Shannon theory is also mentioned for comparison. The measured ionic radii of the smallest specimens in the crystalline material match well with the radii obtained from Shannon theory. Hence, these measurements further corroborate the validity of high-frequency approximation in the studied solids.

## 7.5 Picometer scale resolution

By providing the direct access to the radius of the smallest valence specimen in various crystals which matches the Shannon radius very well we not only bolster the validity of our technique but also provide a method to directly access the valence radii with picometer-scale resolution. The measured radii of Mg, C and Zn are 59 pm, 70 pm and 64 pm, respectively.

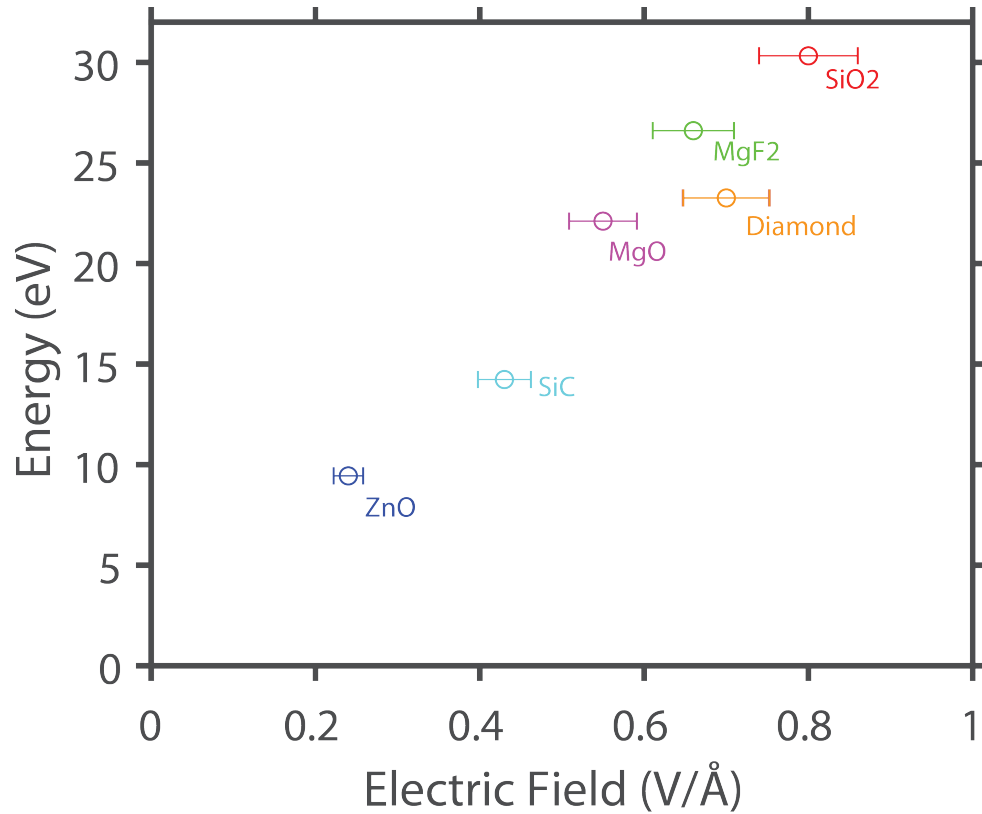


Figure 7.4: Measured cutoff energy as a function of driving field strengths for various crystalline materials.

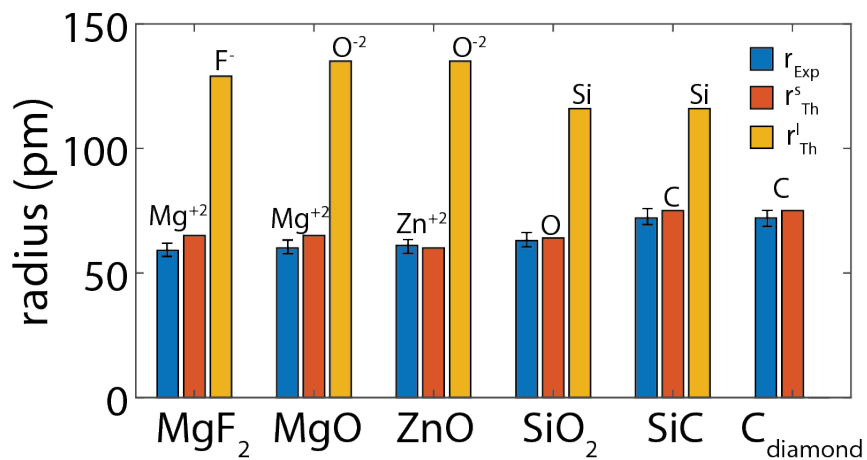


Figure 7.5: Comparison of the radius of the smallest specimen obtained experimentally (blue bar) with that of Shannon radius (red and yellow bars) for all the specimens present in the crystal.



# Chapter 8

## Picometer scale reconstruction of the valence potential of $\text{MgF}_2$

*When you come to the end of your rope, tie a knot and hang on.*

- Franklin D. Roosevelt

Utilizing the foundation laid in previous chapters, I attempt here to reconstruct the periodic potential of  $\text{MgF}_2$  crystal and compare it with the valence potential obtained from the density functional theory.

### 8.1 Crystal structure of $\text{MgF}_2$

The unit cell of crystalline  $\text{MgF}_2$  (Sellaite) as shown in Fig. 8.1 has a lattice constant of 4.64 Å along **a**, **b** axis and 3.05 Å along the **c** axis. In our experiments, laser impinges along the **c** axis of the crystal. The crystallographic direction [110] matches with the F-Mg-F molecular axis in the crystal shown in Fig. 8.1. The  $\text{MgF}_2$  crystal has two symmetry points, both located on the Mg ions. The two planes containing these non-equivalent symmetry points are highlighted in Fig. 8.1. These planes have exactly the same arrangement of ions but rotated by 90° and are shifted by half of the lattice constant along **a** and **b** axis.

### 8.2 The $\text{MgF}_2$ potential calculated using DFT

The valence potential of  $\text{MgF}_2$  was calculated using the density functional utilizing the Pseudodojo pseudopotentials and the FHI pseudopotentials as the basis set for the fluorine and the magnesium atoms, respectively. The Hartree density mesh cutoff was kept at 95 Hartree and 164 reciprocal space grid points were used to calculate the valence potential using commercially available DFT package (ATK-Quantumwise).

Fig. 8.2(a) shows the 2D slice of the valence potential of  $\text{MgF}_2$  calculated with DFT for the (001) and (002) planes (Fig. 8.1). The two non-equivalent symmetry points of

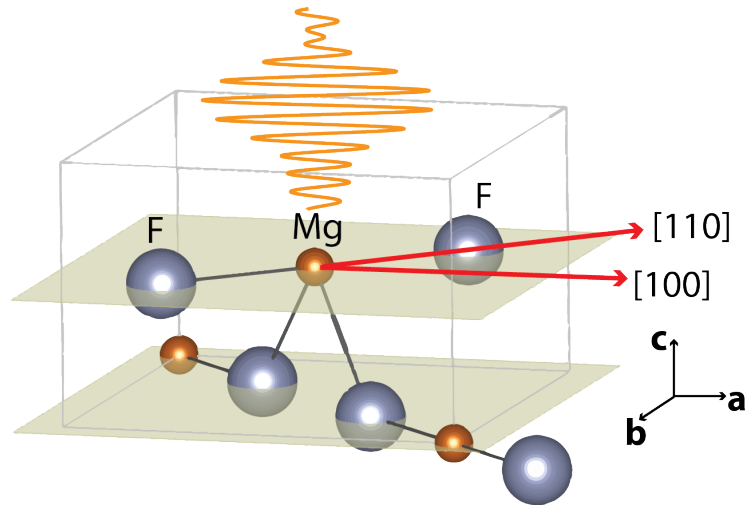
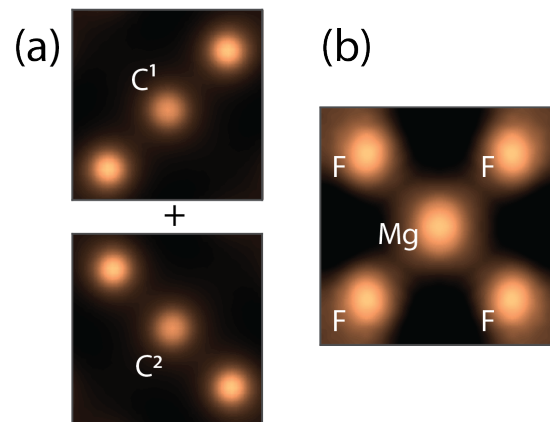
Figure 8.1: Unit cell of  $\text{MgF}_2$ .

Figure 8.2: (a) Valence electron potential of  $\text{MgF}_2$  for (001) and (002) planes as calculated by DFT.  $C^1$  and  $C^2$  are symmetry points of the crystal which coincide with the position of Mg. (b) Total potential calculated by summing the potential on each plane shown in (a).

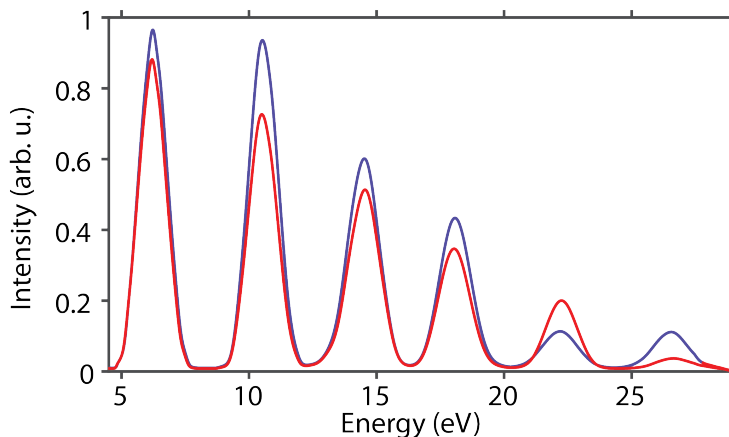


Figure 8.3: High harmonic spectra from  $\text{MgF}_2$  crystal driven by the laser pulses with a carrier photon energy of 2.1 eV polarized along the  $[100]$  direction shown in red curve and  $[110]$  direction shown in blue curve.

the crystal, located at the Mg atoms, are marked as  $C^1$  and  $C^2$ . Fig. 8.2(b) shows the sum of the planes of the valence potential such that their symmetry points coincide. The electric field of the high harmonic signal from both planes will be coherently added to form a summed up potential (Appendix B).

### 8.3 Experiments

An approximately  $5\mu\text{m}$  thick c-cut  $\text{MgF}_2$  crystal was exposed to few-cycle pulses with a central photon energy of  $\sim 2.1\text{eV}$ . The emanating HH spectra from the  $\text{MgF}_2$  crystal is shown in Fig. 8.3. The peak energy spacing of the harmonic spectrum matches well with the odd harmonics of the carrier frequency of the driving laser field verifying the coherence between the driving laser pulse and emitted EUV radiation.

Fig. 8.4(a) shows high harmonic spectra recorded when the driving field strength was varied from 0.46 to  $0.71\text{ V/\AA}$ . The spectral intensity scaling of individual harmonics with respect to driving field strengths shows a highly non-linear behaviour as shown in Fig. 8.4(b). The strength of driving electric fields in the experiments within  $\pm 10\%$  was obtained by using the attosecond streaking technique (chapter 5).

The sample was rotated with respect to the c-axis and the intensity yield of high harmonics for increasing driving field strengths were recorded for various orientations of the crystal. Figure 8.5 shows the harmonic spectrum recorded for 0 to  $2\pi$  rotation of the crystal. The step size of rotation was  $5^\circ$  and the driving field strength was  $0.7\text{ V/\AA}$ . The intensity yield at only 3 different orientations of the crystal was required for the valence potential reconstruction (section 5.2). The fitting in each direction provides the amplitude and phase of the Fourier coefficients in that direction.

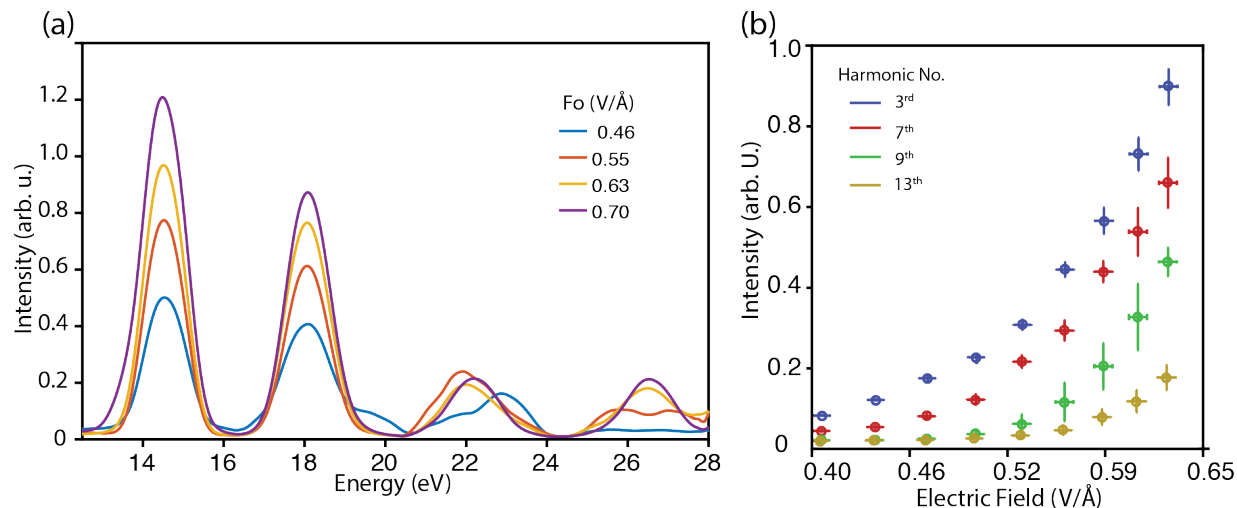


Figure 8.4: (a)  $\text{MgF}_2$  Harmonic spectra recorded for increasing field strength along [110] crystal direction. (b) Intensity yield versus field strength for 4 different high harmonic orders (shown in legend) as a function of increasing driving field strengths.

## 8.4 Retrieving the Fourier coefficients of $\text{MgF}_2$ potential

In order to retrieve the Fourier coefficients, the intensity yield of the emitted harmonics for various driving field strength along the [100] direction and [110] direction of the  $\text{MgF}_2$  were fitted using Eq.3.39. The mean of four consecutive measurements of intensity yield taken along [100] and [110] directions are depicted by red points along with their standard deviation in Fig. 8.6 and Fig. 8.7). The least square fitting, shown in blue curve, matches well with the intensity yield data where even the finer undulation of its build-up is captured precisely with our model.

## 8.5 Potential along [100] and [110] crystal direction of $\text{MgF}_2$

The coefficients  $U_h$  (described in Eq.5.4) retrieved by least square fitting of the field dependence on driving field strength along the [100] direction are plotted in Fig. 8.8. In addition, the coefficient  $U_m$  retrieved by fitting (Eq.5.5) along [110] direction is also shown in Fig. 8.8. It needs to be emphasized once again that coefficient along individual direction are not the cut along this direction in reciprocal space but the sum of the projection of all the coefficients along these directions (section 5.1.2)). Fourier transforming these coefficients gives us the cut along the [100] and [110] direction in the real space, as suggested by the Fourier slice theorem (Appendix D). Since the experimental data is normalized before fitting we are left with the ambiguity of the depth of the potential, just as in any

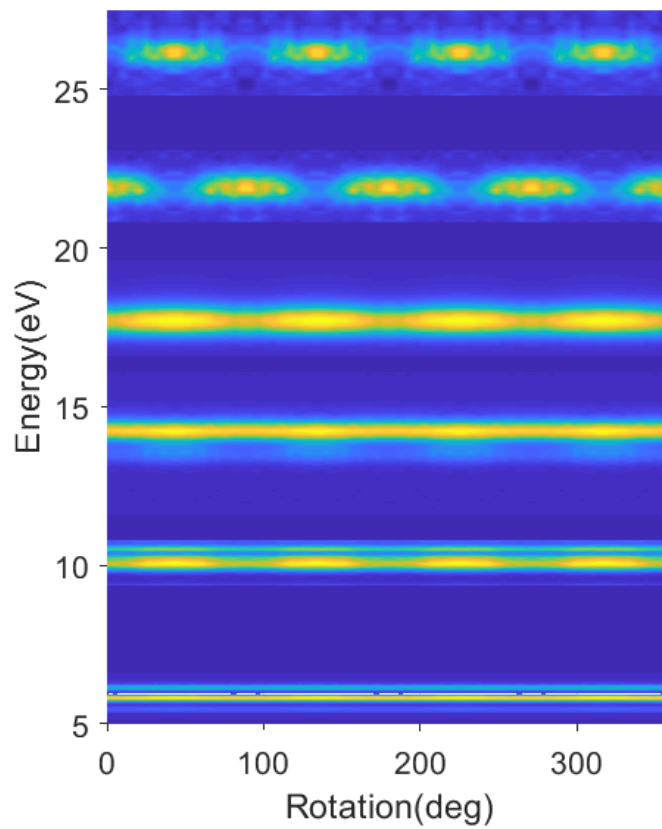


Figure 8.5: MgF<sub>2</sub> harmonic spectra recorded for different crystal orientations with 5° step size. The carrier frequency of few-cycle pulses is 2.1 eV with their electric field strength is 0.7 V/Å.

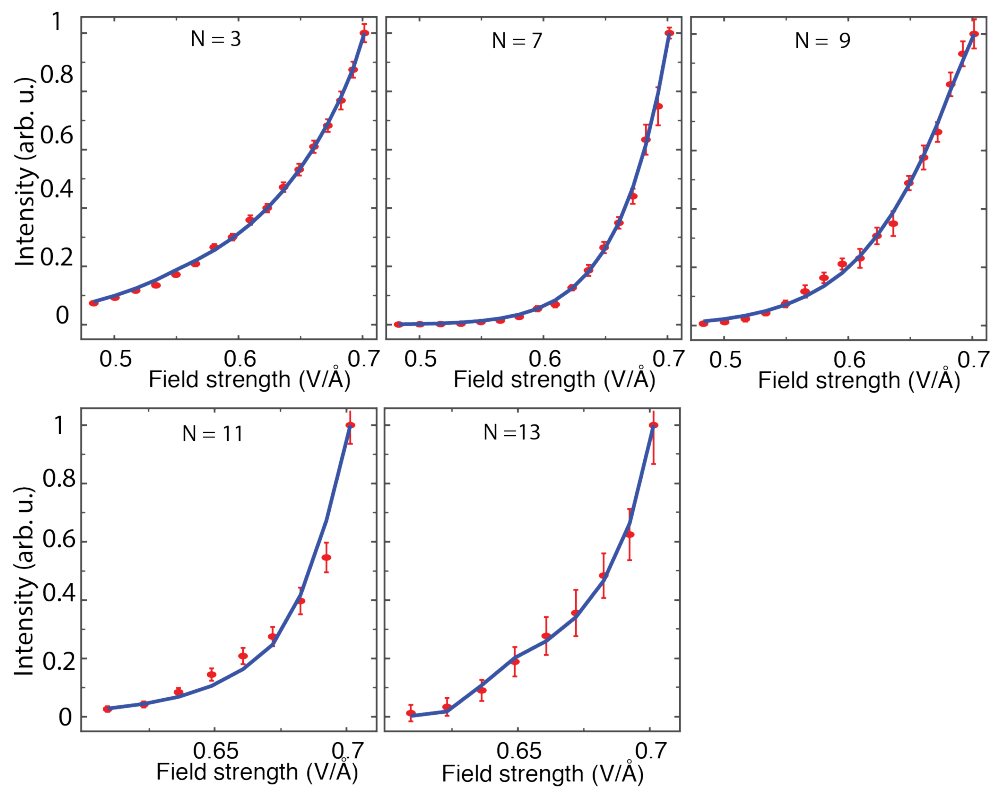


Figure 8.6: High harmonic yield versus field strength of the driving pulse aligned along [100] direction of the crystal. The least square fitting obtained using equation 3.39 is shown in the blue curve. The Intensity yield for each harmonic order ( $N$ ) is normalized by the maximum yield.

crystallographic measurement. The slices of the valence potential of  $\text{MgF}_2$  in real space obtained experimentally are shown in Fig. 8.8 and the corresponding slices of the potential from density functional theory are also plotted for comparison. The depth of the retrieved potential is chosen so as to match the DFT calculation to ease the comparison.

Fig. 8.8 shows that the along [100] direction of the crystal only  $\text{Mg}^{+2}$  ion is solely present. However, along the [110] direction 3 ions ( $\text{F}^{-1}\text{-Mg}^{+2}\text{-F}^{-1}$ ) are observed. As mentioned earlier  $\text{MgF}_2$  has two non-equivalent symmetry points on (001) and (002) planes. Hence the measured valence potential curve along the [100] and [110] axes comprise the addition of two parallel lines lying on these planes passing through the symmetry point. This means that the potential of Mg will be twice deeper than Mg potential on a single plane. The  $\text{Mg}^{+2}$  ion is smaller in size compared to the  $\text{F}^{-1}$  ion because of the electron transfer from  $\text{Mg}^{+2}$  to  $\text{F}^{-1}$ . Along the  $\text{F}^{-1}\text{-Mg}^{+2}\text{-F}^{-1}$  molecular axis ([110] crystal direction), sharing of electrons or bonding between  $\text{Mg}^{+2}$  and  $\text{F}^{-1}$  is also observed which is also in agreement with the theoretical predictions [101]. The measured potential is also in excellent agreement with the potential obtained from DFT.

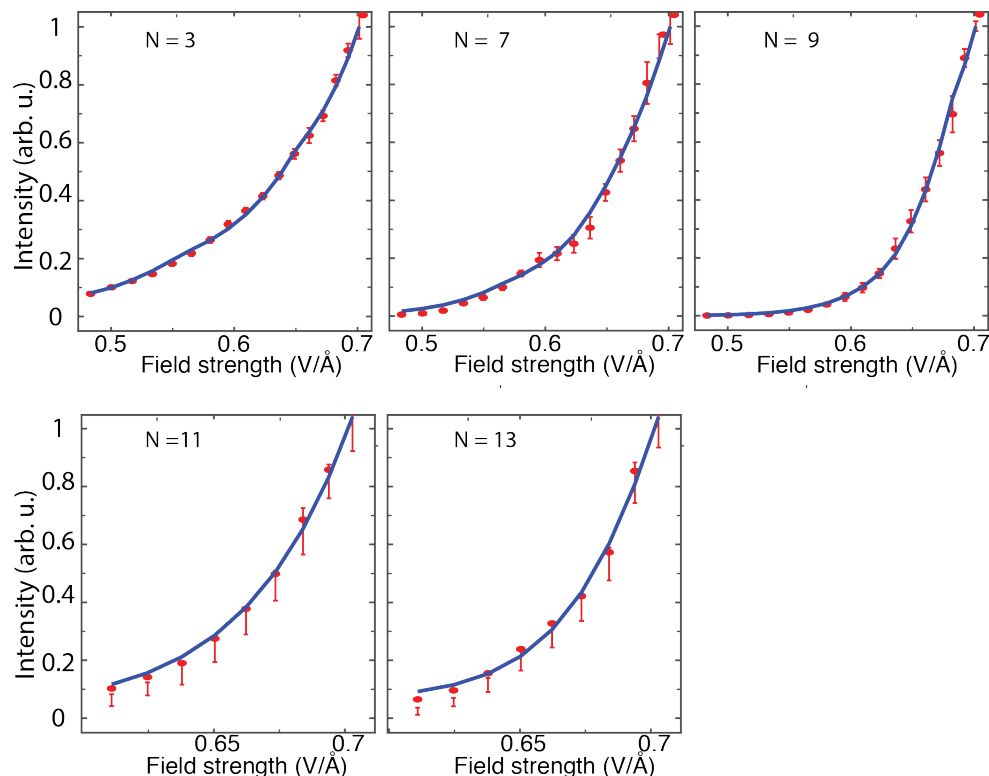


Figure 8.7: High harmonic yield versus field strength of the driving pulse aligned along the [110] direction of the crystal. The least square fitting obtained using equation 3.39 is shown in the blue curve. The Intensity yield for each harmonic order ( $N$ ) is normalized by the maximum yield.

## 8.6 Reconstructing the potential of MgF<sub>2</sub> on planes (001) and (002)

The reconstructed coefficients from [100], [110] and [120] directions of the crystal were solved using the system of linear equation to obtain the Fourier coefficients as mentioned in the section 5.2. The approach required that structure factors outside the specified radius are set to zero. The cutoff diameter of 7 was chosen and 7x7 Fourier coefficients were reconstructed. The resolution in real space is hence  $\frac{d}{2M} = 0.74 \text{ \AA}$ , where  $M$  is the highest order Fourier coefficient which is  $M = 3$  and  $d = 4.624 \text{ \AA}$  is the lattice constant. The real space image of MgF<sub>2</sub> obtained by Fourier transforming the experimentally obtained coefficients is shown in Fig. 8.9. As mentioned earlier we observe that harmonics from both the planes coherently add up, hence the summed up plane is observed in Fig. 8.2. The measured valence potential shows a weaker potential of Mg ion at the center of the unit cell surrounded by four stronger potential of F ions. The electron density is obtained by solving the Poisson equation and is presented in Fig. 8.10(a). The electronegative F ions have a higher electron density compared to the Mg ions. The weak electron density

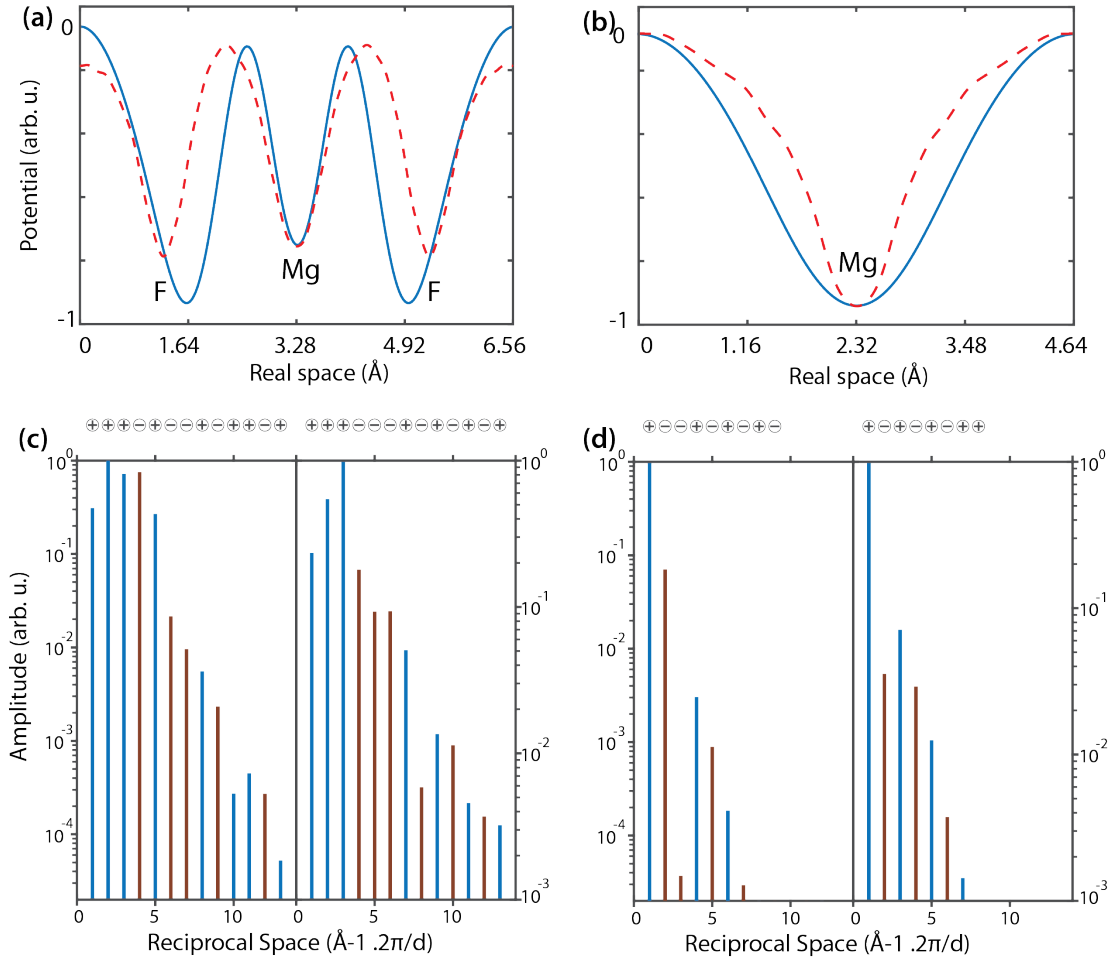


Figure 8.8: (a) 1D slice (blue) of the  $\text{MgF}_2$  potential retrieved by Fourier transforming the coefficients (c) obtained from fitting the intensity yield along  $[110]$  direction of the crystal. (b) 1D slice (blue) obtained by Fourier transforming the coefficients (d) obtained from  $[100]$  direction of the crystal. In (a),(b) experimentally retrieved slices are compared with the theoretically obtained slices (red dash) from the density functional theory (c),(d). The right column depicts experimentally obtained Fourier coefficients and the left column depicts the theoretical Fourier coefficients from DFT. They are plotted in log scale and the negative coefficients are represented by dark red.

in the interstitial space between Mg and F ions suggest the ionic character of the bonding. The potential calculated from DFT along with its electron density is also presented for comparison. They are in excellent agreement with the picometer resolution image obtained experimentally.

## 8.7 Fitting fidelity analysis

The experimentally obtained electric field from attosecond streaking measurements have an error of  $\pm 5\%$ . The stability and sensitivity of the fitting procedure to the input field strength is tested by varying the electric field by  $-20\%$  to  $20\%$ . In Fig. 8.11, panels (a),(b) and (c) show the fitting of experimental high harmonic intensity yield along  $[100]$  and  $[110]$  orientation when the electric field is changed by  $-15\%$ ,  $-5\%$  and  $0\%$  respectively. The fitting yields the best regression when the electric field is only changed by  $\pm 5\%$ . For greater variation, the regression becomes worse. The 3rd harmonic does not fit at all when the electric field is varied by more than  $-15\%$ . This can be explained by the selectivity of Bessel function on Fourier coefficients i.e. high field strengths are needed for the Bessel function to be sensitive to the lower Fourier coefficients shown previously in Fig. 4.3. The potential reconstructed along  $[110]$  and  $[100]$  direction from three fittings are shown in Fig. 8.11(d). When the electric field is changed by  $-15\%$  the Mg ions almost disappear in the reconstructed potential as shown in Fig. 8.11(e). The fitting error calculated by changing the field strength from  $-20\%$  to  $20\%$  in discrete steps of  $5\%$  is shown in panel Fig. 8.11(f). For both  $[100]$  and  $[110]$  directions the fitting error increases for more than  $\pm 5\%$  change of field strength. However, within the  $\pm 5\%$  change fitting error is low, and stable at similar value for all the fittings. Hence, the numerical fitting is stable for  $\pm 5\%$  change of field which is also the amount of error we have in the measured value of the electric field strength. This study shows that our technique has a great fidelity in reconstructing the potential of  $\text{MgF}_2$  along  $[100]$  and  $[110]$  crystal directions.

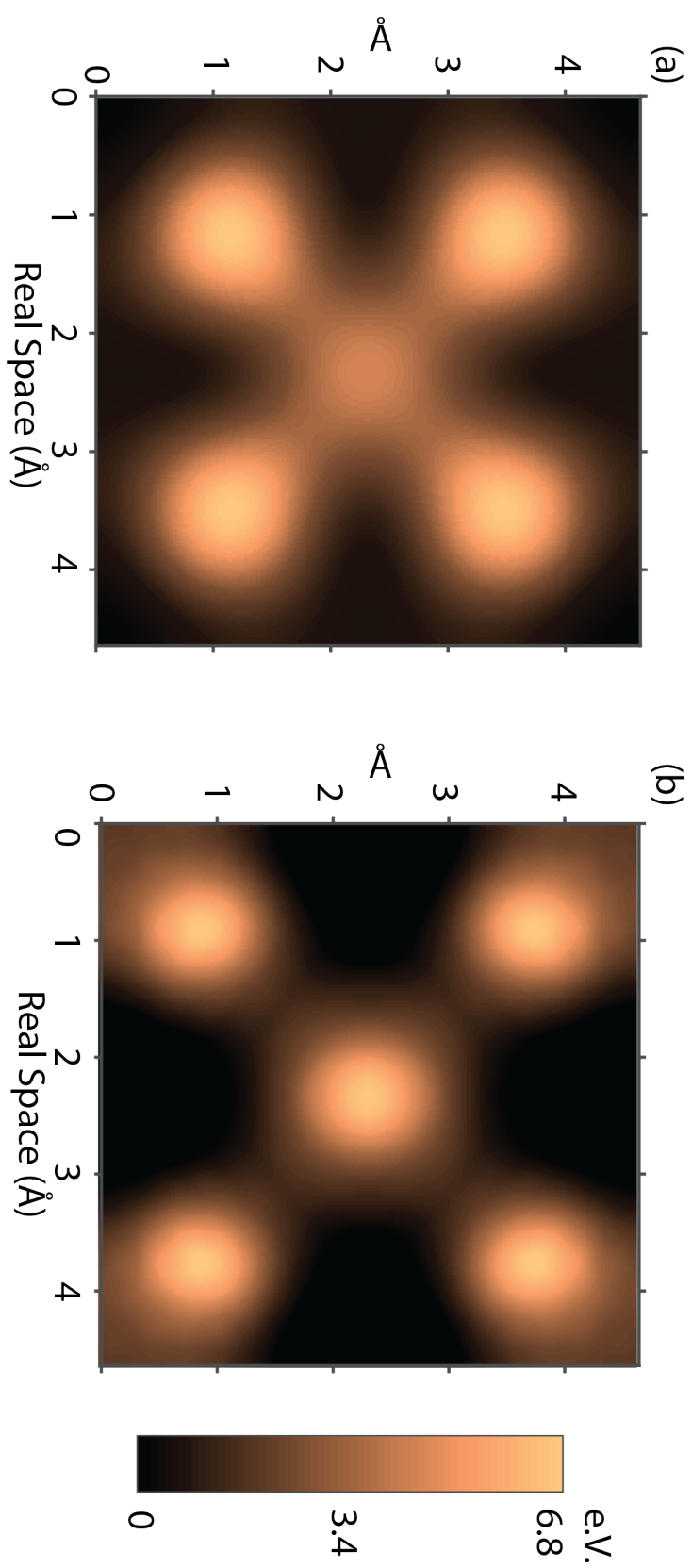


Figure 8.9: (a) Reconstructed potential of  $\text{MgF}_2$  crystal which is sum of potential on (001) plane and (002) plane (b) Effective single electron potential obtained from density functional theory calculations by summing individual potential on plane (001) and (002).

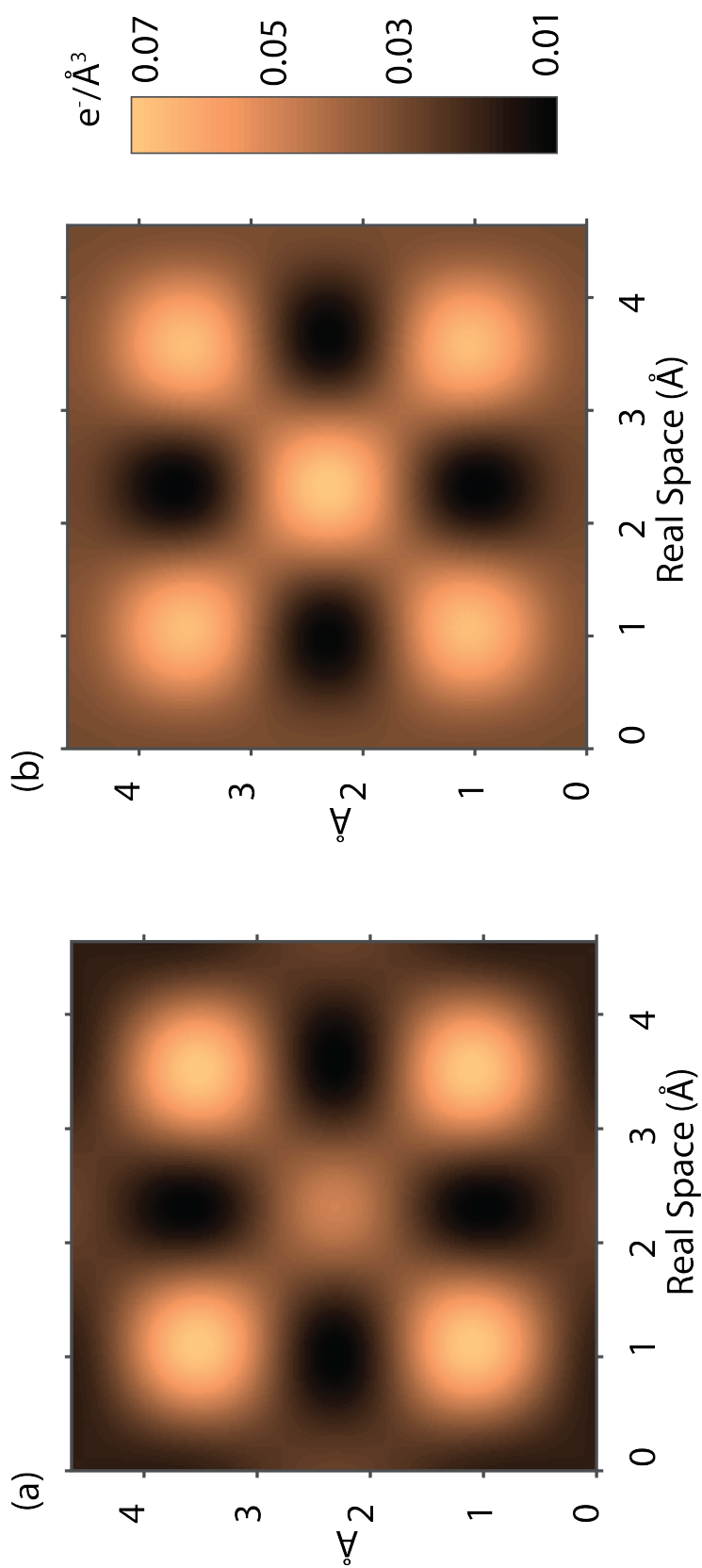


Figure 8.10: (a) Experimentally reconstructed valence electron density of MgF<sub>2</sub> crystal (b) Electron density of MgF<sub>2</sub> obtained from density functional theory.

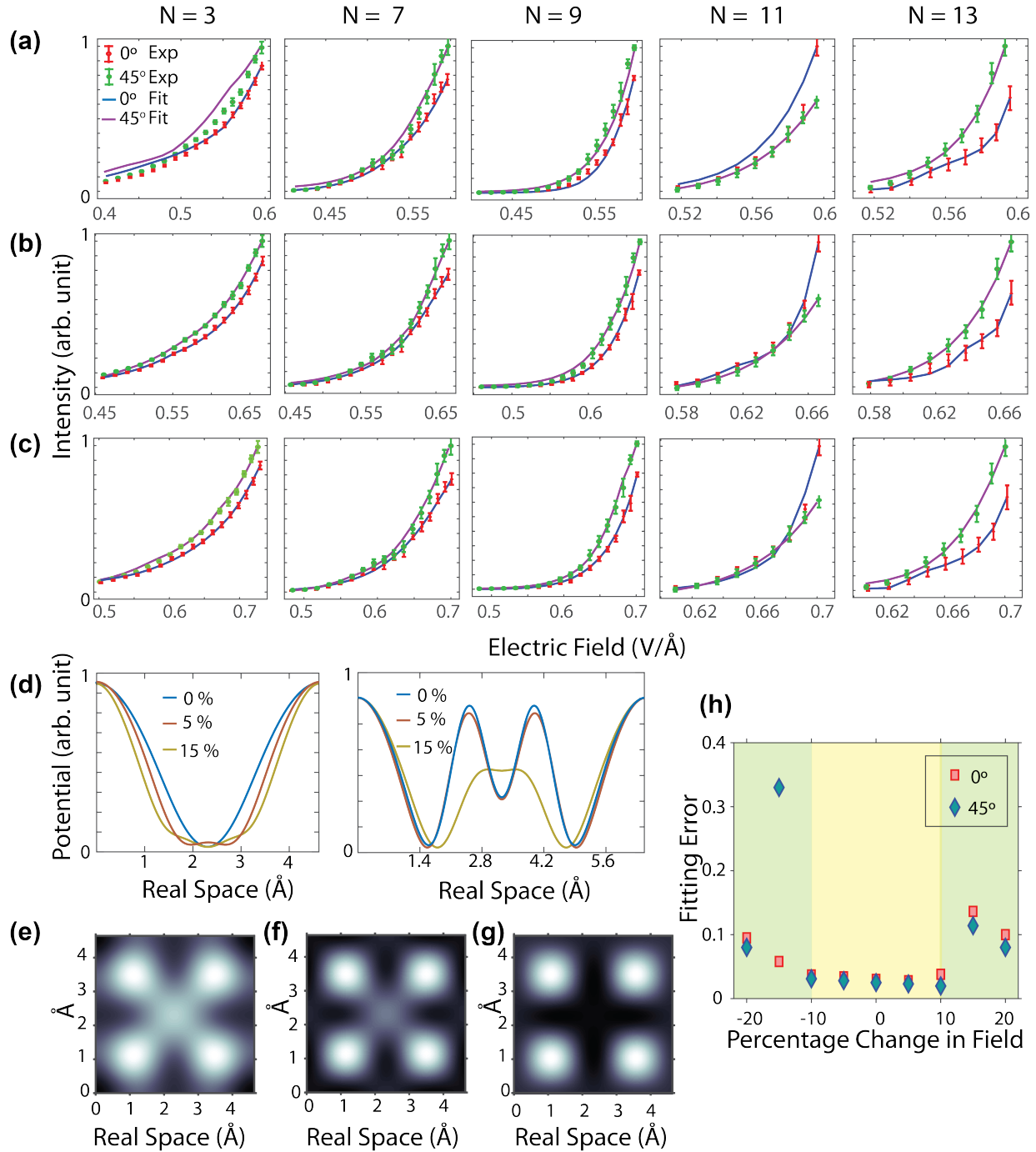


Figure 8.11: (a),(b) and (c) shows the least square fitting of intensity yield of 3<sup>rd</sup> to 13<sup>th</sup> harmonic of  $\text{MgF}_2$  for various driving field strength (red and green dots) along  $[100]$  (red solid curve) and  $[110]$  (green solid curve) orientation when the electric field is changed by -15%, -5% and 0 % respectively. (d) The potential reconstructed along  $[110]$  and  $[100]$  direction from all these 3 fittings. (e),(f),(g) The 2D potential reconstructed from the lines along  $[100]$  and  $[110]$  directions when field is changed by 0%, -5% and -15 % respectively. (h) The fitting error calculated by changing the field strength from -20% to 20 % in discrete steps of 5 % change.

# Chapter 9

## Reconstructing the valence potential of $\text{CaF}_2$

*Two are better than one*

- Every guide

To further verify the applicability of optical picoscopy to different systems, we extend our study to another crystalline material,  $\text{CaF}_2$ . It is a wide band gap material with similar chemical formula as  $\text{MgF}_2$  but has a very different lattice structure.

### 9.1 Structure of $\text{CaF}_2$

Fig. 9.1(a) shows the arrangement of atoms in a  $\text{CaF}_2$  crystal. In contrast to  $\text{MgF}_2$ ,  $\text{CaF}_2$  has Ca and F atoms on different planes when seen along  $\mathbf{c}$  axis. The symmetry point in the crystal is at the origin of the unit cell. The plane on which symmetry point exists is shaded for the reference. The line along next nearest calcium atoms (Ca-Ca) is referred to as  $[100]$  direction of the crystal which is also parallel to the conventional axis ( $\mathbf{a}, \mathbf{b}$ ). The line along the next nearest fluorine atoms (F-F) is referred to as  $[110]$  direction of the crystal. The space-filling model of the crystal is also presented alongside in Fig. 9.1(b). This shows the exact ionic radius as given by Shannon radius of the individual specimen.

### 9.2 The $\text{CaF}_2$ potential (DFT)

The valence potential of  $\text{CaF}_2$  was evaluated by a commercially available density functional theory package known as Quantumwise. The generalized gradient approximation (GGA) with Perdew-Burke-Erzerhof (PBE) functionals along with optimized norm-conserving pseudopotentials (ONCVSP) were used. The density mesh cutoff energy was kept at 75 eV and electron temperature at 300K. 270 reduced reciprocal space  $\mathbf{k}$  points were used to generate the valence potential and the valence electron density.

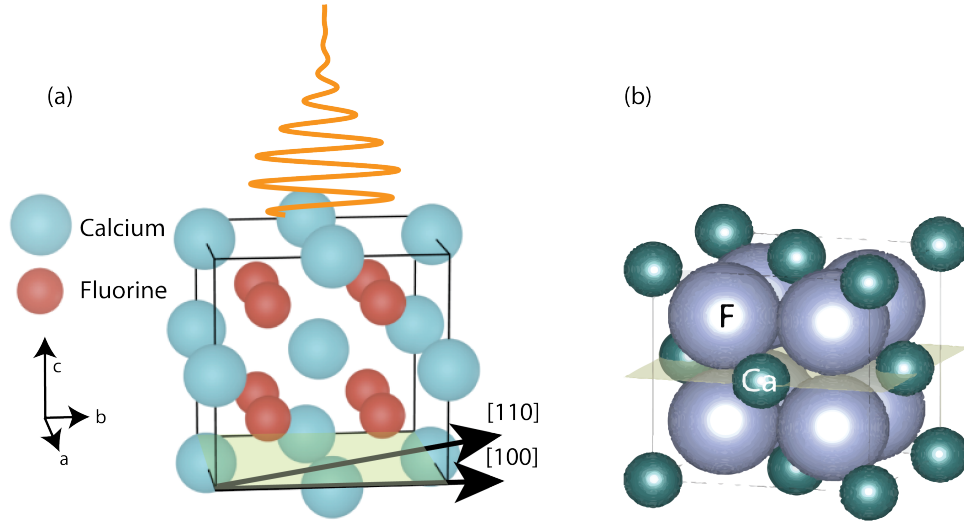


Figure 9.1: (a) Unit cell of calcium fluoride ( $\text{CaF}_2$ ) crystal. The laser pulse impinges through the  $c$  axis. The plane containing the symmetry point is shaded. (b) A space filling model of  $\text{CaF}_2$  where size of ions are based on Shannon radius.

Figure 9.2 shows the valence potential of  $\text{CaF}_2$  calculated from DFT for the plane (001) which contains the symmetry point (0,0,0). The symmetry point in  $\text{CaF}_2$  is equidistant from all the Ca atoms. In figure 9.2 this is exactly at the center of the unit cell.

### 9.3 Experiment and Analysis

Having seen the structure of  $\text{CaF}_2$  and its valence potential obtained from DFT, we now move on to reconstruct its valence potential experimentally. An approximately  $8 \mu\text{m}$  thick,  $c$ -cut  $\text{CaF}_2$  crystal was exposed to few-cycle pulses with a carrier photon energy of  $2eV$ . The harmonic signal emitting for the crystal was recorded using the spectrometer. Fig. 9.3 (a) shows the high harmonic spectra from thin  $\text{CaF}_2$  film when the driving laser field was oriented along the [100] and [110] directions of the crystal. More intense harmonics near cutoff energy were observed when the laser field was polarized along the [110] direction compared to the [100] direction of the crystal. Also, the spectral intensities of different harmonics do not maximize at the same orientation of the crystal. This may be attributed to the fact that the Fourier coefficients of the potential vary differently along the different orientations of the crystal. Fig. 9.3(b) shows the variation of intensity of emitted harmonics with increasing field strength. The spectral intensity yield of all the harmonics show a highly non-linear behaviour.

The high harmonic spectra were also recorded for the other directions of the crystal apart from the two directions mentioned above. Fig. 8.5 shows the harmonic spectra recorded for  $0^\circ$  to  $360^\circ$  rotation of the crystal with  $5^\circ$  step size at a driving field strength of  $0.7 \text{ V/\AA}$ . The  $90^\circ$  periodicity of the emitted intensity for varying crystal orientations

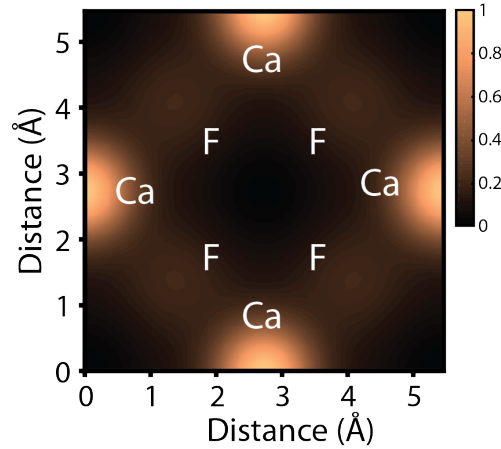


Figure 9.2: The valence potential of CaF<sub>2</sub> on the plane (001) calculated from density functional theory.

of CaF<sub>2</sub> is evident and is also in agreement with the periodicity of the crystal. Similar measurements were repeated for the various field strengths of the driving pulse until the damage threshold of the sample was reached.

## 9.4 Potential along [100] and [110] direction of CaF<sub>2</sub> crystal

The intensity dependence of recorded harmonics for various driving field strengths when the laser polarization vector is aligned along [100] and [110] orientation of the crystal is shown in Fig. 9.5 and Fig. 9.6 respectively. These plots are normalized for all the harmonics and every point in the plot is the average of 4 consecutive measurements conducted under identical experimental conditions. Using the earlier derived equation, Eq. 3.39, based on high-frequency approximation the experimental intensity dependence of high harmonics were fitted. The black line is the least square fitting of the intensity dependence data. The fitting along both [100] and [110] direction of the crystal matches precisely with the experimental data. The fitting parameters - Fourier coefficients of the potential - extracted by fitting the intensity yield in [100] and [110] direction of the crystal are shown in Fig. 9.5b and Fig. 9.6b alongside the Fourier coefficients obtained from DFT. Fourier transforming these coefficients provide us with the slice of potential along [100] and [110] direction of the crystal as shown in Fig. 9.6(c). The experimentally obtained potential is in good agreement with the valence electron potential of CaF<sub>2</sub> obtained using density functional theory. The absolute strength of the potential- zeroth order Fourier coefficient of potential- is not known experimentally so it is assumed to be of the same strength as the prediction from DFT. The valence potential along [100] direction shows the presence of only one specimen along that direction as the potential comprises of a single valley as presented in Fig. 9.6(c). This specimen is identified as a calcium ion on comparison with the potential

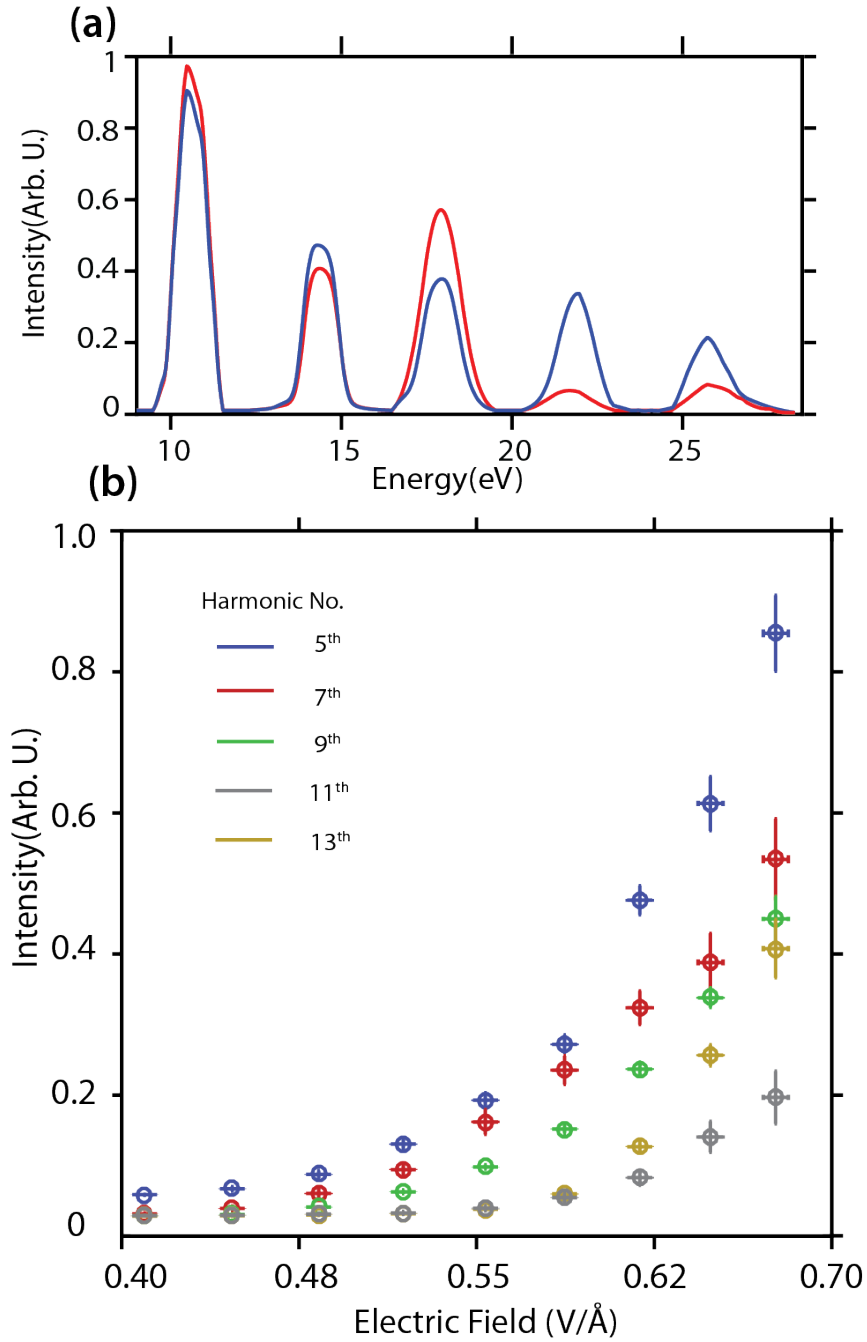


Figure 9.3: (a) High harmonic spectra of  $\text{CaF}_2$  along Ca-Ca, [100] crystal direction shown in red curve and F-F [110] crystal direction shown in blue line. (b) Intensity yield of emitted harmonics with increasing incident field strengths for 5<sup>th</sup> to 13<sup>th</sup> laser harmonic orders.

obtained from DFT. Two valleys seen along the direction [110] can be identified as  $\text{F}^-$  ions. The slices of crystal potential along two directions are enough to obtain the image of

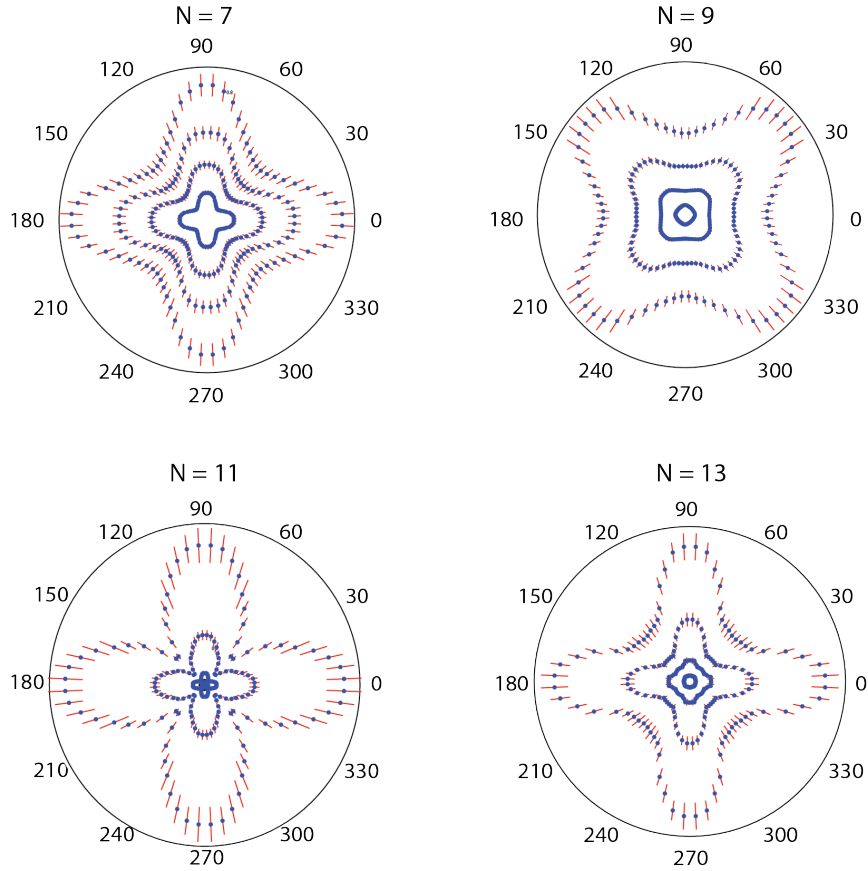


Figure 9.4: Each panel depicts the spectral intensity of emitted odd harmonics ( $N = 7$  to  $13$ ) as a function of crystal angle for 4 driving field strengths ( $0.485, 0.560, 0.615$  and  $0.650$   $\text{V}/\text{\AA}$ ). The radial direction is the intensity of emitted harmonics while azimuthal direction is the angle at which crystal is rotated.

2D valence potential of  $\text{CaF}_2$  (section 5.2).

## 9.5 Reconstruction of the potential of $\text{CaF}_2$ on (001) plane

The Fourier coefficients extracted for the slice of potential along  $[100]$  and  $[110]$  directions of the crystal were used to obtain the Fourier coefficients of the 2D slice of the potential for (001) plane as described in the section 5.2. The cutoff diameter of 7 was chosen and  $7 \times 7$  Fourier coefficients were reconstructed. The resolution of the 2D slice of the valence potential is hence  $\frac{d}{2M} = 0.91$   $\text{\AA}$  where  $M$  is the highest order Fourier coefficient which is  $M = 3$  while  $d = 5.46$   $\text{\AA}$  is the lattice constant. The reconstructed potential is depicted in panel (a) of Fig. 9.7. In the experimental potential, at the center of each side of the unit cell is a calcium ion and between two nearest calcium ion is a fluorine ion. The

calcium ion is stronger in strength and bigger in size compared to the fluorine ions, in this plane. In the ball model shown in Fig. 9.1(a), the fluorine ions are not present in this plane. However, the electron density of the fluorine ions could still be observed on this plane. This is because the radius of valence density of fluorine is ( $\sim 1.4 \text{ \AA}$ ) which is higher than the distance between the two planes ( $1.35 \text{ \AA}$ ) Fig. 9.1b. The effective potential experienced by the electrons in  $\text{CaF}_2$  as retrieved from experimental measurement matches well with the effective potential obtained from density functional theory. The sensitivity of our technique to the penetrating valence potential of  $\text{F}^-$  confirms that it observes the valence potential of the solid.

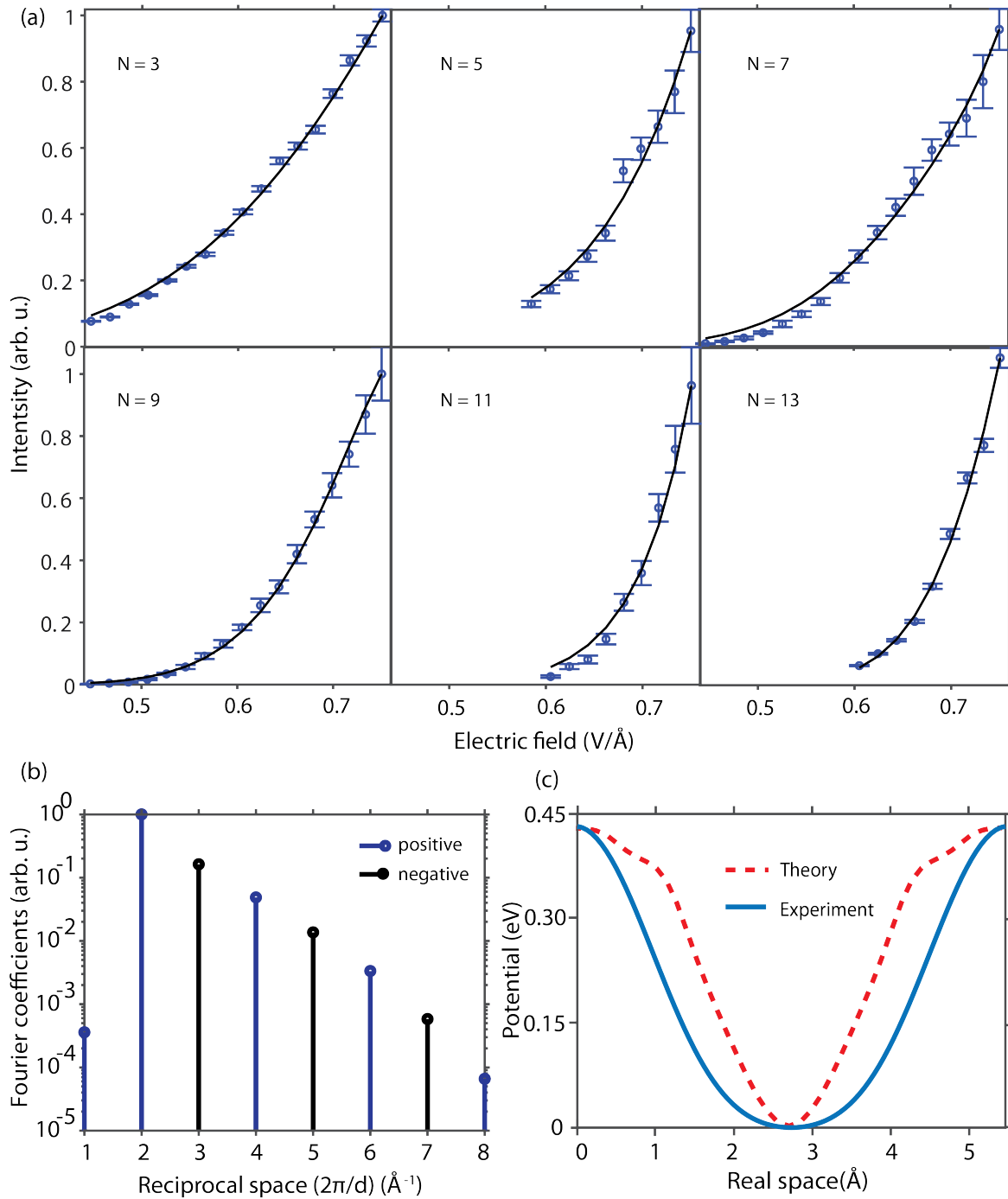


Figure 9.5: (a) The intensity of emitted harmonics as a function of increasing driving field strength along [100] direction of the crystal. The black curve is the least square fitting of the intensity yield of individual harmonic. (b) The Fourier coefficients of the periodic potential obtained by fitting the intensity yield vs electric field strength. (c) The slice of valence potential of  $\text{CaF}_2$  along [100] direction of the crystal obtained by Fourier transforming the retrieved DFT coefficients. The dashed curve represents the cross cut from the potential obtained by DFT.

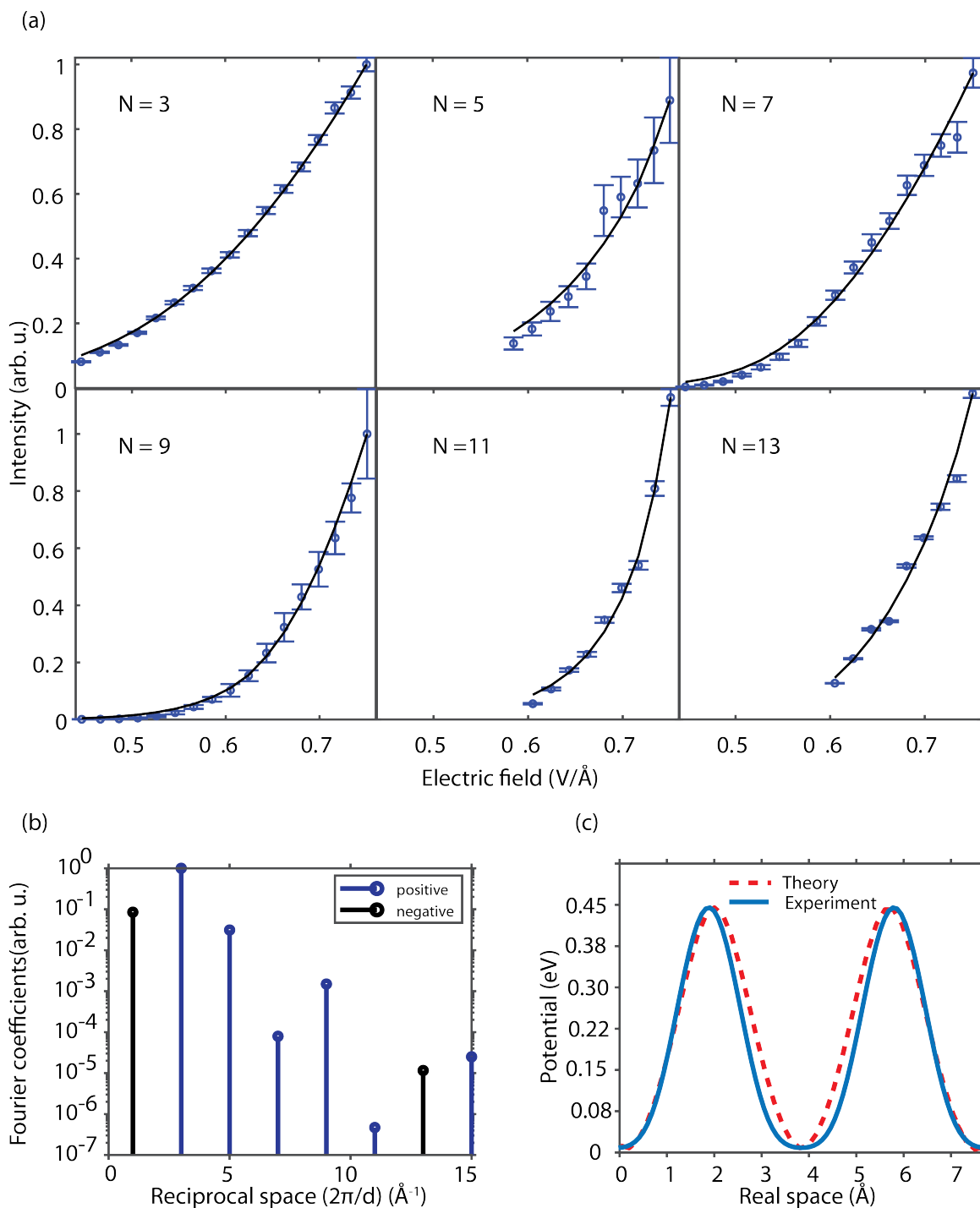


Figure 9.6: (a) The intensity of emitted harmonics versus field strength along  $[110]$  direction of crystal. The black curve is the least square fitting of the intensity yield of individual harmonic. (b) The Fourier coefficients of the periodic potential obtained by fitting the intensity yield vs electric field strength. (c) The slice of valence potential of  $\text{CaF}_2$  along  $[110]$  direction of the crystal obtained by Fourier transforming the retrieved coefficients. The dashed curve represents the cut from the potential obtained by DFT.

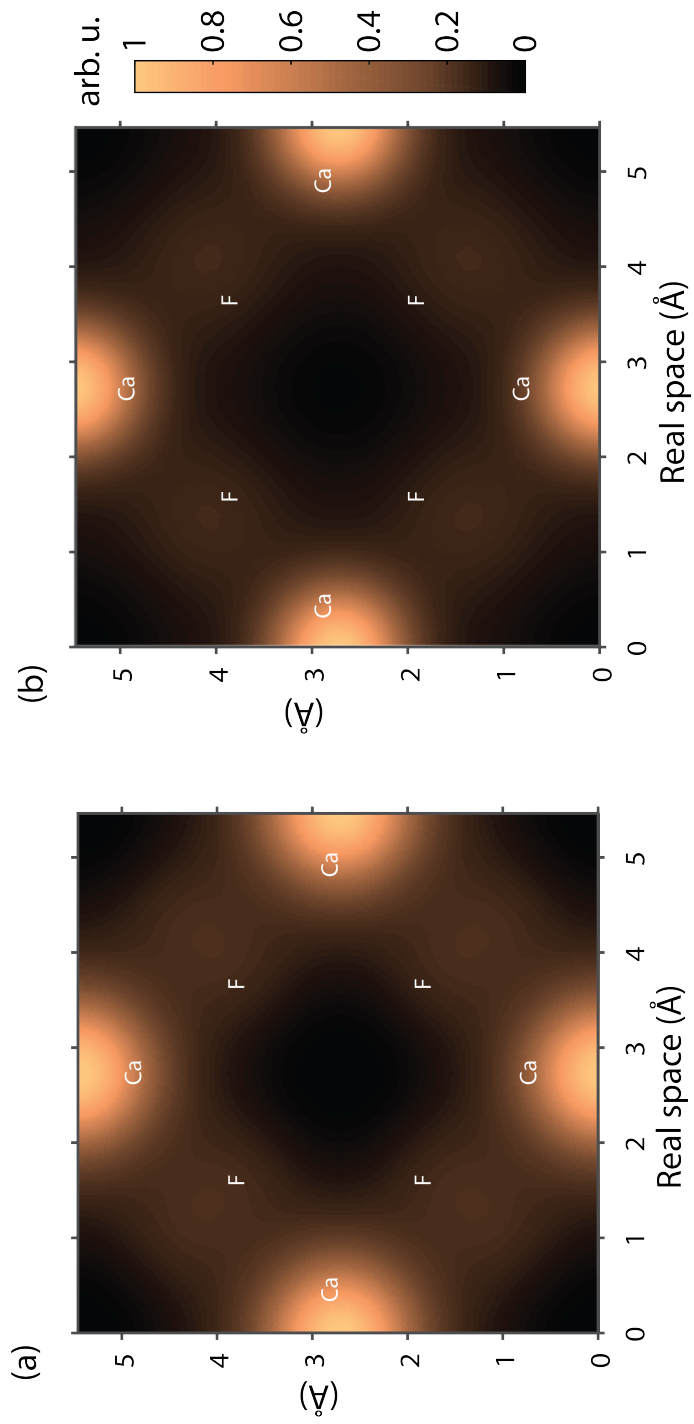


Figure 9.7: (a) Reconstructed potential of  $\text{CaF}_2$  on (001) plane of crystal. (b) Valence electron potential obtained from density functional theory.



# Chapter 10

## Conclusion and Outlook

*Set thy heart upon thy work, but never on its reward*

- The Bhagwad Gita

### 10.1 Conclusion

In this work, we showed how the high frequency approximation can be extended to solids. In this regime, where an incident pulse has photon energy higher than the inner potential energy of solids ( $\hbar\omega_L > U_{in}$ ), the velocity of valence electrons inside a crystal potential driven by a laser field follows the vector potential of the incident field. In other words, the electrons are predominantly driven by the laser field and the periodic potential only act as a perturbation to the laser motion. The first principle time dependent density functional theory (TDDFT) verified the high frequency approximation by conducting simulations of electron dynamics in MgF<sub>2</sub> crystal exposed to an intense optical pulses where the velocity of the crystal electron nearly matched the velocity of the free electron. TDDFT also attested to our intuition that the nearly free electron regime sets in when the frequency of the driving field is higher than the inner potential of the solid ( $\hbar\omega_L > U_{in}$ ).

A direct implication of the high frequency approximation was that we could use the long understood concepts of high frequency driving in atoms and solids to our exact problem of understanding HHG process in solids. Building on these concepts, we presented a semi-classical picture for explaining HHG process in solids without invoking the band picture. The high harmonic emission was found to be associated with the classical motion of an electron beginning from a symmetry point in a periodic potential of the crystal. The complete electron dynamics was found to be linked to this single trajectory of the electron. This provided us with the ability to link the intensity of emitted harmonic radiation to the periodic potential of the crystal along this trajectory.

Furthermore, the law for the cutoff energy of harmonic radiation derived using this approximation was found to be dependent on the radius of the smallest valence specimen in the crystal. The validity of high frequency approximation was experimentally established by measuring the valence radii of the smallest specimen in various systems such as MgF<sub>2</sub>,

ZnO, SiC, MgO and Diamond. This provided the first direct measurement of the ionic radii of solids. The measured radii matched well with the most widely used database for ionic radii empirically calculated by Shannon.

Having developed the theoretical toolbox, in high frequency regime, which connects the intensity of emitted harmonics to the Fourier coefficients of the potential, we set the foundation for new microscopy technique sensitive to the valence electron density of solids. We successfully established this new kind of microscope, termed as *picoscope*, and provided the first measurements of the valence electron density of MgF<sub>2</sub> and CaF<sub>2</sub> crystals with picometer resolution. The shape of the ions in MgF<sub>2</sub> and CaF<sub>2</sub> crystals were found to be non-spherical. Sharing of the electron between cationic and anionic species in the crystals were also evident from the measurement.

This paved the way for observation of valence electron density inside the crystals for the first time and opened up new avenues where dynamics of valence electrons in solids can also be probed.

## 10.2 Outlook: Picoscopy

- **NON-CENTROSYMMETRIC CRYSTAL** In the framework of this thesis, the electron density of centrosymmetric structures was imaged. Now the work is continued to also image the electron densities of the non-centrosymmetric crystal, such as quartz, where both the even and the odd harmonics are observed. The Fourier coefficients of the periodic potential of the symmetric crystal contain only the real part however for asymmetric crystals both the real and the imaginary part are present. The even harmonic is generated due to the asymmetry of the crystal and hence contain the information about the imaginary part of the crystal. Fitting the intensity yield of both even and odd harmonics with our model, the potential of the asymmetric crystal can be also obtained.
- **3D RECONSTRUCTION** The reconstruction technique is sensitive to the plane of the crystal perpendicular to the laser polarization direction. Due to this, reconstruction from a single plane of the crystal was obtained. A 3D reconstruction of a periodic potential of a valence crystal can be obtained by either revolving the crystal or using the crystals cut along different planes.
- **TIME RESOLVED OBSERVATION OF ELECTRON DENSITY** The dynamic electron density information might also be obtained using the similar techniques incorporated in a pump-probe experiment where a weak and slow pump pulse excites the dynamics in the system and a strong and fast probe pulse observe such dynamics in real time by imaging the electron density of the crystal which is stretched/bend in a controlled manner.

# Appendix A

## Semiconductor Bloch equations with coulombic interaction

A general many-body Hamiltonian in second-quantization for the electronic system neglecting the defects and the electron-phonon interactions is given as [59]

$$\begin{aligned}\hat{H} &= \hat{H}_o + \hat{H}_v + \hat{H}_{ls} \\ \hat{H} &= \sum_{\lambda, \mathbf{k}} \varepsilon_{\mathbf{k}}^{\lambda} \hat{\mathbf{a}}_{\lambda, \mathbf{k}}^{\dagger} \hat{\mathbf{a}}_{\lambda, \mathbf{k}} + \frac{1}{2} \sum_{\lambda \lambda'} \sum_{\mathbf{k}, \mathbf{k}'} \sum_{q \neq 0} \mathbf{V}_q^{\lambda \lambda'} \hat{\mathbf{a}}_{\lambda, \mathbf{k}}^{\dagger} \hat{\mathbf{a}}_{\lambda', \mathbf{k}'}^{\dagger} \hat{\mathbf{a}}_{\lambda', \mathbf{k}'+q} \hat{\mathbf{a}}_{\lambda, \mathbf{k}-q} - \mathbf{E}(t) \sum_{\lambda, \lambda' > \lambda, k} (\mathbf{d}_{\mathbf{k}}^{\lambda \lambda'} \hat{\mathbf{a}}_{\lambda, \mathbf{k}}^{\dagger} \hat{\mathbf{a}}_{\lambda', \mathbf{k}} + c.c.).\end{aligned}\tag{A.1}$$

Where  $\hat{\mathbf{a}}_{\lambda, \mathbf{k}}^{\dagger}$  and  $\hat{\mathbf{a}}_{\lambda, \mathbf{k}}$  denotes the creation and the annihilation operators for an excitation of particle with momentum  $\mathbf{k}$ . The Hamiltonian is divided into three components. The first term describes an electron in a band structure with an energy given by  $\varepsilon_{\mathbf{k}}$ . The second term describes the Coulomb interaction between electrons either in the same band or in different bands.  $\mathbf{V}_q$  are the Fourier coefficients of the real space Coulomb potential. The third term is laser-solid interaction where the electron is annihilated from one of the bands and created in other band. Only interband interactions are currently taken in the laser-solid interaction term, in the next section intraband interactions are also included. All terms except the Coulomb interaction terms have two operators. When we write the equations of motion, these operators recursively increase and end up in infinite hierarchy of coupled differential equations. In order to truncate this and obtain closed set of differential equations we make the random phase approximation i.e.  $\langle \langle \hat{\mathbf{a}}_{\lambda, \mathbf{k}}^{\dagger} \hat{\mathbf{a}}_{\lambda, \mathbf{k}'}^{\dagger} \hat{\mathbf{a}}_{\lambda, \mathbf{k}} \hat{\mathbf{a}}_{\lambda, \mathbf{k}'} \rangle \rangle \rightarrow \langle \hat{\mathbf{a}}_{\lambda, \mathbf{k}}^{\dagger} \hat{\mathbf{a}}_{\lambda, \mathbf{k}'}^{\dagger} \rangle \langle \hat{\mathbf{a}}_{\lambda, \mathbf{k}} \hat{\mathbf{a}}_{\lambda, \mathbf{k}'} \rangle - \langle \hat{\mathbf{a}}_{\lambda, \mathbf{k}}^{\dagger} \hat{\mathbf{a}}_{\lambda, \mathbf{k}} \rangle \langle \hat{\mathbf{a}}_{\lambda, \mathbf{k}'}^{\dagger} \hat{\mathbf{a}}_{\lambda, \mathbf{k}'} \rangle + \langle \hat{\mathbf{a}}_{\lambda, \mathbf{k}}^{\dagger} \hat{\mathbf{a}}_{\lambda, \mathbf{k}'} \rangle \langle \hat{\mathbf{a}}_{\lambda, \mathbf{k}'}^{\dagger} \hat{\mathbf{a}}_{\lambda, \mathbf{k}} \rangle$

The expectation value of these two operators are either population ( $f_{e,h}$ ) or polarization ( $p_{\lambda\lambda'}$ ) of electrons/holes. Specifically,  $f_e = \langle \hat{\mathbf{a}}_{e, \mathbf{k}}^{\dagger} \hat{\mathbf{a}}_{e, \mathbf{k}} \rangle$ ,  $f_h = \langle \hat{\mathbf{a}}_{h, \mathbf{k}}^{\dagger} \hat{\mathbf{a}}_{h, \mathbf{k}} \rangle$ ,  $p_{he} = \langle \hat{\mathbf{a}}_{h, \mathbf{k}}^{\dagger} \hat{\mathbf{a}}_{e, \mathbf{k}} \rangle$ ,  $p_{ee'} = \langle \hat{\mathbf{a}}_{e, \mathbf{k}}^{\dagger} \hat{\mathbf{a}}_{e', \mathbf{k}} \rangle$ ,  $p_{hh'} = \langle \hat{\mathbf{a}}_{h, \mathbf{k}}^{\dagger} \hat{\mathbf{a}}_{h', \mathbf{k}} \rangle$ , with e and h denoting electron and hole band indices. With the above approximation, the equations of motion can be described as

$$\hbar \frac{\partial f_e}{\partial t} = -2Im [\sum_{\lambda} \Omega_{e\lambda} (p_{\lambda e})^*] - \left(\frac{\hbar}{T_1}\right) f_e \quad (\text{A.2})$$

$$\hbar \frac{\partial f_h}{\partial t} = -2Im [\sum_{\lambda} \Omega_{\lambda h} (p_{h\lambda})^*] - \left(\frac{\hbar}{T_1}\right) f_h \quad (\text{A.3})$$

$$\hbar \frac{\partial p_{he}}{\partial t} = (\epsilon_e + \epsilon_h - i\hbar/T_2) p_{he} - \Omega_{eh} (1 - f_e - f_h) \quad (\text{A.4})$$

$$+ \sum_{\lambda} (\Omega_{\lambda h} p_{\lambda e} - \Omega_{e\lambda} p_{h\lambda}) \quad (\text{A.5})$$

$$\hbar \frac{\partial p_{ee'}}{\partial t} = (\epsilon_e - \epsilon_{e'} - i\hbar/T_2) p_{ee'} - \Omega_{e'e} (f_{e'} - f_e) \quad (\text{A.6})$$

$$+ \sum_{\lambda} (\Omega_{\lambda e} p_{\lambda e'} - \Omega_{e'\lambda} p_{e\lambda}) \quad (\text{A.7})$$

$$\hbar \frac{\partial p_{hh'}}{\partial t} = (\epsilon_h - \epsilon_{h'} - i\hbar/T_2) p_{hh'} - \Omega_{h'h} (f_h - f_{h'}) \quad (\text{A.8})$$

$$+ \sum_{\lambda} (\Omega_{\lambda h} p_{\lambda h'} - \Omega_{h'\lambda} p_{h\lambda}) \quad (\text{A.9})$$

Here  $\epsilon_e(k) = \varepsilon_e(k) - \sum_{q \neq k} V_{|k-q|} n_e(k)$  and  $\epsilon_h(k) = -\varepsilon_h(k) - \sum_{q=0} V_q - \sum_{q \neq k} V_{|k-q|} n_h(k)$  are the renormalized bands and  $\Omega_{\lambda\lambda'}^k = d_{\lambda\lambda'}^k E(t) + \sum_{q \neq k} V_{|k-q|} P_{\lambda\lambda'}(q)$  is the renormalized Rabi frequency.  $T_2$  is the dephasing time for polarization and  $T_1$  is the dephasing time of population. The dephasing time is the time it takes for the polarization or the population to become decoherent. This is used to take into consideration interaction of electron with phonons or other impurities.

The above equations carry the intraband term only due to Coulomb interactions. The term similar to semiclassical Bloch equation, due to the acceleration of charge carriers, is not yet included in the equation. To include the Boltzmann drift term we follow the procedure suggested in [102]. We start with the Hamiltonian of the system in the presence of laser field,  $H = \frac{1}{2m} (p - \frac{e}{c} A)^2 + V(r)$ . The eigenstates of the Hamiltonian are Volkov states  $\psi_i(r, t) = e^{\frac{ieAr}{\hbar c}} \phi_{nk}(r)$ . Since the Hamiltonian is invariant under lattice translations, the allowed values of  $k$  are:  $\frac{eA}{\hbar c} + k = \frac{n}{N} K$ , where  $N$  are the number of unit cell and  $n_i$  are integers with  $-N/2 < n < N/2$  to avoid extra redundant solutions. As  $\frac{n}{N} K$  is constant and  $A(t)$  varies with time,  $k$  must be function of time such that:

$$\frac{\partial k}{\partial t} = -\frac{e}{\hbar c} \frac{\partial A}{\partial t} = \frac{e}{\hbar} E \quad (\text{A.10})$$

Hence in the above SBE equation we must replace  $k$  with time dependent  $k(t)$  or with  $eE(t) \frac{\partial}{\partial k}$

$$\hbar \frac{\partial f_e}{\partial t} = -2Im [\sum_{\lambda} \Omega_{e\lambda} (p_{\lambda e})^*] + eE(t) \frac{\partial f_e}{\partial k} - \left(\frac{\hbar}{T_1}\right) f_e \quad (\text{A.11})$$

$$\hbar \frac{\partial f_h}{\partial t} = -2Im [\sum_{\lambda} \Omega_{\lambda h} (p_{h\lambda})^*] + eE(t) \frac{\partial f_h}{\partial k} - \left(\frac{\hbar}{T_1}\right) f_h \quad (\text{A.12})$$

$$\hbar \frac{\partial p_{he}}{\partial t} = (\epsilon_e + \epsilon_h - i\hbar/T_2) p_{he} - \Omega_{eh} (1 - f_e - f_h) \quad (\text{A.13})$$

$$+ ieE(t) \frac{\partial p_{he}}{\partial k} + \sum_{\lambda} (\Omega_{\lambda h} p_{\lambda e} - \Omega_{e\lambda} p_{h\lambda}) \quad (\text{A.14})$$

$$\hbar \frac{\partial p_{ee'}}{\partial t} = (\epsilon_e - \epsilon_{e'} - i\hbar/T_2) p_{ee'} - \Omega_{e'e} (f_{e'} - f_e) \quad (\text{A.15})$$

$$+ ieE(t) \frac{\partial p_{ee'}}{\partial k} + \sum_{\lambda} (\Omega_{\lambda e} p_{\lambda e'} - \Omega_{e'\lambda} p_{e\lambda}) \quad (\text{A.16})$$

$$\hbar \frac{\partial p_{hh'}}{\partial t} = (\epsilon_h - \epsilon_{h'} - i\hbar/T_2) p_{hh'} - \Omega_{h'h} (f_h - f_{h'}) \quad (\text{A.17})$$

$$+ ieE(t) \frac{\partial p_{hh'}}{\partial k} + \sum_{\lambda} (\Omega_{\lambda h} p_{\lambda h'} - \Omega_{h'\lambda} p_{h\lambda}) \quad (\text{A.18})$$

Now the total polarization (interband) and current (intraband) terms can be extracted as follows:

$$P(t) = \sum \lambda \lambda' k p_{\lambda \lambda'}(k) d_{\lambda \lambda'}(k) \quad (\text{A.19})$$

$$J(t) = \sum \lambda k f_{\lambda}(k) v_{g,\lambda}(k) \quad (\text{A.20})$$

The total emitted intensity is the sum of harmonics from the terms given by

$$I_{rad}(\omega) \propto |\omega P(\omega) + iJ(\omega)|^2 \quad (\text{A.21})$$



# Appendix B

## Coherent sum of equivalent planes

In this appendix we show that total observed high harmonic signal is due to the sum of high harmonics from individual plane containing symmetry points. Hence the reconstructed image is the sum of planes of the potential containing symmetry points.

A 3D potential can be written as a series of Fourier coefficients as following,

$$V(\mathbf{r}) = \int d^3\mathbf{g} \tilde{V}(\mathbf{g}) \exp(i\mathbf{g} \cdot \mathbf{r}) \quad (\text{B.1})$$

where the  $\tilde{V}(\mathbf{g})$  are Fourier coefficients of periodic potential. For simplicity, suppose that the polarization of laser is along x-direction,  $\mathbf{E}(t) = E\hat{i}$ , and electrons are initially located at  $(x_0, y_0, z_0)$ . Then, the position of electrons can be  $(x_0 + x'(t), y_0 + y'(t), z_0 + z'(t))$ . However, excursion of electrons along y and z direction is negligible compared to direction of laser polarization,  $y(t) = z(t) = 0$ . The radiation along the laser polarization can be calculated from acceleration of electrons as a function of initial position,  $\mathbf{r}_0 = (x_0, y_0, z_0)$ .

$$a_x(\mathbf{r}_0 : t) = \int d^3\mathbf{g} \tilde{V}(\mathbf{g}) i g_x \exp(i\mathbf{g} \cdot \mathbf{r}_0) \exp(i g_x x'(t)) \quad (\text{B.2})$$

Total radiation from electron acceleration is sum over all possible initial points with charge distribution,  $\rho(\mathbf{r}_0)$ .

$$E_{rad}(t) \propto \int d^3\mathbf{r}_0 \rho(\mathbf{r}_0) a_x(\mathbf{r}_0 : t) \quad (\text{B.3})$$

$$= \int d^3\mathbf{r}_0 \int d^3\mathbf{k} \tilde{\rho}(\mathbf{k}) \exp(i\mathbf{k} \cdot \mathbf{r}_0) \int d^3\mathbf{g} \tilde{V}(\mathbf{g}) i g_x \exp(i\mathbf{g} \cdot \mathbf{r}_0) \exp(i g_x x'(t)) \quad (\text{B.4})$$

$$= \int d^3\mathbf{k} \tilde{\rho}_k(\mathbf{k}) \int d^3\mathbf{g} \tilde{V}(\mathbf{g}) i g_x \exp(i g_x x'(t)) \int d^3\mathbf{r}_0 \exp(i\mathbf{g} \cdot \mathbf{r}_0) \exp(i\mathbf{k} \cdot \mathbf{r}_0) \quad (\text{B.5})$$

$$= \int d^3\mathbf{g} \tilde{\rho}(-\mathbf{g}) \tilde{V}(\mathbf{g}) i g_x \exp(i g_x x'(t)) \quad (\text{B.6})$$

$$= \int dg_x i g_x \left[ \int dg_y dg_z \tilde{V}(\mathbf{g}) \tilde{\rho}(-\mathbf{g}) \right] \exp(i g_x x'(t)) \quad (\text{B.7})$$

The radiation of N-th harmonic is Fourier transform of acceleration with respect to time as following

$$I_N(\mathbf{E}, \omega_L) \propto \left| \int dg_x g_x U_{proj}(g_x) J_n \left( \frac{eg_x E}{m_e \omega_L^2} \right) \right|^2 \quad (\text{B.8})$$

where  $U_{proj}(k_x)$  is defined as

$$U_{proj}(g_x) = \int dg_y dg_z \tilde{\rho}(-\mathbf{g}) \tilde{V}(\mathbf{g}) \quad (\text{B.9})$$

By the convention of crystallography above equation can be written with the Miller indices where  $\mathbf{g} = \frac{2\pi}{d}(h\hat{i} + k\hat{j} + l\hat{k})$ .

$$I_N(\mathbf{E}, \omega_L) \propto \left| \sum_h h U_h J_n \left( h \frac{ekE}{m_e \omega_L^2} \right) \right|^2 \quad (\text{B.10})$$

$$U_h = \sum_{k,l} \tilde{\rho}_{\bar{h}\bar{k}\bar{l}} \tilde{V}_{hkl} \quad (\text{B.11})$$

#### Case: $MgF_2$ structure (Rutile Structure)

Since crystal structure can be decomposed into basis and lattice and total periodic potential in real space is convolution of them.

$$V(\mathbf{r}) = f(\mathbf{r}) \otimes l(\mathbf{r}) \quad (\text{B.12})$$

where  $f(\mathbf{r})$  and  $l(\mathbf{r})$  refer to potential of basis and lattice function respectively. The lattice function,  $l(\mathbf{r})$ , is described as a comb function. In the Fourier space, convolution can be simply written as a multiplication of two function.

$$\tilde{V}(\mathbf{g}) = \tilde{f}(\mathbf{g}) \tilde{l}(\mathbf{g}) \quad (\text{B.13})$$

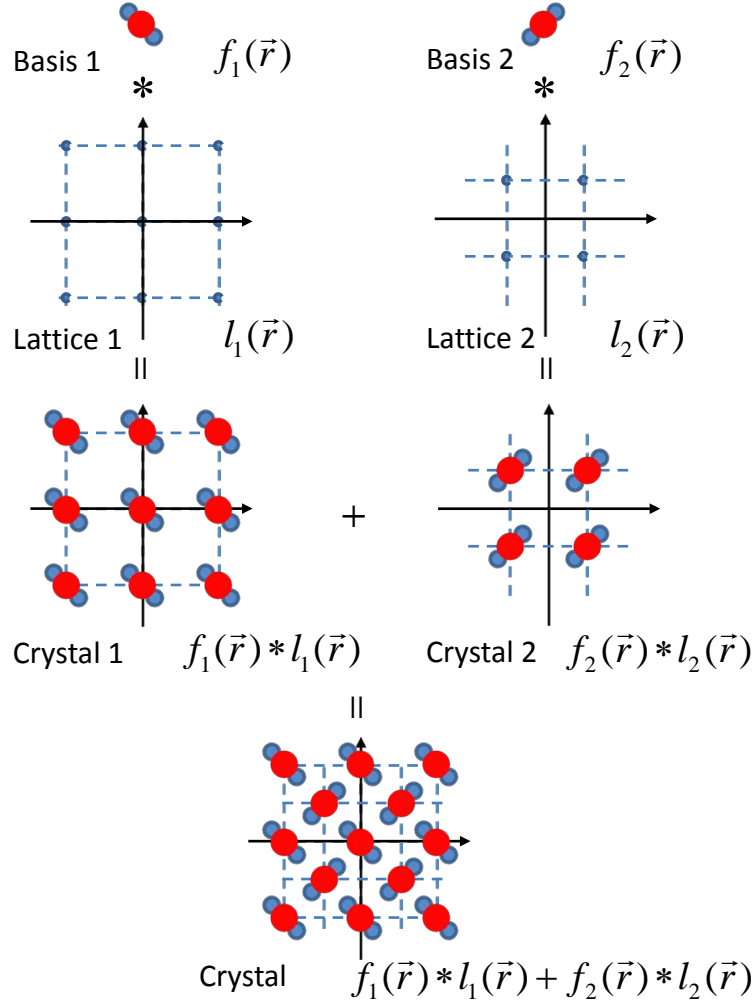
It is valid for all kind of crystal structures. Crystalline  $MgF_2$  consists of two same cuboid lattice structures [d, d, d'], (lattice 1 and 2) but spatially separated by [d/2, d/2, d'/2], and two different bases, one and 90deg rotated with respect to the other, (basis 1 and 2). Basis 1 and 2 are located at each point of lattice 1 and 2, respectively.

$$\tilde{V}_1(\mathbf{g}) = \tilde{f}_1(\mathbf{g}) \tilde{l}_1(\mathbf{g}) \quad (\text{B.14})$$

$$\tilde{V}_2(\mathbf{g}) = \tilde{f}_2(\mathbf{g}) \tilde{l}_2(\mathbf{g}) \quad (\text{B.15})$$

$$\tilde{V}(\mathbf{g}) = \tilde{V}_1(\mathbf{g}) + \tilde{V}_2(\mathbf{g}) \quad (\text{B.16})$$

Spatial separation creates phase difference between two lattices. From now the conven-

Figure B.1: **Construction of  $MgF_2$  crystal**

tion of Miller indices is used.

$$\tilde{l}_2(hkl) = \tilde{l}_1(hkl) \exp(i\pi(h + k + l)) \quad (\text{B.17})$$

Then, the Eq. B.16 is rewritten as

$$\tilde{V}(hkl) = \tilde{f}_1(hkl)\tilde{l}_1(hkl) + \tilde{f}_2(hkl)\tilde{l}_1(hkl) \exp(i\pi(h + k + l)) \quad (\text{B.18})$$

$$= \tilde{l}_1(hkl)[\tilde{f}_1(hkl) + \tilde{f}_2(hkl) \exp(i\pi(h + k + l))] \quad (\text{B.19})$$

Supposing that one basis or one  $MgF_2$  molecule provides one trajectory of electron, a

charge or trajectory density at initial position,  $\mathbf{r}_0$  is defined as the lattice function.

$$\tilde{\rho}(hkl) = \tilde{l}_1(hkl) + \tilde{l}_2(hkl) = \tilde{l}_1(hkl)(1 + \exp(i\pi(h + k + l))) \quad (\text{B.20})$$

Substitution of Eq. B.18 and Eq. B.20 into Eq.B.11 gives

$$U_h = \sum_{k,l} \tilde{\rho}_{\bar{h}\bar{k}\bar{l}} \tilde{V}_{hkl} \quad (\text{B.21})$$

$$= \sum_{k,l} \tilde{l}_1(hkl) \tilde{l}_1(\bar{h}\bar{k}\bar{l}) [1 + \exp(-i\pi(h + k + l))] [\tilde{f}_1(hkl) + \tilde{f}_2(hkl) \exp(i\pi(h + k + l))] \quad (\text{B.22})$$

$$= \sum_{k,l} \tilde{l}_1(hkl) \tilde{l}_1(\bar{h}\bar{k}\bar{l}) [\tilde{f}_1(hkl) + \tilde{f}_2(hkl)] [1 + \cos(\pi(h + k + l))] \quad (\text{B.23})$$

If coordinate is chosen such that lattice 1 is centered at 0, the lattice function,  $\tilde{l}_1(hkl)$  is a centrosymmetric comb function with uniform phase. It implies,  $\tilde{l}_1(\bar{h}\bar{k}\bar{l}) = \tilde{l}_1(hkl)$  and  $(\tilde{l}_1(hkl))^2 = \alpha \tilde{l}_1(hkl)$ , where  $\alpha$  is a constant. Then, the final result is

$$U_h = \alpha \sum_{k,l} \tilde{l}_1(hkl) [\tilde{f}_1(hkl) + \tilde{f}_2(hkl)] [1 + \cos(\pi(h + k + l))] \quad (\text{B.24})$$

$$= \alpha \sum_{k,l} [\tilde{f}_1(hkl) + \tilde{f}_2(hkl)] [\tilde{l}_1(hkl) + \tilde{l}_2(hkl)] \quad (\text{B.25})$$

This result is equivalent to the result of one trajectory with double lattice and superposition of two bases,  $\rho'(hkl) = \text{const}$  and  $\tilde{V}' = [\tilde{f}_1(hkl) + \tilde{f}_2(hkl)] [\tilde{l}_1(hkl) + \tilde{l}_2(hkl)]$ .

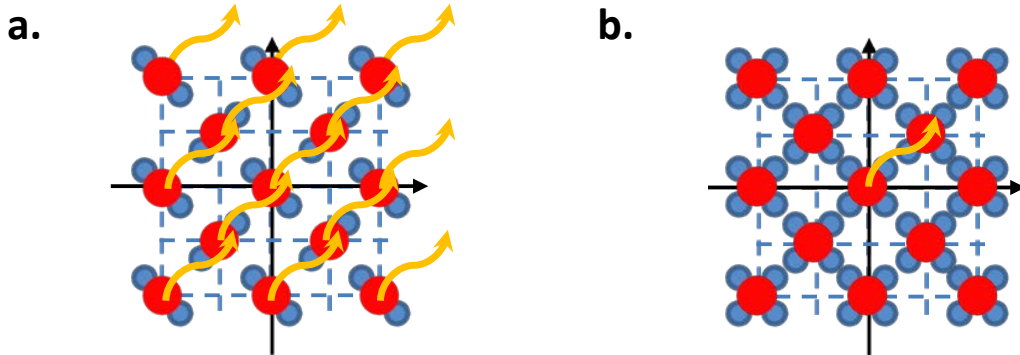


Figure B.2: **Radiation from  $MgF_2$  crystal** Radiation from  $MgF_2$  or rutile crystal, coherent sum from all bases (a), is equivalent to radiation from a single superimposed basis (b).

# Appendix C

## Calculating harmonic current from time dependent density functional theory

### Calculation Method

The TDDFT calculations were performed for the rutile-type  $\text{MgF}_2$  unit cell ( $P4_2/mnm$ ) [83]. Initially, density functional theory (DFT) was performed with the Quantum ESPRESSO package (QE) to obtain the ground state properties, using a norm-conserving (NC) pseudopotential in conjunction with the Perdew–Burke–Ernzerhof (PBE) functional [84] and plane-wave (PW) basis set with energy cutoff at 400 eV. The energy and forces convergence threshold for ionic minimization were kept at  $10^{-4}$  (a.u) and  $10^{-3}$  (a.u) respectively. The energy convergence threshold for self-consistent calculations was  $10^{-6}$  (a.u). In the ground state calculation we used  $12 \times 12 \times 24$  k-points sampling and obtained a direct band gap is of about 7 eV (10.8 eV in experiment)

### Excited state dynamics

The excited-state simulations were performed with real-time time dependent density functional theory (TDDFT). We start the calculation by adding the laser-matter interaction term in the Hamiltonian to simulate the external laser field:

$$\hat{H} = \frac{1}{2m}(\hbar\hat{k} - \frac{e}{c}A\hat{t})^2 + \hat{V}, \quad (\text{C.1})$$

where  $m$  is the electron mass,  $k$  is the electron momentum and  $V$  is the periodic lattice potential of the crystal. In velocity gauge the time-dependent vector field  $A(t)$  can be written as the integral of electric field  $E(t)$ :

$$A(t) = -\frac{e}{\hbar} \int E(t)dt. \quad (\text{C.2})$$

With the time-dependent Hamiltonian, time-dependent Kohn-Sham equation (TDKS)  $i\hbar\frac{\partial\psi}{\partial t} = \hat{H}\psi$  is solved to simulate the excitation process.[85] To save computational time and maintain accuracy, we made use of L-W Wang's algorithm[103, 104] and expressed the propagator operator within the Crank-Nicholson scheme[105, 85]. Then the TDKS orbitals  $\psi_{l,G,k,\sigma}(t)$  as well as time dependent charge density  $\rho(t)$  were available. The population  $n_{i,G,k,\sigma}(t)$  and induced current density  $j_{G,k,\sigma}(t)$  were obtained by expanding the TDKS orbital in the adiabatic basis  $\phi_{i,G,k,\sigma}(t)$ :

$$n_{i,G,k,\sigma}(t) = \sum_l |c_{il,G,k,\sigma}(t)|^2, \quad (C.3)$$

$$j_{G,k,\sigma}(t) = \frac{e\hbar}{m} \sum_i n_{i,G,k,\sigma}(t) \Re[\phi_{i,G,k,\sigma}(t)^* \nabla \phi_{i,G,k,\sigma}(t)]. \quad (C.4)$$

where  $\psi(t)_{l,G,k,\sigma} = \sum_i c_{il,G,k,\sigma}(t) \phi_{i,G,k,\sigma}(t)$ . The labels  $i, l$  denote band index and  $G, k, \sigma$  are the PW basis index, K points and spin index, respectively.  $c_{il,G,k,\sigma}$  is the coefficient in adiabatic basis. At  $t = 0$  fs,  $c_{il,G,k,\sigma} = \delta_{il,G,k,\sigma}$ . Summing up  $j(t)$  we obtain the overall current as:

$$I(t) = \sum_{G,k,\sigma} j_{G,k,\sigma}(t). \quad (C.5)$$

Being interested mainly in the microscopic dynamics of HHG, the macroscopic propagation and screening effects were neglected. This approximation can be reasonable as previous works have described[72].

Using the current expression for the HHG spectra, namely,  $\text{HHG}(\omega) \propto \omega^2 |\text{FT}[I(t)]|^2$ , we can obtain the spectra of different harmonics.

In calculations we considered a laser pulse with:

$$E(t) = \frac{E_0}{e^{(t-t_0)/\tau} + e^{-(t-t_0)/\tau}} \cos(2\pi\omega(t - t_0) + \phi), \quad (C.6)$$

being the envelope, where  $\tau = 3.63$  fs. The pulse duration is about 50 fs and the pulse center is located at 25 fs. The carrier wavelength  $\lambda$  ranges between 400-800 nm, corresponding to the photon energy of 3.1 to 0.41 eV. The electric field peak ranges from 0.43 V/Å to 0.7 V/Å. Correspondingly, the peak intensity inside matter takes value from  $1.47 \times 10^{12}$  to  $3.41 \times 10^{12}$  W/cm<sup>2</sup>. These pulse parameters are identical with those from the experiment.

Given the primary convenience for plane wave (PW) to deal with gradient in reciprocal space, simulations were performed using a homemade time dependent plane wave(TDPW) package with PW basis to obtain the induced current. We used a norm-conserving pseudopotential with the PBE functional[84] and the PW basis energy cutoff of 400 eV. The k-point sampling was  $6 \times 6 \times 9$ . To make the MgF<sub>2</sub> DFT band gap real, we applied a scissor correction[72]  $\Delta = 3.8$  eV by artificially shifting the conduction bands to higher energy. The evolution of excited states was achieved by an electron density self-consistently propagating at every electronic step of 0.0483 fs. After a 1040 steps of evolution, we get a direct microscopic picture on the electron dynamics.

# Appendix D

## Projection-slice theorem

The projection-slice theorem in 2D states that, the Fourier transform of the projection of 2D function in 1D is equal to the 1D slice of 2D Fourier transform of that function through the origin of the Fourier transform. This statement can be trivially generalized to higher dimensions. We present the proof in 2D dimension. Without loss of generality the projection axis can be chosen to be  $k_x$  axis. If  $F(k_x, k_y)$  is a 2D function, then projection onto  $k_x$  axis is given by

$$p(k_x) = \int_{-\infty}^{\infty} F(k_x, k_y) dk_y \quad (\text{D.1})$$

The Fourier transform of  $F(k_x, k_y)$  is

$$f(x, y) = \int_{-\infty}^{\infty} \int_{-\infty}^{\infty} F(k_x, k_y) e^{-2\pi i(k_x x + k_y y)} dk_y dk_x \quad (\text{D.2})$$

The slice is then  $s(x)$

$$s(x) = f(x, 0) = \int_{-\infty}^{\infty} \int_{-\infty}^{\infty} F(k_x, k_y) e^{-2i\pi x k_x} dk_y dk_x \quad (\text{D.3})$$

$$= \int_{-\infty}^{\infty} \left[ \int_{-\infty}^{\infty} F(k_x, k_y) dk_y \right] e^{-2i\pi x k_x} dk_x \quad (\text{D.4})$$

$$= \int_{-\infty}^{\infty} p(k_x) e^{-2i\pi x k_x} dk_x \quad (\text{D.5})$$

$$(\text{D.6})$$

which is just the Fourier transform of  $p(k_x)$ .



# Bibliography

- [1] J. J. Thomson, “Cathode Rays,” *Philosophical Magazine*, vol. 44, pp. 293–316, 1897.
- [2] E. Rutherford, “The Scattering of  $\alpha$  and  $\beta$  Particles by Matter and the Structure of the Atom,” *Philosophical Magazine*, vol. 21, no. 6, pp. 669–668, 1911.
- [3] P. Drude, “Zur Elektronentheorie der Metalle,” *Annalen der Physik*, vol. 306, pp. 566–613, jan 1900.
- [4] M. Hentschel, R. Kienberger, C. Spielmann, G. a. Reider, N. Milosevic, T. Brabec, P. Corkum, U. Heinzmann, M. Drescher, and F. Krausz, “Attosecond metrology,” *Nature*, vol. 414, pp. 509–513, 2001.
- [5] Y. Silberberg, “Physics at the attosecond frontier,” *Nature*, vol. 414, pp. 494–495, nov 2001.
- [6] P. M. Paul, E. S. Toma, P. Breger, G. Mullot, F. Auge, P. Balcou, H. G. Muller, and P. Agostini, “Observation of a train of attosecond pulses from high harmonic generation,” *Science (New York, N.Y.)*, vol. 292, pp. 1689–92, jun 2001.
- [7] M. Drescher, M. Hentschel, R. Kienberger, M. Uiberacker, V. Yakovlev, A. Scrinzi, T. Westerwalbesloh, U. Kleineberg, U. Heinzmann, and F. Krausz, “Time-resolved atomic inner-shell spectroscopy,” *Nature*, vol. 419, no. 6909, pp. 803–807, 2002.
- [8] A. Baltuška, T. Udem, M. Uiberacker, M. Hentschel, E. Goulielmakis, C. Gohle, R. Holzwarth, V. S. Yakovlev, A. Scrinzi, T. W. Hänsch, and F. Krausz, “Attosecond control of electronic processes by intense light fields,” *Nature*, vol. 421, pp. 611–615, 2003.
- [9] J. Itatani, J. Levesque, D. Zeidler, H. Niikura, H. Pépin, J. C. Kieffer, P. B. Corkum, and D. M. Villeneuve, “Tomographic imaging of molecular orbitals,” *Nature*, vol. 432, no. December, pp. 867–871, 2004.
- [10] M. Uiberacker, T. Uphues, M. Schultze, A. J. Verhoef, V. Yakovlev, M. F. Kling, J. Rauschenberger, N. M. Kabachnik, H. Schröder, M. Lezius, K. L. Kompa, H.-G. Muller, M. J. J. Vrakking, S. Hendel, U. Kleineberg, U. Heinzmann, M. Drescher, and F. Krausz, “Attosecond real-time observation of electron tunnelling in atoms,” *Nature*, vol. 446, pp. 627–632, apr 2007.

- [11] A. L. Cavalieri, N. Müller, T. Uphues, V. S. Yakovlev, A. Baltuska, B. Horvath, B. Schmidt, L. Blümel, R. Holzwarth, S. Hendel, M. Drescher, U. Kleineberg, P. M. Echenique, R. Kienberger, F. Krausz, and U. Heinzmann, “Attosecond spectroscopy in condensed matter.,” *Nature*, vol. 449, pp. 1029–32, oct 2007.
- [12] E. Goulielmakis, M. Uiberacker, R. Kienberger, A. Baltuska, V. Yakovlev, A. Scrinzi, T. Westerwalbesloh, U. Kleineberg, U. Heinzmann, M. Drescher, and F. Krausz, “Direct measurement of light waves.,” *Science (New York, N.Y.)*, vol. 305, pp. 1267–9, aug 2004.
- [13] M. Schultze, M. Fiess, N. Karpowicz, J. Gagnon, M. Korbman, M. Hofstetter, S. Neppl, A. L. Cavalieri, Y. Komninos, T. Mercouris, C. A. Nicolaides, R. Pazourek, S. Nagele, J. Feist, J. Burgdörfer, A. M. Azzeer, R. Ernstorfer, R. Kienberger, U. Kleineberg, E. Goulielmakis, F. Krausz, and V. S. Yakovlev, “Delay in photoemission.,” *Science (New York, N.Y.)*, vol. 328, pp. 1658–62, jun 2010.
- [14] E. Goulielmakis, Z.-H. Loh, A. Wirth, R. Santra, N. Rohringer, V. S. Yakovlev, S. Zherebtsov, T. Pfeifer, A. M. Azzeer, M. F. Kling, S. R. Leone, and F. Krausz, “Real-time observation of valence electron motion.,” *Nature*, vol. 466, pp. 739–743, 2010.
- [15] M. T. Hassan, T. T. Luu, A. Moulet, O. Raskazovskaya, P. Zhokhov, M. Garg, N. Karpowicz, A. M. Zheltikov, V. Pervak, F. Krausz, and E. Goulielmakis, “Optical attosecond pulses and tracking the nonlinear response of bound electrons,” *Nature*, vol. 530, pp. 66–70, feb 2016.
- [16] S. Ghimire, A. D. DiChiara, E. Sistrunk, P. Agostini, L. F. DiMauro, and D. A. Reis, “Observation of high-order harmonic generation in a bulk crystal,” 2011.
- [17] O. Schubert, M. Hohenleutner, F. Langer, B. Urbanek, C. Lange, U. Huttner, D. Golde, T. Meier, M. Kira, S. W. Koch, and R. Huber, “Sub-cycle control of terahertz high-harmonic generation by dynamical Bloch oscillations,” *Nature Photonics*, vol. 8, no. January, pp. 119–123, 2014.
- [18] G. Vampa, T. J. Hammond, N. Thire, B. E. Schmidt, F. Legare, C. R. McDonald, T. Brabec, D. D. Klug, and P. B. Corkum, “All-Optical Reconstruction of Crystal Band Structure,” *Physical Review Letters*, vol. 115, no. November, pp. 1–5, 2015.
- [19] T. T. Luu, M. Garg, S. Y. Kruchinin, a. Moulet, M. T. Hassan, and E. Goulielmakis, “Extreme ultraviolet high-harmonic spectroscopy of solids.,” *Nature*, vol. 521, pp. 498–502, 2015.
- [20] M. Hohenleutner, F. Langer, O. Schubert, M. Knorr, U. Huttner, S. W. Koch, M. Kira, and R. Huber, “Real-time observation of interfering crystal electrons in high-harmonic generation.,” *Nature*, vol. 523, pp. 572–5, 2015.

- [21] G. Vampa, T. J. Hammond, N. Thire, B. E. Schmidt, F. Legare, C. R. McDonald, T. Brabec, and P. B. Corkum, “Linking high harmonics from gases and solids,” *Nature*, vol. 522, pp. 462–464, 2015.
- [22] Y. S. You, M. Wu, Y. Yin, A. Chew, X. Ren, S. Gholam-Mirzaei, D. A. Browne, M. Chini, Z. Chang, K. J. Schafer, M. B. Gaarde, and S. Ghimire, “Laser waveform control of extreme ultraviolet high harmonics from solids,” *Optics Letters*, vol. 42, no. 9, p. 1816, 2017.
- [23] X. Liu, X. Zhu, P. Lan, X. Zhang, D. Wang, Q. Zhang, and P. Lu, “Time-dependent population imaging for high-order-harmonic generation in solids,” *Physical Review A*, vol. 95, no. 6, pp. 1–10, 2017.
- [24] F. Langer, M. Hohenleutner, U. Huttner, S. W. Koch, M. Kira, and R. Huber, “Symmetry-controlled temporal structure of high-harmonic carrier fields from a bulk crystal,” *Nature Photonics*, no. March, pp. 1–6, 2017.
- [25] S. Han, H. Kim, Y. W. Kim, Y.-J. Kim, S. Kim, I.-Y. Park, and S.-W. Kim, “High-harmonic generation by field enhanced femtosecond pulses in metal-sapphire nanostructure,” *Nature Communications*, vol. 7, no. May, p. 13105, 2016.
- [26] M. Kira and S. W. S. W. Koch, *Semiconductor quantum optics*. Cambridge University Press, 2012.
- [27] M. Wu, S. Ghimire, D. a. Reis, K. J. Schafer, and M. B. Gaarde, “High-harmonic generation from Bloch electrons in solids,” *Physical Review A - Atomic, Molecular, and Optical Physics*, vol. 91, pp. 1–11, 2015.
- [28] M. Garg, M. Zhan, T. T. Luu, H. Lakhotia, T. Klostermann, A. Guggenmos, and E. Goulielmakis, “Multi-petahertz electronic metrology,” *Nature*, vol. 538, no. 7625, pp. 359–363, 2016.
- [29] S. Y. Kruchinin, F. Krausz, and V. S. Yakovlev, “<i>Colloquium</i> : Strong-field phenomena in periodic systems,” *Reviews of Modern Physics*, vol. 90, p. 021002, apr 2018.
- [30] A. Klug, “Press release: The 1989 Nobel Prize in Physics - NobelPrize.org,” 1982.
- [31] M. C. Leake, A. J. M. Wollman, R. Nudd, and E. G. Hedlund, “From Animaculum to single molecules: 300 years of the light microscope,”
- [32] J. B. Nannini and M. Ehrenberg, “The Nobel Prize in Chemistry 2014 - Press Release,” 2014.
- [33] G. Binnig, H. Rohrer, C. Gerber, and E. Weibel, “Surface Studies by Scanning Tunneling Microscopy,” *Physical Review Letters*, vol. 49, pp. 57–61, jul 1982.

- [34] F. J. Giessibl, “Advances in atomic force microscopy,” *Reviews of Modern Physics*, vol. 75, pp. 949–983, jul 2003.
- [35] T. Sumner, “Dazzling history,” *Science (New York, N.Y.)*, vol. 343, pp. 1092–3, mar 2014.
- [36] R. Crease, “Critical Point One amazing moment,” *physics world*, vol. 25, no. 2, 2012.
- [37] C. Giacovazzo, *Fundamentals of crystallography*. Oxford University Press, 2011.
- [38] B. E. Warren, *X-ray Diffraction*. Courier Corporation, 1990.
- [39] G. Taylor, “The phase problem,” *Acta crystallographica. Section D, Biological crystallography*, vol. 59, pp. 1881–90, nov 2003.
- [40] R. E. Burge, M. A. Fiddy, A. H. Greenaway, and G. Ross, “The Phase Problem,” *Proceedings of the Royal Society A: Mathematical, Physical and Engineering Sciences*, vol. 350, pp. 191–212, aug 1976.
- [41] T. E. Glover, D. M. Fritz, M. Cammarata, T. K. Allison, S. Coh, J. M. Feldkamp, H. Lemke, D. Zhu, Y. Feng, R. N. Coffee, M. Fuchs, S. Ghimire, J. Chen, S. Shwartz, D. A. Reis, S. E. Harris, and J. B. Hastings, “X-ray and optical wave mixing,” *Nature*, vol. 488, pp. 603–608, aug 2012.
- [42] S. Haessler, J. Caillat, W. Boutu, C. Giovanetti-Teixeira, T. Ruchon, T. Auguste, Z. Diveki, P. Breger, A. Maquet, B. Carré, R. Taeb, and P. Salières, “Attosecond imaging of molecular electronic wavepackets,” *Nature Physics*, vol. 6, pp. 200–206, mar 2010.
- [43] B. K. McFarland, J. P. Farrell, P. H. Bucksbaum, and M. Gühr, “High Harmonic Generation from Multiple Orbitals in N<sub>2</sub>,” *Science*, vol. 322, pp. 1232–1235, nov 2008.
- [44] O. Smirnova, Y. Mairesse, S. Patchkovskii, N. Dudovich, D. Villeneuve, P. Corkum, and M. Y. Ivanov, “High harmonic interferometry of multi-electron dynamics in molecules,” *Nature*, vol. 460, pp. 972–7, aug 2009.
- [45] T. H. MAIMAN, “Stimulated Optical Radiation in Ruby,” *Nature*, vol. 187, pp. 493–494, aug 1960.
- [46] R. W. Boyd and R. W. Boyd, “The Nonlinear Optical Susceptibility,” *Nonlinear Optics*, pp. 1–67, jan 2008.
- [47] P. A. Franken, A. E. Hill, C. W. Peters, and G. Weinreich, “Generation of Optical Harmonics,” *Physical Review Letters*, vol. 7, pp. 118–119, aug 1961.
- [48] P. B. Corkum, “Plasma perspective on strong field multiphoton ionization,” *Physical Review Letters*, vol. 71, pp. 1994–1997, 1993.

- [49] P. B. Corkum, “Plasma perspective on strong field multiphoton ionization,” *Physical Review Letters*, vol. 71, no. 13, pp. 1994–1997, 1993.
- [50] E. Goulielmakis, M. Schultze, M. Hofstetter, V. S. Yakovlev, J. Gagnon, M. Uiberacker, A. L. Aquila, E. M. Gullikson, D. T. Attwood, R. Kienberger, F. Krausz, and U. Kleineberg, “Single-cycle nonlinear optics,” *Science (New York, N.Y.)*, vol. 320, pp. 1614–1617, 2008.
- [51] G. Farkas, C. Toth, S. D. Moustazis, N. A. Papadogiannis, and C. Fotakis, “Observation of multiple-harmonic radiation induced from a gold surface by picosecond neodymium-doped yttrium aluminum garnet laser pulses,” tech. rep.
- [52] S. Ghimire, A. D. DiChiara, E. Sistrunk, P. Agostini, L. F. DiMauro, and D. a. Reis, “Observation of high-order harmonic generation in a bulk crystal,” *Nature Physics*, vol. 7, no. 2, pp. 138–141, 2011.
- [53] A. Schiffrin, T. Paasch-Colberg, N. Karpowicz, V. Apalkov, D. Gerster, S. Mühlbrandt, M. Korbman, J. Reichert, M. Schultze, S. Holzner, J. V. Barth, R. Kienberger, R. Ernstorfer, V. S. Yakovlev, M. I. Stockman, and F. Krausz, “Optical-field-induced current in dielectrics,” *Nature*, vol. 493, pp. 70–4, jan 2013.
- [54] M. Schultze, E. M. Bothschafter, A. Sommer, S. Holzner, W. Schweinberger, M. Fiess, M. Hofstetter, R. Kienberger, V. Apalkov, V. S. Yakovlev, M. I. Stockman, and F. Krausz, “Controlling dielectrics with the electric field of light,” *Nature*, vol. 493, pp. 75–78, dec 2012.
- [55] T. Higuchi, C. Heide, K. Ullmann, H. B. Weber, and P. Hommelhoff, “Light-field-driven currents in graphene,” *Nature*, vol. 550, pp. 224–228, sep 2017.
- [56] T. Higuchi, M. I. Stockman, and P. Hommelhoff, “Strong-Field Perspective on High-Harmonic Radiation from Bulk Solids,” *Physical Review Letters*, vol. 113, p. 213901, nov 2014.
- [57] G. Vampa, T. J. Hammond, M. Taucer, X. Ding, X. Ropagnol, T. Ozaki, S. Delprat, M. Chaker, N. Thiré, B. E. Schmidt, F. Légaré, D. D. Klug, A. Y. Naumov, D. M. Villeneuve, A. Staudte, and P. B. Corkum, “Strong-field optoelectronics in solids,” *Nature Photonics*, vol. 12, pp. 465–468, aug 2018.
- [58] F. Bloch, “Über die Quantenmechanik der Elektronen in Kristallgittern,” *Zeitschrift für Physik*, vol. 52, pp. 555–600, jul 1929.
- [59] D. Golde, M. Kira, T. Meier, and S. W. Koch, “Microscopic theory of the extremely nonlinear terahertz response of semiconductors,” *Physica Status Solidi (B) Basic Research*, vol. 248, no. 4, pp. 863–866, 2011.

- [60] G. Vampa, C. R. McDonald, G. Orlando, P. B. Corkum, and T. Brabec, “Semiclassical analysis of high harmonic generation in bulk crystals,” *Physical Review B*, vol. 91, no. 6, p. 064302, 2015.
- [61] Y. S. You, D. Reis, and S. Ghimire, “Anisotropic high-harmonic generation in bulkcrystals,” *Nature Physics*, vol. 1, no. November, pp. 1–6, 2016.
- [62] I. Floss, C. Lemell, G. Wachter, V. Smejkal, S. A. Sato, X. M. Tong, K. Yabana, and J. Burgdörfer, “Ab initio multiscale simulation of high-order harmonic generation in solids,” *Physical Review A*, vol. 97, no. 1, pp. 1–5, 2018.
- [63] O. D. Mücke, “Isolated high-order harmonics pulse from two-color-driven Bloch oscillations in bulk semiconductors,” *Physical Review B*, vol. 84, p. 081202, aug 2011.
- [64] H. Haug and S. W. S. W. Koch, *Quantum theory of the optical and electronic properties of semiconductors*. World Scientific, 2009.
- [65] F. Schlaepfer, M. Lucchini, S. A. Sato, M. Volkov, L. Kasmi, N. Hartmann, A. Rubio, L. Gallmann, and U. Keller, “Attosecond optical-field-enhanced carrier injection into the GaAs conduction band,” *Nature Physics*, vol. 14, pp. 560–564, jun 2018.
- [66] N. Tancogne-Dejean, O. D. Mücke, F. X. Kärtner, and A. Rubio, “Ellipticity dependence of high-harmonic generation in solids: unraveling the interplay between intraband and interband dynamics,” pp. 1–22, 2017.
- [67] G. Vampa, C. R. McDonald, G. Orlando, P. B. Corkum, and T. Brabec, “Semiclassical analysis of high harmonic generation in bulk crystals,” *Physical Review B*, vol. 91, p. 064302, 2015.
- [68] M. Garg, M. Zhan, T. T. Luu, H. Lakhota, T. Klostermann, a. Guggenmos, and E. Goulielmakis, “Multi-petahertz electronic metrology,” *Nature*, vol. 538, no. 7625, pp. 359–363, 2016.
- [69] T.-Y. Du, X.-H. Huang, and X.-B. Bian, “Insight into High-order Harmonic Generation from Solids: The Contributions of the Bloch Wave-packets Moving on the Group and Phase Velocities,” pp. 1–6, 2017.
- [70] K. Kaneshima, Y. Shinohara, K. Takeuchi, N. Ishii, K. Imasaka, T. Kaji, S. Ashihara, K. L. Ishikawa, and J. Itatani, “Polarization-Resolved Study of High Harmonics from Bulk Semiconductors,” *Physical Review Letters*, vol. 120, 2018.
- [71] M. Garg, M. Zhan, T. T. Luu, H. Lakhota, T. Klostermann, A. Guggenmos, and E. Goulielmakis, “Multi-petahertz electronic metrology,” *Nature*, vol. 538, no. 7625, pp. 359–363, 2016.

- [72] N. Tancogne-Dejean, O. D. Mücke, F. X. Kärtner, and A. Rubio, “Impact of the Electronic Band Structure in High-Harmonic Generation Spectra of Solids,” *Physical Review Letters*, vol. 118, no. 8, pp. 1–6, 2017.
- [73] Z. Guan, X.-X. Zhou, and X.-B. Bian, “High-order-harmonic generation from periodic potentials driven by few-cycle laser pulses,” *Physical Review A*, vol. 93, p. 033852, mar 2016.
- [74] T. T. Luu, M. Garg, S. Y. Kruchinin, a. Moulet, M. T. Hassan, and E. Goulielmakis, “Extreme ultraviolet high-harmonic spectroscopy of solids,” *Nature*, vol. 521, pp. 498–502, 2015.
- [75] M. Wu, S. Ghimire, D. A. Reis, K. J. Schafer, and M. B. Gaarde, “High-harmonic generation from Bloch electrons in solids,” *Physical Review A*, vol. 91, p. 043839, apr 2015.
- [76] G. Ndabashimiye, S. Ghimire, M. Wu, D. A. Browne, K. J. Schafer, M. B. Gaarde, and D. A. Reis, “Solid-state harmonics beyond the atomic limit,” *Nature*, vol. 534, no. 7608, pp. 520–523, 2016.
- [77] G. Sansone, E. Benedetti, F. Calegari, C. Vozzi, L. Avaldi, R. Flammini, L. Poletto, P. Villoresi, C. Altucci, R. Velotta, S. Stagira, S. De Silvestri, and M. Nisoli, “Isolated single-cycle attosecond pulses,” *Science (New York, N.Y.)*, vol. 314, pp. 443–446, 2006.
- [78] H. Mashiko, S. Gilbertson, C. Li, S. D. Khan, M. M. Shakya, E. Moon, and Z. Chang, “Double Optical Gating of High-Order Harmonic Generation with Carrier-Envelope Phase Stabilized Lasers,” *Physical Review Letters*, vol. 100, p. 103906, mar 2008.
- [79] N. Yoshikawa, T. Tamaya, and K. Tanaka, “High-harmonic generation in graphene enhanced by elliptically polarized light excitation,” *Science*, vol. 356, no. 6339, pp. 736–738, 2017.
- [80] Y. S. You, D. Reis, and S. Ghimire, “Anisotropic high-harmonic generation in bulkcrystals,” *Nature Physics*, vol. 13, no. 4, pp. 345–349, 2016.
- [81] J. M. J. Madey, “Stimulated Emission of Bremsstrahlung in a Periodic Magnetic Field,” *Journal of Applied Physics*, vol. 42, pp. 1906–1913, apr 1971.
- [82] A. Eckardt and E. Anisimovas, “High-frequency approximation for periodically driven quantum systems from a Floquet-space perspective,” *New Journal of Physics*, vol. 17, p. 093039, sep 2015.
- [83] J. Haines, J. M. Léger, F. Gorelli, D. D. Klug, J. S. Tse, and Z. Q. Li, “X-ray diffraction and theoretical studies of the high-pressure structures and phase transitions in magnesium fluoride,” *Phys. Rev. B*, vol. 64, no. 13, pp. 1341101–13411010, 2001.

- [84] J. P. Perdew, K. Burke, and M. Ernzerhof, “No Title,” *Phys. Rev. Lett.*, vol. 77, no. 18, pp. 3865–3868, 1996.
- [85] S. Meng and E. Kaxiras, “Real-time, local basis-set implementation of time-dependent density functional theory for excited state dynamics simulations,” *J. Chem. Phys.*, vol. 129, no. 5, p. 54110, 2008.
- [86] S. Hüller and J. Meyer-Ter-Vehn, “High-order harmonic radiation from solid layers irradiated by subpicosecond laser pulses,” *Physical Review A*, vol. 48, no. 5, pp. 3906–3909, 1993.
- [87] P. A. Golovinski and P. A. Preobrazhenski, “Nonlinear scattering of laser pulse by electron in periodic potential,” pp. 133–139, 2005.
- [88] P. Kálmán and T. Brabec, “Evolution of coherent hard-x-ray radiation generated in crystalline solids by high-intensity femtosecond laser pulses,” *Physical Review A*, vol. 53, pp. 627–629, jan 1996.
- [89] P. Kalman and T. Brabec, “coherent hard-x-ray radiation,” vol. 52, no. 1, 1995.
- [90] H. Liu, Y. Li, Y. S. You, S. Ghimire, T. F. Heinz, and D. A. Reis, “High-harmonic generation from an atomically thin semiconductor,” *Nature Physics*, vol. 1, no. November, pp. 2–4, 2016.
- [91] D. Strickland and G. Mourou, “Compression of amplified chirped optical pulses,” *Optics Communications*, vol. 56, pp. 219–221, dec 1985.
- [92] M. T. Hassan, A. Wirth, I. Grguraš, A. Moulet, T. T. Luu, J. Gagnon, and V. Pervak, “Invited Article : Attosecond photonics : Synthesis and control of light transients Invited Article : Attosecond photonics : Synthesis and control of light transients,” vol. 111301, pp. 1–19, 2012.
- [93] M. T. Hassan, A. Wirth, I. Grguraš, A. Moulet, T. T. Luu, J. Gagnon, and V. Pervak, “Invited Article : Attosecond photonics : Synthesis and control of light transients,” vol. 111301, pp. 1–19, 2012.
- [94] R. D. Shannon, “Revised effective ionic radii and systematic studies of interatomic distances in halides and chalcogenides,” *Acta Crystallographica Section A*, vol. 32, pp. 751–767, sep 1976.
- [95] O. Taurian, M. Springborg, and N. Christensen, “Self-consistent electronic structures of MgO and SrO,” *Solid State Communications*, vol. 55, pp. 351–355, jul 1985.
- [96] V. Srikant and D. R. Clarke, “On the optical band gap of zinc oxide,” *Journal of Applied Physics*, vol. 83, p. 5447, apr 1998.

- [97] J. R. Chelikowsky and M. Schlüter, “Electron states in  $\alpha$ -quartz: A self-consistent pseudopotential calculation,” *Physical Review B*, vol. 15, pp. 4020–4029, apr 1977.
- [98] C. D. Clark, P. J. Dean, and P. V. Harris, “Intrinsic Edge Absorption in Diamond,” *Proceedings of the Royal Society A: Mathematical, Physical and Engineering Sciences*, vol. 277, pp. 312–329, feb 1964.
- [99] C. H. Park, B.-H. Cheong, K.-H. Lee, and K. J. Chang, “Structural and electronic properties of cubic, 2H, 4H, and 6H SiC,” *Physical Review B*, vol. 49, pp. 4485–4493, feb 1994.
- [100] B. Cordero, V. Gómez, A. E. Platero-Prats, M. Revés, J. Echeverría, E. Cremades, F. Barragán, and S. Alvarez, “Covalent radii revisited,” *Dalton Transactions*, vol. 0, p. 2832, may 2008.
- [101] K. Ramesh Babu, C. Bheema Lingam, S. Auluck, S. P. Tewari, and G. Vaitheeswaran, “Structural, thermodynamic and optical properties of MgF<sub>2</sub> studied from first-principles theory,” *Journal of Solid State Chemistry*, vol. 184, pp. 343–350, feb 2011.
- [102] J. B. Krieger and G. J. Iafrate, “Time evolution of Bloch electrons in a homogeneous electric field,” *Physical Review B*, vol. 33, pp. 5494–5500, apr 1986.
- [103] Z. Wang, S.-S. Li, and L.-W. Wang, “Efficient Real-Time Time-Dependent Density Functional Theory Method and its Application to a Collision of an Ion with a 2D Material,” *Phys. Rev. Lett.*, vol. 114, no. 6, p. 63004, 2015.
- [104] J. Ren, N. Vukmirović, and L.-W. Wang, “Nonadiabatic molecular dynamics simulation for carrier transport in a pentathiophene butyric acid monolayer,” *Phys. Rev. B*, vol. 87, no. 20, p. 205117, 2013.
- [105] A. Castro, M. A. L. Marques, and A. Rubio, “Propagators for the time-dependent Kohn-Sham equations,” *J. Chem. Phys.*, vol. 121, p. 3425, 2004.



# Acknowledgments

First and foremost my sincere gratitude goes to Prof. Eleftherios Goulielmakis for supervising my PhD thesis. Although it sounds cliché but there is no better way of putting that this thesis would not have been possible without his constant support and guidance. He being an exceptionally brilliant experimentalist has taught me the recipe of how good experimental physics is done. I learned the importance of astute observation, perseverance, patience and culture of troubleshooting problems immediately, through him. The enthusiasm he has towards physics was contagious and motivated me throughout my PhD. I would like to thank him for the endless time and effort he has put in to troubleshoot the challenging obstacle I faced during my thesis work. I am also thankful to him to not only help me develop professionally but also grow personally.

I am thankful to Prof Ferenc Krausz and IMPRS-APS for giving me the opportunity to pursue my doctoral studies in his extraordinarily resourceful division of Laboratory for Attosecond Physics at Max Planck Institute for Quantum Optics(MPQ). I am also thankful to Prof. Martin Schultze for his help and suggestions.

The members of the Attoelectronics Group have contributed immensely to my professional and personal time in Munich and later in Rostock. I would like to thank Manish Garg for being a mentor and passing the expertise of working with the experimental setup. I thank him for all the efforts he took to explain and re-explain the fundamentals of ultra-fast optics. I also thank him for his constant support outside the professional environment both during his stay at MPQ and after that. I find myself very lucky to have found personalities like Minjie and Heeyong during my thesis work. Their support made my doctoral life easier and enjoyable. It would not be an exaggeration to say that I have not met more humble person than Hee-Yong and more selfless person than Minjie. Minjie has helped me a lot in understanding the experimental details and Hee-Yong has helped me with the theoretical derivations presented in this thesis. I extend my very warm and compassionate thanks to them. Go ma wo Hee-yong and Xié xié Minjie !

During my PhD stay, I have come across a lot of intelligent minds who have helped me in my thesis work. I would like to extend my sincere thanks to Adomas Baliuka and Matthew Schmitt for proofreading this thesis and providing their inputs to strengthen the theoretical foundations in it.

I am very thankful to have met Benedikt Mayer during the last year of PhD. His motivation towards science and perspective towards life motivated me a lot. I would like to extend my sincere thanks for all the extended professional and personal discussions we

had and also for helping me in smoothly moving from Munich to Rostock during my PhD period. I am also thankful to Tran Trung Luu for his support both during his time at MPQ and after that.

My sincere gratitude also goes to all the collaborators outside the Attoselectronics group who helped in the work presented in this thesis. The time-dependent density functional theory calculations were performed by collaborators Prof. Sheng Meng and Shiqi Hu from The Institute of Physics, Chinese Academy of Sciences and I would like to thank them for the efforts.

I am ever thankful to Till Klostermann, Arohi Jain and Antoine Moulet to help me during my initial days at MPQ and DAAD summer interns Tanmay Verma and Zhaoyou Nie for giving me the opportunity to supervise their internship projects.

I would not have made it through these years without the support from friends in and around Munich. I thank Aritra for being the sink for all my frustration and enthusiasm, Ankan and Manjusha for all the fun-filled evenings and video making sessions, Sambit who lived next door and never forgot to invite me in any social gathering at his place, Vivek who remained the source of motivation and Bhakti who brought the sense of calm in my life and made sure of my sleep and food during the last stage of my PhD. I would also like to thanks Swarupa, Poonam, Aparna, Kireeti and Saptrishi.

Finally, I would like to thank my family for all their love and encouragement. My parents Shri Giriraj Kishore Lakhota and Mamta Lakhota and my grandfather Shri Purushottam Das Maheshwari who supported me in all my endeavors and encouraged me throughout my PhD period.